High Spectral-Efficiency Signaling Schemes for Underwater Wireless Optical Communication Systems

Taha Essalih

ÉCOLE CENTRALE MARSEILLE

N° attribué par la bibliothèque
XXXX

TITRE:

Schémas de transmission à haute efficacité spectrale pour les systèmes de communication optique sous-marine sans-fil

THÈSE
pour obtenir le grade de DOCTEUR

École Doctorale : Physique et Sciences de la Matière
Mention : Optique, Photonique et Traitement des Images

Effectuée à l'INSTITUT FRESNEL
Présentée et soutenue publiquement par:

Taha ESSALIH
le 12 Mars 2021

Directeur de thèse: M. Mohammad-Ali KHALIGHI
Co-Directeur de thèse: M. Hassan AKHOUAYRI

JURY :

Rapporteurs:	M. Laurent ROS	Université de Grenoble Alpes
	M. Eric SIMON	Université de Lille
Examinateurs:	M. Stanislav ZVÁNOVEC	Czech Technical Univ. Prague
	Mme. Muriel ROCHE	École Centrale Marseille
Directeurs de thèse:	M. Mohammad-Ali KHALIGHI	École Centrale Marseille
	M. Hassan AKHOUAYRI	École Centrale Marseille

ANNEE : 2021

ÉCOLE CENTRALE MARSEILLE

N° assigned by library
XXXX

TITLE:

High Spectral-Efficiency Signaling Schemes for Underwater Wireless Optical Communication Systems

THESIS
to obtain the degree of Doctor of Philosophy

issued by ÉCOLE CENTRALE MARSEILLE

Doctoral school : Physics and Material Sciences
Discipline : Optics, Photonics and Image Processing

Carried out at FRESNEL INSTITUTE
Presented and defended publicly by:

Taha ESSALIH
on March 12 2021

Thesis advisor: Mr. Mohammad-Ali Khalighi
Thesis co-advisor: Mr. Hassan Akhouayri

COMMITTEE :

Reviewers:	Mr. Laurent Ros	Grenoble Alpes university
	Mr. Eric Simon	Lille University
Examiners:	Mr. Stanislav Zvánovec	Czech Technical Univ. Prague
	Mrs. Muriel Roche	École Centrale Marseille
Thesis advisors:	Mr. Mohammad-Ali Khalighi	École Centrale Marseille
	Mr. Hassan Akhouayri	École Centrale Marseille

YEAR : 2021

Remerciements

Tout d'abord, je tiens à remercier mes parents et mes frères qui ont partagé mes joies et mes peines tout au long de mon parcours scolaire, qui ont nourri mon esprit en croyant en moi et en mon potentiel. Mes chers parents, ce travail est le fruit de votre dévouement, de vos efforts ainsi que de votre amour inconditionnel, j'espère qu'il vous a rendu fier de votre petit garçon, je vous aime.

Je remercie vivement mon directeur de thèse Monsieur Mohammad-Ali Khalighi, pour la confiance qu'il m'a accordé en me confiant ce travail de thèse, ses innombrables conseils, sa disponibilité et aussi les compétences techniques et managériales que j'ai pu obtenir grâce à son aide et ses conseils. Je le remercie également pour sa forte implication, son soutien sans oublier ses qualités humaines d'écoute et de compréhension tout au long de cette collaboration. Son encadrement était incontestable à la réussite de ce travail. Je tiens également à remercier mon co-directeur de thèse monsieur Hassan Akhouayri pour son excellent encadrement à savoir ses conseils et sa grande disponibilité. Je remercie également tous les membres du laboratoire Fresnel et de l'équipe GSM surtout Monsieur Mouloud ADEL et Monsieur Salah Bourennane.

Par ailleurs, je tiens à exprimer ma profonde gratitude aux membres de mon jury de thèse pour s'être rendus disponibles pour la soutenance. M. Laurent Ros (Professeur, Université Grenoble-Alpes), M. Eric Simon

(Maître-de-conférences HDR, Université de Lille I), M. Stanislav Zvanovec (Professeur, Czech Technical University, Prague) et Mme Muriel Roche (Maître de conférences, ECM). Je tiens à les assurer de ma vive reconnaissance pour l'intérêt qu'ils ont porté à mon travail, ainsi que pour les remarques et les questions pertinentes dont ils ont donné lors de la soutenance. Un remerciement particulier est adressé à Mme Muriel ROCHE, ma responsable de master ainsi que l'examinatrice de cette thèse, je tiens à la remercier profondément de son temps, tout un tas d'encouragement, d'efforts, de conseils qu'elle n'a pas retenu afin de réussir cette thèse. Je remercie Monsieur Yves Chardard, directeur de Sub-Sea Tech Marseille, et Monsieur Jan Opderbecke IFREMER, d'avoir accepté l'invitation à participer au jury.

Finalement, je voudrais remercier mes collègues Le, Ikenna, Mahmoud, Oussama, Jahid, Paul. Leur réconfort et les moments géniaux que nous avons passés ensemble dans et en dehors du laboratoire étaient un honneur, je les garderai toujours en mémoire.

List of acronyms

ACO-OFDM : Asymmetrically-clipped optical orthogonal frequency-division multiplexing.
ADC : Analog-to-digital converter.
ADO-OFDM : Asymmetrically-clipped DC-biased optical orthogonal frequency-division multiplexing.
AP : Afterpulsing.
APD : Avalanche photodiode.
AQ : Active quenching.
ARQ : Automatic repeat request.
AUV : Autonomous underwater vehicles.
AWG : Arbitrary waveform generator.
BER : Bit error rate.
BL : Beer-Lambert.
BW :. Bandwidth.
CP : Cyclic prefix.
CT : Crosstalk.
DCO-OFDM : DC-biased optical orthogonal frequency-division multiplexing.
DCR : Dark count rate.
DFE : Decision feedback equalizer.
DR : Dynamic range.
EM : Electromagnetic.
eU-OFDM : Enhanced unipolar orthogonal frequency-division multi-

plexing.
FEC : Forward error correction.
FF : Fill factor.
FFT : Fast Fourier transform.
FOV : Field of view.
FSO : free space optical communication.
Gbps : Gigabits per second.
HACO-OFDM : Hybrid asymmetrically-clipped optical orthogonal frequency-division multiplexing.
HPAM-DMT : Hybrid pulse-amplitude-modulation discrete-multitone.
IFFT : Inverse fast Fourier transform.
IM/DD : Intensity modulation with direct detection.
IR : Impulse response.
ISI : Inter-symbol interference.
LACO-OFDM : Layered Asymmetrically-clipped optical orthogonal frequency-division multiplexing.
LBI : Low bit error rate interval.
LD : Laser diode.
LED : light-emitting diode.
Mbps : Megabits per second.
MCM : multi-carrier modulation.
MIMO : Multiple-input-multiple-out.
MPPC : Multi-pixel photon counters.
NLD : Non-linear distortion.
NRZ OOK : Non-return to zero on-Off-keying.
O-OFDM : Optical orthogonal frequency-division multiplexing.
OOK : On-Off-keying .
PAM : Pulse amplitude modulation.
PAM-DMT : Pulse-amplitude-modulation discrete-multitone.
PAPR : Peak-to-average power ratio.
PD : Photo-detector.

PDE : Photon detection efficiency.
PMT : Photo-multiplier tubes.
PQ : Passive quenching.
PPM : Pulse position modulation.
QE : Quantum efficiency.
RF : Radio-frequency.
ROV : Remotely operated vehicles.
RPAM-DMT : Real pulse-amplitude-modulation discrete-multitone.
Rx : Receiver.
SC-FDE : Single-carrier frequency domain equalization .
SCM : Single-carrier modulation.
SiPM : Silicon photo-multipliers.
SNR : Signal-to-noise ratio.
SQRT : Square root transformation.
SPAD : Single photon avalanche diodes.
SSPM : Solid state photomultiplier.
Tx : Transmitter.
U-OFDM : Unipolar orthogonal frequency-division multiplexing.
UWOC : Underwater wireless optical communications.
UWSN : Underwater sensor network.
VLC : Visible light communication.

Abstract

Emerging maritime applications such as ecological monitoring, natural resource discovery, and port security have an inherent need for high data-rate underwater wireless links. Underwater wireless optical communications (UWOCs) are recognized as a cost-effective and energy-efficient alternative or complementary technology to acoustic and radiofrequency underwater communication systems. To extend the transmission range of UWOC systems, there has been a growing interest in employing silicon photo-multipliers (SiPMs) at the receiver, which ensure high sensitivity in addition to several implementation and operational advantages, as compared with photo-multiplier tubes, for instance. This thesis studies SiPM-based UWOC links and focuses on the appropriate signalling schemes that offer high spectral efficiency in order to overcome the bandwidth limitation of SiPMs and/or emitting devices. We consider, in particular, optical orthogonal frequency-division multiplexing (O-OFDM) schemes and investigate their advantages and limitations by taking into account the limited dynamic range of the transmitter and the receiver, as well as the constraint on the transmit electrical power. We start by studying the performance of the two popular schemes of DC-biased and asymmetrically-clipped O-OFDM (DCO- and ACO-OFDM), and show the advantage of the former in terms of link range flexibility. We further consider a few recently-proposed spectrally-enhanced schemes including the hybrid ACO and the layered ACO (HACO- and LACO-OFDM) and show the good compromise that they make between energy efficiency

and operational range flexibility, at the cost of a higher computational complexity and a longer delay latency at the receiver.

Les applications maritimes émergentes ont un besoin inhérent de liaisons sans-fil à haut débit. Les communications optiques sans-fil sous-marines (UWOC) permettent d'atteindre des débits très élevés et sont reconnues comme une technologie alternative ou complémentaire aux systèmes de communication sous-marine acoustiques et radiofréquences avec les avantages indéniables en termes d'efficacité énergétique et de coût. Pour étendre la portée des liaisons UWOC, il y a eu un intérêt croissant depuis quelques années pour l'utilisation des photomultiplicateurs en silicium (SiPM) au récepteur, qui permettent une sensibilité élevée, en plus d'une mise en œuvre moins complexe comparé aux tubes photomultiplicateurs, par exemple. Cette thèse est consacrée à l'étude des liaisons UWOC utilisant des SiPMs et se concentre sur les schémas de transmission qui offrent une efficacité spectrale élevée afin de surmonter les limitations de bande passante des composants optoélectroniques. En particulier, nous considérons les schémas optiques de multiplexage orthogonal par répartition en fréquence (O-OFDM) et étudions leurs avantages et limites en tenant compte de la dynamique limitée de l'émetteur et du récepteur et de la contrainte sur la puissance à l'émission. Dans un premier temps, nous étudions les performances des deux schémas populaires de DCO-OFDM et ACO-OFDM et démontrons l'avantage du premier en termes de flexibilité de la portée de liaison UWOC. Ensuite, nous nous intéressons à plusieurs schémas d'O-OFDM récemment proposés pour améliorer leurs efficacités spectrales, tels que le HACO-OFDM et le LACO-OFDM. Nous montrons, entre autres, le bon compromis qu'ils font entre l'efficacité énergétique et la flexibilité de la portée, au prix d'une complexité calculatoire plus élevée et d'une latence plus importante au niveau du récepteur.

Résumé étendu

Introduction :

L'eau représente plus de 75 % de la surface de la Terre, les ressources et la vie sous-marines ont toujours suscité l'intérêt de l'humanité pour les explorer vu que notre connaissance de ce milieu reste très limitée. En effet, le corps humain est incapable de supporter le manque d'oxygène et de tolérer des pressions extrêmement élevées, la raison par laquelle les scientifiques ont fabriqué des équipements sous-marins pour découvrir cet environnement. Ces robots sous-marins peuvent naviguer dans des zones difficilement accessibles et peuvent être utilisés avec des réseaux de capteurs sous-marins. La conception de véhicules sous-marins sans câble leur permettra de naviguer librement et d'améliorer leur portée opérationnelle. De ce fait, concevoir une transmission sans fil sous l'eau est un élément clé pour le fonctionnement efficient de ces équipements.

Les ondes acoustiques offrent la meilleure solution pour les communications sous-marines de très longues distances. Cette technologie classique de communication sous-marine est actuellement utilisée pour diverses applications, par exemple, la recherche marine, la surveillance de la pollution, l'océanographie, l'industrie pétrolière, la découverte de nouvelles ressources et la défense [1,2]. En effet, le son se propage sous forme d'onde de pression et peut facilement se propager au cours de très longues distances atteignant des centaines de kilomètres [3]. Cependant,

pour assurer cette communication à longue distance, il est nécessaire d'utiliser des fréquences basses limitant le débit de transmission [1]. Les ondes radio-fréquence, quant à elles, peuvent se propager sur de longues distances dans l'eau de mer conductrice en utilisant de très basses fréquences, mais cela nécessite de grandes antennes et des puissances de transmission élevées et limite le débit à quelques bits par seconde.

Les communications optiques sans fil sous-marines (UWOC) constituent une alternative intéressante aux communications radio-fréquence et acoustiques. Les ondes optique ont la capacité de transmettre des débits élevés avec une grande efficacité énergétique sur des distances courtes à moyennes grâce à la large bande disponible. Les ondes optiques sont le meilleur candidat pour les transmissions multimédias à haute résolution pour les études océanographiques.

Notre objectif dans cette thèse est d'évaluer l'utilisation des récepteurs qui s'appellent photomultiplicateurs au silicium (SiPM) qui sont très sensibles et utilisés essentiellement pour améliorer la distance entre l'émetteur (Tx) et le récepteur (Rx). Les SiPMs sont des réseaux d'APDs ayant la capacité de détecter un seul photon arrivant sur leur surface. Ils ont une sensibilité élevée et un gain interne à l'ordre de 10^6, avec le principal avantage d'une faible tension de polarisation. Cependant, leurs principales contraintes sont la petite surface active et la faible gamme dynamique.

En raison de la limitation de la bande passante que les composants optoélectroniques peuvent présenter (notamment l'SiPM), nous étudierons des schémas optiques de transmission de signaux par multiplexage de fréquence orthogonale pour faire face à la sélectivité des canaux. L'O-OFDM est populaire dans les systèmes de communication en lumière visible (VLC) [75] tout en tant proposé en tant que base pour les normes

en évolution [18,76]. Cependant, il peut en résulter un rapport de la puissance de crête sur la puissance moyenne (PAPR) élevé qui peut causer une dégradation significative des performances du système. Pour cela, nous considérons l'utilisation des diodes électroluminescentes (LED) en Tx, qui ont l'avantage d'une puissance de sortie relativement élevée et la flexibilité d'être arrangées en réseaux.

Nous étudions l'utilisation de schémas de transmission appropriés parmi les techniques O-OFDM proposées dans la littérature. Nous évaluons les performances de ces schémas, en considérant la dynamique limitée du SiPM et du dispositif d'émission, tout en tenant compte la contrainte de puissance électrique à l'émission.

Hypothèses génerales :

Nous considérons une liaison parfaitement alignée et nous supposons une synchronisation temporelle parfaite entre le Tx et le Rx. nous négligeons également la turbulence océanique en supposant que le gradient de température, de salinité, ainsi que les courants marins sont davantage négligeables. Du côté Tx, une LED ou un réseau de LED est utilisé comme dispositif d'émission. Par conséquent, la modulation d'intensité (IM) est utilisée et associé avec une détection directe (DD) au niveau de Rx. Nous supposons également que le Rx possède une connaissance parfaite de la réponse impulsionnelle du canal (IR), d'autres mots les réponses impulsionnelles de Tx, du canal aquatique et du Rx.

Considérons le modèle lambertien de rayonnement de la LED P_t qui est donné par [22] :

$$P_t = P_{\text{Tx}} \frac{m+1}{2\pi} \cos^m(\theta), \quad \theta \in [0, \pi/2], \tag{1}$$

où θ est l'angle d'irradiation de la LED, m est l'ordre lambertien et P_{Tx} est la puissance optique transmise. Ignorons les pertes du système, la puissance reçue par la photodiode (PD) est alors donnée par [22] :

$$P_{\text{Rx}} = P_{\text{Tx}} \exp(-KZ) \frac{A}{Z^2}. \tag{2}$$

Z représente la distance entre le Tx et le Rx, K est le coefficient d'atténuation du faisceau dépendant de la longueur d'onde et de la turbidité de l'eau, et A désigne la surface active effective du PD.

Modélisation de l'SiPM

Un SiPM est un réseau de diodes à avalanche biaisées en mode Geiger, ayant la capacité de détecter un seul photon arrivant sur sa surface. Ces "pixels" sont aussi communément appelés diodes à avalanche et à photon unique (SPAD). Le processus de comptage des photons peut être modélisé par une distribution de Poisson. En considérant que le nombre moyen de photons reçus sur la surface du SiPM est représenté par μ, et le nombre de photons comptés par C_{ph}, la probabilité de comptage des photons $Pr(C_{\text{ph}} = k)$ est donnée par [22, 23, 71] :

$$Pr(C_{\text{ph}} = k) = \exp(-\mu)\frac{\mu^k}{k!}, \tag{3}$$

où $C_{\text{ph}} = \sum_{i=1}^{N_{\text{SPAD}}} c_{\text{ph}}(i)$, avec $c_{\text{ph}}(i)$ le nombre de photons du $i^{\text{ème}}$ SPAD, et N_{SPAD} le nombre de SPADs.
Le nombre moyen de photons μ peut être exprimé en fonction de la

puissance optique reçue comme suit [22, 23] :

$$\mu = \left(\frac{\Upsilon_{\mathrm{PDE}}}{E_p} P_{\mathrm{Rx}} + f_{\mathrm{DCR}} \right) (1 + P_{\mathrm{AP}} + P_{\mathrm{CT}})\, T_s, \tag{4}$$

où Υ_{PDE} est l'efficacité de détection des photons f_{DCR} désigne le *dark count rate*, P_{AP} est la probabilité de post-pulsation, et P_{CT} représente la probabilité de diaphonie. De plus, E_p représente l'énergie des photons et T_s est la période de comptage moyenne.
Un autre paramètre important d'un SiPM est le temps mort τ_d, qui correspond au temps nécessaire pour que chaque SPAD se recharge après avoir détecté un photon. Cela entraîne la saturation du SiPM à des puissances de réception relativement élevées (c'est-à-dire à de courtes portées) , ce qui entraîne une distorsion non linéaire des signaux reçus. Le temps mort dépend du dispositif d'extinction utilisé dans la conception du SiPM. Nous considérons dans cette thèse les dispositifs *Passive quenching* (PQ) pour lesquels le nombre moyen de photons de sortie, noté par μ_{PQ}, est donné par [23, 72] :

$$\mu_{\mathrm{PQ}} = \mu \ \exp\Big(- \frac{\mu\, \tau_d}{T_s\, N_{\mathrm{SPAD}}} \Big). \tag{5}$$

0.1 O-OFDM classiques :

En raison de la transmission avec l'IM/DD, le signal transmis doit être strictement positif et réel. C'est la raison par laquelle la plupart des schémas O-OFDM proposés imposent la symétrie hermitienne dans le domaine fréquentiel afin d'obtenir un signal réel dans le domaine temporel [**?**]. L'un des schémas les plus populaires dans la littérature sont le *DC biased O-OFDM (DCO-OFDM)* et le *Assymetrically clipped O-OFDM*.

DCO-OFDM garantit l'unipolarité du signal transmis en rajoutant un biais en courant continu au signal avant l'écrêtage du signal (supérieur et aussi inférieur), ce qui permet d'obtenir une efficacité spectrale relativement élevée au détriment de l'efficacité énergétique. ACO-OFDM, en

revanche, utilise seulement les sous-porteuses impaires lors du modulation, ce qui donne un signal dans le domaine temporel ayant une propriété antisymétrique. Après avoir appliqué un écrêtage de la partie négative, le bruit d'écrêtage résultant n'affecte pas les sous-porteuses modulées. Néanmoins, cette méthode entraîne une perte d'efficacité spectrale d'un facteur 2 par rapport à DCO-OFDM, mais offre une meilleure efficacité énergétique [78].

Les blocs de bits d'entrée sont convertis en symboles (complexes) en utilisant une modulation d'amplitude en quadrature (QAM) d'ordre M, ce qui nous donne les symboles X_k, $k = 0, 1..., N-1$, qui passent ensuite par un bloc transformée de Fourier inverse (IFFT) générant le signal OFDM x_n du domaine temporel :

$$x_n = \frac{1}{\sqrt{N}} \sum_{k=0}^{N-1} X_k \exp\left(j\frac{2\pi}{N}nk\right), \quad n = 0, ..., N-1. \tag{6}$$

Comme expliqué précédemment, pour s'assurer que x_n est réel, une symétrie hermitienne est imposée aux symboles X_k avant la IFFT de telle sorte que [77] :

$$\begin{cases} X_0 &= X_{N/2} = 0, \\ X_k &= X^*_{N-k}, \qquad 0 < k < N/2, \end{cases}$$

où .* dénote le conjugué complexe. Après la IFFT, un prefixe cyclique (CP) est ajouté à chaque bloc pour éviter l'interférence entre symboles causé par le retard de propagation τ_0 du canal. La longueur de CP N_{CP}, est fixée de manière à être plus grande que τ_0/T_s, où T_s est la durée

du symbole OFDM, cela permet de restaurer le signal à la réception en utilisant un égaliseur simple. Ensuite, un facteur d'échelle α est appliqué au signal afin de l'adapter de manière adéquate à la gamme dynamique de LED. Le signal résultant est noté $\breve{x}_n = \alpha x_n$. Ensuite, pour obtenir un signal positif, une polarisation en courant continu est ajoutée à $\breve{x}_n$ avant l'écrêtage au niveau supérieur et inférieur dû à la gamme de fonctionnement limité de la LED. Le signal finalement est écrêté des deux côtés (supérieur et inférieur) en donnant le signal $\tilde{x}_n$.

Nous considérons que la LED est pilotée en mode tension, c'est-à-dire que x_n, $\breve{x}_n$ et $\tilde{x}_n$ sont tous exprimés en volts. Cela n'est pas contraignant, puisqu'il existe une relation de bijection entre le courant d'entrée et la tension de la LED.

Après avoir été transmise par le canal aquatique, l'intensité optique reçue par le Rx est convertie en un signal électrique. Ensuite, après avoir supprimé le CP, les symboles OFDM r_n du domaine temporel récupérés sont passés par un bloc de transformée de Fourier (FFT) dont la sortie est donnée par :

$$R_k = \frac{1}{\sqrt{N}} \sum_{n=0}^{N-1} r_n \exp\Big(- j\frac{2\pi}{N} nk\Big), \quad k = 0, ..., N-1. \tag{7}$$

Les signaux obtenus $\hat{R}_k$ et égalisés sont ensuite transmis au bloc de démappage QAM afin récupérer les bits transmis.

La démodulation du signal QAM est particulièrement importante dans la mesure où le Rx est limité par le bruit quantique en raison de l'utilisation d'un SiPM. Il a été démontré dans [74] qu'en cas de l'O-OFDM,

même si le signal dans le domaine temporel r_n est affecté par un bruit dépendant du signal, le signal dans le domaine fréquentiel (c'est-à-dire R_k à la sortie du bloc FFT) est indépendant du bruit. Par conséquent, la démodulation QAM classique peut être utilisée dans notre cas.

En ACO-OFDM, les données sont envoyées uniquement sur les sous-porteuses impaires. Après l'application de la symétrie hermitienne, la trame de symboles transmise résultante (avant la IFFT) a la forme suivante :

$$\left[0,\, X_0,\, 0,\, X_1,\, 0, ..., X_{N/4-1},\, 0,\, X^*_{N/4-1},\, 0, ..., X^*_1\,\right].$$

De cette manière, après l'IFFT, la partie négative de x_n peut être écrêtée sans aucune perte d'information [86]. Les autres étapes sont similaires à celles décrites pour le DCO-OFDM. Dans la pratique, un biais en courant continu doit être ajouté à $\breve{x}_n$ afin de tenir compte des caractéristiques courant-tension de la LED.

ACO en couche O-OFDM (LACO-OFDM)

Le LACO-OFDM récemment proposé consiste en une superposition de plusieurs signaux ACO, dépendants des propriétés de symétrie du signal. Cette technique présente l'avantage d'une meilleure efficacité spectrale par rapport à ACO-OFDM qui peut s'approcher de celle du DCO-OFDM. Elle bénéficie également d'une plus grande flexibilité, dans le sens où le débit et les performances peuvent être ajustés en réglant indépendamment la taille de la constellation du signal et la puissance allouée dans chaque couche. Le signal transmis est obtenu comme la superposi-

tion de L trames de symboles, chacune correspondant à une "couche". Au sein de chaque couche, le principe de transmission est similaire à celui de l'ACO-OFDM, comme expliqué dans [92, 97] :

— Pour la première couche, la technique de transmission ACO-OFDM est utilisée : $N/4$ symboles et leurs conjugués complexes sont envoyés sur les sous-porteuses impaires $2q+1$ avec $q = 0, 1, ..., N/2-1$. Ils sont ensuite transformés dans le domaine temporel après l'IFFT.
— Pour les couches qui suivent, les trames correspondantes sont mappées sur les sous-porteuses paires restantes, c'est-à-dire pour la deuxième couche, $N/8$ symboles et leurs conjugués complexes sont envoyés sur les sous-porteuses $2(2q + 1)$ avec $q = 0, 1, ..., N/4 - 1$; ils sont transformés dans le domaine temporel après l'IFFT, tandis que les amplitudes des sous-porteuses restantes sont mises à zéro.
— En général, pour la $\ell^{\text{ème}}$ couche, $\ell > 1$, $(N/2^{\ell+1})$ symboles et leurs conjugués complexes sont envoyés sur les sous-porteuses $2^{\ell-1}(2q + 1)$ avec $q = 0, 1, ..., N/2^{\ell+1} - 1$. Ensuite, les amplitudes des sous-porteuses restantes sont mises à zéro et transformées dans le domaine temporel après l'IFFT.

Pour récupérer les données transmises, une détection successive est effectuée au niveau de Rx, comme proposé dans [92], où les symboles sont récupérés couche par couche à partir de r_n. Les symboles de la première couche peuvent être détectés directement, comme dans l'ACO-OFDM. Ces symboles sont ensuite utilisés pour supprimer la distorsion associée à la seconde couche. Le processus est répété successivement jusqu'à ce que l'on détecte les symboles de la $\ell^{\text{ème}}$ couche.

Résultats numériques :

Nous avons étudié l'utilisation de schémas de modulation à haute efficacité spectrale présenté ci-dessus, dans le cas d'un système UWOC basé sur SiPM. Nous avons discuté les limitations en termes de saturation de l'SiPM et la gamme dynamique limitée de Tx. En effet, la particularité de notre étude est que nous prenons en compte le biais nécessaire au niveau de Tx afin de transmettre le signal, en fonction des caractéristiques de la LED utilisée. Les résultats présentés permettent d'avoir une comparaison fiable des performances des schémas considérés.

Nous avons montré que, pour une efficacité spectrale modérée (à peu près $\sim$ 1 bps/Hz), le schéma ACO-OFDM offre la meilleure efficacité énergétique, c'est-à-dire qu'il permet d'atteindre une distance maximale entre le Tx et le Rx pour une puissance électrique d'émission constante. D'autre part, pour une efficacité spectrale relativement élevée (c'est-à-dire supérieures à 2 bps/Hz), la technique ACO-OFDM souffrira d'un PAPR élevé en raison de la grande taille de la constellation requise. Dans ce cas, LACO-OFDM devient le meilleur choix, car il offre un bon compromis entre un PAPR réduit (par rapport à ACO) et un biais requis plus faible (par rapport à DCO), au prix d'une complexité de calcul élevée, en particulier lorsqu'on utilise plusieurs couches. En effet, un signal PAPR élevé peut entraîner soit un niveau de bruit d'écrêtage élevé du côté Tx, soit une distance limitée en raison de la saturation du SiPM du côté Rx. Néanmoins, en relâchant la contrainte sur la puissance transmise, nous avons montré que le DCO-OFDM est le schéma le plus flexible, offrant une grande flexibilité, permettant ainsi un fonctionnement plus robuste.

Conclusion et perspective :

La communication optique sans fil sous-marine est une technologie prometteuse, notamment lorsqu'il s'agit de transmettre des débits élevés sur des distances modérées. Cependant, elle est confrontée à une forte atténuation du signal lors de la transmission sur de longues distances. De plus, la mise en place d'une liaison à débit relativement élevé présente des difficultés en raison de la bande passante limitée des composants optoélectroniques utilisés à la Transmission et à la Réception. Pour résoudre ces problèmes, nous nous sommes concentrés dans cette thèse sur l'étude de l'utilisation de PDs très sensibles, i.e., les SiPMs, ainsi que les schémas de transmission O-OFDM, pour améliorer les performances.

Évidemment, la première perspective est de réaliser les expériences et aussi d'étudier d'autres schémas O-OFDM à faible complexité de calcul. D'autre part, des techniques de multiplexage spatial pourraient être utilisées pour augmenter la portée et les performances, telles que les architectures à entrées multiples et sorties multiples (MIMO), en utilisant des réseaux de LEDs et de SiPM au niveau du Tx et du Rx, respectivement. En outre, des LED de différentes longueurs d'onde peuvent être utilisées pour multiplexer le signal sur différentes longueurs d'onde et améliorer encore le débit. Comme le signal n'est pas atténué de la même manière dans le spectre visible, les tailles de constellation correspondantes ou les puissances électriques de transmission peuvent être ajustées pour chaque longueur d'onde afin d'optimiser les performances globales.

Table of contents

1 General Introduction **1**

1.1 Underwater wireless communications, overview 1

1.1.1 Underwater acoustic communications 1

1.1.2 Underwater radio-frequency communications 3

1.1.3 Underwater optical communications 4

1.2 Thesis Objectives 4

1.2.1 Thesis outline 5

1.2.2 Contribution 6

1.2.3 Author's publication 7

2 Underwater Wireless Optical Communications **9**

2.1 Introduction 9

2.2 Signal Modulation 10

2.2.1 Intensity modulation 11

2.2.2 Multi-carrier modulation 13

2.3 Transmitter 14

2.3.1 Laser diodes 14

2.3.2 Light emitting diode (LED) 15

2.4 Receiver 16

2.4.1 PIN PDs 16

2.4.2 APDs 16

2.4.3 PMTs . . . 16
2.4.4 SiPMs . . . 17
2.5 Aquatic channel modeling . . . 17
2.5.1 Absorption and Scattering . . . 17
2.5.2 Channel impulse response . . . 18
2.6 Other Challenging Channel Impairments . . . 19
2.6.1 Turbulence . . . 19
2.6.2 Beam obstruction . . . 19
2.6.3 Solar noise . . . 19
2.6.4 Link misalignments . . . 20
2.7 Chapter summary . . . 20

3 Silicon Photomultiplier 21
3.1 Introduction . . . 21
3.2 SiPM receivers . . . 22
3.2.1 Working principal . . . 23
3.2.2 Performance Parameters . . . 26
3.2.3 Photon counting . . . 29
3.2.4 Non-linear distortion . . . 30
3.3 SiPM-Based receiver using OOK in UWOC . . . 32
3.3.1 Parameters specification . . . 33
3.3.2 Numerical results . . . 34
3.4 Conclusion . . . 36

4 Optical OFDM for UWOC systems 39
4.1 Introduction . . . 39
4.2 DCO-OFDM . . . 42
4.3 Adapting the Signal Amplitude to the LED dynamic rang . . . 43
4.3.1 Method 1 (Classical approach) . . . 44
4.3.2 Method 2 (Optimal approach) . . . 44

4.4 Performance Study of the UWOC Link 45
4.4.1 Comparison with OOK 45
4.4.2 Impact of Bias Selection for DCO-OFDM 46
4.4.3 Performance of DCO-OFDM with Optimal and Non-optimal DC Bias 48
4.4.4 Required Precision for Calculating the Optimal Bias for DCO-OFDM 49
4.5 DCR Impact on the Link Performance 51
4.6 LED Non-linearity Impact 53
4.7 Conclusion 54

5 Spectrally enhanced ACO-OFDM schemes for SiPM-based UWOC links 57

5.1 Introduction 57
5.2 Description of the Considered Signaling Schemes 59
5.2.1 ACO-OFDM 59
5.2.2 LACO-OFDM 59
5.2.3 HACO-OFDM 62
5.2.4 ADO-OFDM 63
5.2.5 Computational Complexity 64
5.2.6 Adapting signal to DR of the LED 65
5.3 Performance Study of the UWOC Link 66
5.3.1 Link performance study of improved spectral efficiency schemes with the respect to DCO-OFDM 66
5.3.2 Clipping Effect on the Link Performance 70
5.3.3 Impact of Data Rate and Transmit Power 76
5.3.4 Relaxing the Transmit Power Constraint 77
5.3.5 Impact of QAM Constellation Size 77
5.3.6 Increasing Link Span Using Multiple LEDs 81
5.4 Conclusion 83

6 Experimental setup for an UWOC link **87**

6.1 Introduction 87

6.2 Experimental setup description 87

6.3 This part is still going on 89

7 Conclusions and perspectives **93**

7.1 Conclusions 93

7.2 Perspectives for future research 94

A Noise-signal independency in the frequency domain **97**

Bibliography **100**

List of Figures

1.1 Examples of human underwater activities demanding long-distance, high transmission speed, and large data rate wireless communications. Reproduced from [1] . . . 2

1.2 Pictures of underwater mobile units (Courtesy IFREMER). . . . 2

1.3 Absorption coefficient of pure seawater for different transmission wavelengths. Reproduced from [2] . . . 3

2.1 The general block diagram of an UWOC link from [3] . . . 10

2.2 NRZ-OOK modulation signal with $P_{\mathrm{Off,OOK}}$ set to zero . . . 11

2.3 Illustration of PPM signaling with $M = 4$ and $P_{\mathrm{Off,PPM}}$ set to zero. T_s denotes symbol duration. . . . 12

2.4 Example of PAM modulation with $M = 4$ P_{avg} set to zero, T_s denotes the time symbol duration. . . . 13

3.1 Stucture of SiPM, inspired from [4] . . . 23

3.2 Equivalent Circuit of SiPM (two representative microcells) reproduced from [4] . . . 25

3.3 A graph of the current flowing in a microcell of SiPM, inspired from [4] . 25

3.4 Primary and secondary avalanche caused by CT, Inspired from [4] 28

3.5 Illustration of dead time effect on the current pulse. . . . 29

3.6 Example of the resultant current pulse of SiPM for $N_{\mathrm{SiPM}} = 4$. . . . 30

3.7 SiPM photon-count as a function of optical received power P_{Rx} . . . 32

3.8 I-V characteristics of the LED [5]. Blue curve: real characteristic; red line: approximate linearized characteristic with $V_{min} = 2.75$ V , $V_{max} = 4.03$ V , $I_{min} = 1$ mA , $I_{max} = 110$ mA 34

3.9 BER as a function of Z using OOK for $P_{Tx,e}$ = 65mW and 125mW; $R_b = 5$ Mbps 35

3.10 BER as a function of Z using OOK; $R_b = 1, 2, 5$ and 10 Mbps; $P_{\mathrm{Tx},e}$ = 125mW. 36

4.1 Block diagram of the DCO-OFDM signaling scheme. 41

4.2 BER comparison of OOK and DCO-OFDM (with 4-QAM) for $P_{\mathrm{Tx,e}} = 125\,\mathrm{mW}$. $N = 1024$. $N_{\mathrm{CP}} = 2$, 2, 3, and 5, for $R_b = 1$, 2, 5, and 10 Mbps, respectively. . . 47

4.3 BER performance of DCO-OFDM using optimized and non-optimized DC bias. One LED at the Tx with $P_{\mathrm{Tx,e}} = 50\,\mathrm{mW}$; $N = 1024$; $N_{\mathrm{CP}} = 9$; $R_b = 20\,\mathrm{Mbps}$. The corresponding clipping factors are $\alpha = 0.12$ for the optimum bias (corresponding to $B_{\mathrm{DC}} = 2.932$), and $\alpha = 0.145$, 0.0922, 0.062, and 0.0432 for $\mathcal{K}_{\mathrm{dB}} = 4$, 7, 10, and 13 dB (corresponding to $B_{\mathrm{DC}} = 2.9279$, 2.9344, 2.9357, and 2.9377 V), respectively. 48

4.4 Comparison of the BER performance for DCO-OFDM: Optimal DC bias (HP); DC bias obtained by setting a clipping factor of 7 dB; DC bias obtained by setting $\mathcal{K} = 7\,\mathrm{dB}$ but limited to 3.9 V. $N = 1024$; $N_{\mathrm{CP}} = 9$; $R_b = 20\,\mathrm{Mbps}$, $\eta \approx 1\,\mathrm{bps/Hz}$. 49

4.5 Partial derivation of $\mathcal{E}$ with respect to B_{DC} for calculating the optimal bias for DCO-OFDM. 4-QAM modulation, $P_{\mathrm{Tx,e}} = 50\,\mathrm{mW}$; $N = 1024$; $N_{\mathrm{CP}} = 9$; $R_b = 20\,\mathrm{Mbps}$. 50

4.6 Comparison of the BER performance for DCO-OFDM obtained using low- and high-precision (LP and HP) optimal bias calculation with those calculated based on clipping factors of 4, 7, 10, and 13 dB. $P_{\mathrm{Tx,e}} = 50\,\mathrm{mW}$; $N = 1024$; $N_{\mathrm{CP}} = 9$; $R_b = 20\,\mathrm{Mbps}$. 51

4.7 BER performance for 4-QAM DCO-OFDM for DCR=25kHz, 7, 70, and 700MHz. $P_{\mathrm{Tx,e}} = 125\,\mathrm{mW}$; $\mathcal{K} = 7\,\mathrm{dB}$; $N = 1024$; $N_{\mathrm{CP}} = 9$; $R_b = 20\,\mathrm{Mbps}$. 52

4.8 BER performance for 4-QAM DCO-OFDM for DCR = 7 and 700MHz. $P_{\mathrm{Tx,e}} = 125\,\mathrm{mW}$; $\mathcal{K} = 7\,\mathrm{dB}$; $N = 1024$; $N_{\mathrm{CP}} = 9$; $R_b = 1, 20$ and 100 Mbps. 53

4.9 BER performance for 4-QAM DCO-OFDM obtained using non-linear LED characteristics. $P_{\mathrm{Tx,e}} = 50\,\mathrm{mW}$; $N = 1024$; $N_{\mathrm{CP}} = 9$; $R_b = 20\,\mathrm{Mbps}$. 54

5.1 Block diagram of LACO-OFDM signaling with L layers. 60

5.2 Successive layer-based LACO-OFDM signal detection at the Rx with L layers. . 61

5.3 Block diagram of the HACO-OFDM signaling scheme 62

5.4 Block diagram of the ADO-OFDM signaling scheme 64

5.5 BER performance of ADO-OFDM using classical DC bias. $P_{\mathrm{Tx,e}} = 50\,\mathrm{mW}$; $N = 1024$; $N_{\mathrm{CP}} = 9$; $R_b = 20\,\mathrm{Mbps}$. The corresponding clipping factors are $\alpha = 0.142$, 0.115, 0.0935, 0.0695, and 0.0515 for $\mathcal{K}_{\mathrm{dB}} = 3$, 5 7, 10, and 13 dB (corresponding to $B_{\mathrm{DC}} = 2.8495$, 2.8693, 2.8832, 2.8962, and 2.9085 V 67

5.6 BER performance as a function of distance for ADO-, HACO-, and LACO-OFDM. $P_{\mathrm{Tx,e}} = 50\,\mathrm{mW}$, $N = 1024$; $N_{\mathrm{CP}} = 9$, 20, and 28, for $R_b = 20$, 50, and 100 Mbps, respectively, $\eta \approx 1\,\mathrm{bps/Hz}$. 68

5.7 BER performance as a function of distance for 2, 3 and 4-layers LACO-OFDM. $P_{\mathrm{Tx,e}} = 50\,\mathrm{mW}$, $N = 1024$; $\eta \approx 2$ bps/Hz; $N_{\mathrm{CP}} = 5$, 11, and 20, for $R_b = 20$, 50, and 100 Mbps, respectively. 70

5.8 BER performance as a function of distance for ADO, HACO and 3-layer LACO-OFDM. $P_{\mathrm{Tx,e}} = 50\,\mathrm{mW}$, $N = 1024$; $\eta \approx 2$ bps/Hz; $N_{\mathrm{CP}} = 5$, 11, and 20, for $R_b = 20$, 50, and 100 Mbps, respectively. 71

5.9 Contrasting clipping effect on DCO-, ACO-, LACO-, ADO-, and HACO-OFDM BER performances for $Z = 20$ and 70 m. $R_b = 20\,\mathrm{Mbps}$, $N = 1024$, $N_{\mathrm{CP}} = 9$. . . 72

5.10 Comparison of BER performance versus the link range Z and the transmit electrical power $P_{\mathrm{Tx,e}}$ of DCO-, ACO-, and LACO-OFDM taking into account the LED DR and signal clipping. $N = 1024$, $N_{\mathrm{CP}} = 9$, 20, and 28, for data rates of (a) 20, (b) 50, and (c) 100 Mbps, $\eta \approx 1\,\mathrm{bps/Hz}$. 74

5.11 Comparison of BER performance versus the link range Z and the transmit electrical power $P_{\mathrm{Tx,e}}$ of LACO-, ADO-, and HACO-OFDM taking into account the LED DR and signal clipping. $N = 1024$, $N_{\mathrm{CP}} = 9$, 20, and 28, for data rates of (a) 20, (b) 50, and (c) 100 Mbps, $\eta \approx 1\,\mathrm{bps/Hz}$. 75

5.12 BER performance as a function of distance for DCO-, ACO-, and LACO-OFDM. $P_{\mathrm{Tx,e}} = 50\,\mathrm{mW}$, $N = 1024$; $N_{\mathrm{CP}} = 9$, 20, and 28, for $R_b = 20$, 50, and 100 Mbps, respectively, $\eta \approx 1 bps/Hz$. 76

5.13 BER as a function of Z for ACO-, LACO-, HACO-, ADO- and DCO-OFDM, with $P_{\mathrm{Tx,e}} = 50$, 80, 140, 185 and 185 mW, respectively. $R_b = 20$, 50, and 100 Mbps; N and N_{CP} as in Fig. 5.12 and 5.6, $\eta \approx 1\,\mathrm{bps/Hz}$. 78

5.14 BER performance as a function of distance for DCO, ACO and LACO-OFDM. Spectral efficiency of ~ 2 bps/Hz using, e.g., 16QAM for DCO. $N = 1024$, $N_{\mathrm{CP}} =$ 5, 11, and 20, for $R_b = 20$, 50, and 100 Mbps, respectively. Electrical transmit power of (a) 20 mW and (b) 50 mW. 80

5.15 Comparison of BER versus the link range Z and the transmit electrical power $P_{\mathrm{Tx,e}}$ of the three transmission schemes. $N = 1024$, $N_{\mathrm{CP}} = 5$, 11, and 20, for data rates of (a) 20, (b) 50, and (c) 100 Mbps, $\eta \approx 2$ bps/Hz. 82

5.16 BER performance as a function of distance using 100 LEDs with $P_{\mathrm{Tx,e}} = 50$ mW for each; $N = 1024$. (a) $\eta \approx 1$ bps/Hz (e.g., 2-layer LACO and DCO-OFDM with 4-QAM) with $N_{\mathrm{CP}} = 9$, 20, and 28, for $R_b = 20$, 50, and 100 Mbps, respectively; (b) $\eta \approx 2$ bps/Hz (e.g., 3-layer LACO and DCO-OFDM with 16-QAM) with $N_{\mathrm{CP}} = 5$, 11, and 20, for $R_b = 20$, 50, and 100 Mbps, respectively. 84

6.1 Block diagram of the experimental setup. 88

6.2 Picture of the water tank used in the experiment 89

6.3 Pictures of laser diode and mirror used in the experiment 90

6.4 Transmission link using mirrors (M1, M2, and M3) to extend the distance between Tx and Rx 91

List of Tables

1.1 Comparison of underwater communication technologies (Reproduced from [2]). 4

3.1 Hamamatsu C13366 3050GA SiPM parameters [6] 31

3.2 Physical Tx and channel parameters used in the simulations. 34

37table.3.3

46table.4.1

5.1 LBI and maximum attainable range for ADO, HACO, an LACO-OFDM transmission schemes according to Fig. 5.6; $P_{\mathrm{Tx,e}} = 50\,\mathrm{mW}$, $\mathrm{BER} = 10^{-3}$, $\eta \approx 1\,\mathrm{bps/Hz}$. 69

5.2 Signal constellation in different layers of the considered LACO, ADO, and HACO-OFDM transmission schemes for $\eta \approx 2\,\mathrm{bps/Hz}$. 69

5.3 LBI and maximum attainable range for DCO, ACO, an LACO-OFDM transmission schemes according to Fig. 5.12; $P_{\mathrm{Tx,e}} = 50\,\mathrm{mW}$, $\mathrm{BER} = 10^{-3}$, $\eta \approx 1\,\mathrm{bps/Hz}$. 77

5.4 LBI and maximum attainable range for DCO, ACO, LACO, ADO, and HACO-OFDM transmission schemes according to Fig. 5.13; $\mathrm{BER} = 10^{-3}$, $\eta \approx 1\,\mathrm{bps/Hz}$. 79

5.5 LBI and maximum attainable range for DCO, ACO, and LACO-OFDM according to Fig. 5.14; $\mathrm{BER} = 10^{-3}$, $\eta \approx 2\,\mathrm{bps/Hz}$. 81

5.6 LBI and maximum attainable range for DCO, ACO, an LACO-OFDM transmission schemes according to Fig. 5.16; $\mathrm{BER} = 10^{-3}$. 83

CHAPTER 1

General Introduction

1.1 Underwater wireless communications, overview

As water represents more than 75% of the Earth's surface, underwater life and resources have always raised the interest of the humankind to explore them since our knowledge of this environment remains very limited, especially at the deep-sea level. The reason is the inability of the human body to withstand the lack of oxygen and tolerate extremely high pressures. For the last decades, scientists have tried by all means to discover this unknown part of the world to understand it better and explore its resources (human underwater activities are illustrated in Fig. 1.1). For this purpose, underwater equipment has been manufactured to discover this environment, particularly the development of underwater robots such as remotely operated vehicles (ROVs) and autonomous underwater vehicles (AUVs) (see Fig.1.2). These underwater robots can navigate hardly accessible areas and can be used along with underwater sensor networks (UWSNs). Designing cable-free underwater vehicles will allow them to navigate freely and improve their operational range. Underwater wireless data transmission is one of the key features for the efficient operation of such systems.

1.1.1 Underwater acoustic communications

Acoustic waves offer the best solution for underwater communications over very long distances. This conventional underwater communication technology is currently used for various applications, for example, marine research, pollution monitoring, oceanography, oil industry, the discovery of new resources, and defense [9,10]. In fact, sound propagates as a pressure wave and can easily spread over very long distances reaching hundreds of kilometers [11]. However, to ensure this long-distance communication, it is necessary to use low frequencies. The low bandwidth of acoustic waves, limits the transmission data

Figure 1.1 — Examples of human underwater activities demanding long-distance, high transmission speed, and large data rate wireless communications. Reproduced from [1]

(a) ROV Victor 6000, IFREMER [7]

(b) AUV Ulyx, IFREMER [8]

Figure 1.2 — Pictures of underwater mobile units (Courtesy IFREMER).

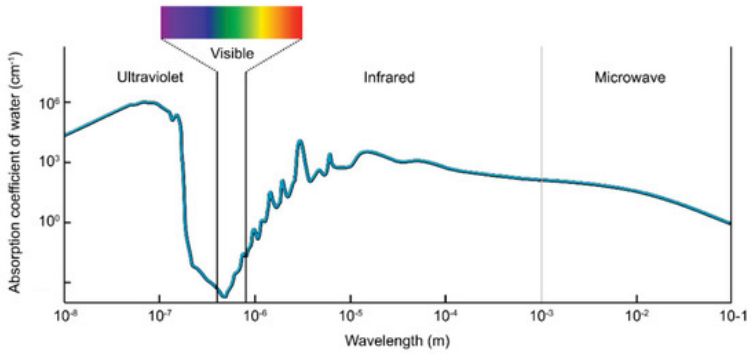

Figure 1.3 — Absorption coefficient of pure seawater for different transmission wavelengths. Reproduced from [2]

rate [9]. Acoustic modems generally operate in bandwidths of the order of a few kHz [11]. For instance, the authors in [12] reported a 69 kbps uplink communication using acoustic waves over a distance of 3.6 km with a frequency band of 10 kHz. Signal attenuation mainly depends on the wave frequency; while frequencies of the order of 10 kHz can be used for communication over distances of around ten kilometers, frequencies on the order of 100 kHz can only be used for shorter distances (of typically several meters) [11]. In addition to the limited data rate of acoustic communications, the transmission antennas are very expensive, bulky, and energy-consuming (an essential criterion for submarine vehicles during underwater missions). Other challenges, include the long delay latency, the doppler effect resulting from the low speed of wave propagation and multi-path propagation [11]. Acoustic waves suffer from low-speed propagation (around 1500m/s), which communication latency.

1.1.2 Underwater radio-frequency communications

An alternative solution for underwater communication is electromagnetic (EM) waves, which have a much higher propagation speed [13]. EM waves in the radio-frequency (RF) range are not affected by temperature and salinity, but their range depends mostly on water constraints such as water conductivity, permittivity, and water permeability [14]. RF waves can propagate over long distances in conductive seawater using very low frequencies (30 Hz-300 Hz), but this requires large antennas and high transmission powers and limits the data rate to a few bits per second [9].

Table 1.1 — Comparison of underwater communication technologies (Reproduced from [2]).

Parameters	**Acoustic**	**RF**	**Optical**
Attenuation	Distance and frequency dependent (0.1-4 dB/km)	Frequency and conductivity dependent (3.5-5 dB/m)	0.39dB/m (Ocean) 11 dB/m (Turbid)
Speed	1500 ms^{-1}	2.3x10^8 ms^{-1}	2.3x10^8 ms^{-1}
Data rate	kbps	Mbps	Gbps
Latency	High	Moderate	Low
Distance	>100 Km	$\leq$ 10m	100-150 m (500 m potential)
Bandwidth	1 kHz -100 kHz	MHz	150 MHz
Frequency band	10 kHz -15 kHz	30 MHz -300 MHz	5x10^{14} Hz
Transmit power	10 W	mW-W	mW-W

1.1.3 Underwater optical communications

As an interesting alternative to RF and acoustic communications, underwater wireless optical communications (UWOCs) have received increasing attention in the past two decades because of their ability to transmit high data rates (up to Gbps) with high energy efficiency over short to moderate distances [15–19] mainly thanks to the large available bandwidth. Hybrid optical/acoustic transmission can also be used for long-distance transmission, as shown in [20]. Due to the high propagation speed of light in water, optical underwater wireless communications have very low latency [21]. Moreover, in low-turbidity waters, the attenuation of blue/green light is very minimal compared to other wavelengths, as seen in Fig. 1.3. Enabling high data rates due to the large bandwidth available, optical waves are the best candidate for high-resolution multimedia transmissions for oceanographic studies, for example.

A brief comparison of the above-mentioned transmission techniques is provided in Table 1.1.

1.2 Thesis Objectives

The primary challenges for UWOC systems include extending the range and enhancing the data rate of these links. To address the former requirement, silicon photo-multipliers (SiPMs), also called multi-pixel photon counters (MPPCs), have recently drawn particu-

lar attention thanks to their high internal gain, allowing a high receiver (Rx) sensitivity, and hence, operation over large distances. In addition, they offer many implementation and operational advantages over photo-multiplier tubes (PMTs) [22]. On the other hand, the data rate of UWOC links is mainly limited by the limited modulation bandwidth (BW) of the emitting device, which is either a laser diode (LD) or a light-emitting diode (LED), and that of the photo-detector (PD). One efficient approach to deal with channel frequency-selectivity is to use optical orthogonal frequency-division multiplexing (O-OFDM). However, the resulting high signal peak-to-average power ratio (PAPR) can cause a significant performance degradation, given the limited dynamic range (DR) of the transmitter (Tx) opto-electronic components (primarily the emitter and its driver).

Our aim in this thesis is to assess the limitation of highly sensitive SiPM receivers when using O-OFDM signaling. For this, we consider the use of LEDs at the Tx, which have the advantage of a relatively high output power and the flexibility of being arranged in arrays. The use of SiPMs at the Rx has the obvious advantage of allowing significant range extension compared to PIN or APD counterparts on the one hand, and operational robustness and implementation simplicity compared to PMTs, on the other hand [22]. Given the limited DR of an SiPM, which primarily impacts Rx performance at relatively short ranges [22, 23], the use of O-OFDM signaling could impose further limitations in practice. To the best of our knowledge, the performance of an SiPM-based Rx with O-OFDM signaling, taking into account the limited DRs of the Tx and the Rx, has not been investigated in detail so far.

More precisely, we investigate the use of appropriate signaling schemes among O-OFDM techniques provided in the literature, namely DC-biased O-OFDM (DCO-OFDM), asymmetrically-clipped (ACO-OFDM), layered ACO (LACO-OFDM), asymmetrically-clipped DCO (ADO-OFDM), and hybrid ACO (HACO-OFDM). We evaluate the link performance of these schemes, considering the limited DR of the SiPM and the emitting device, while taking into consideration the transmit electrical power constraint.

The outline of this thesis is presented below.

1.2.1 Thesis outline

In **Chapter** 2, we will provide a literature review of the current UWOC research. We outline the proposed modulation techniques, the models and components deployed, and the reported results. We will also highlight some practical limitations of the use of this

technology.

In **Chapter** 3, We will present in detail the working principle, model, and limitation of SiPM receivers. Afterwards, we will describe a simple UWOC link using a SiPM as a Rx, the related emitter I-V characteristics. We will show the effect of increasing transit power and data rate on the link performance considering the simple on-Off-keying (OOK) modulation.

In **Chapter** 4, we will study the link performance for the case of using the DCO-OFDM technique. We will mainly focus our study on adapting the DCO signal to the LED DR and setting the optimal DC bias, which is the main factor that determines the transmit electrical power. Then, we will study the effect the LED non-linear I-V characteristics on the link performance.

In **Chapter** 5, we will investigate ACO-OFDM-based transmission techniques to improve the link spectral efficiency while maintaining the energy efficiency advantage of such schemes. First, we will present ACO, LACO, ADO, and HACO techniques and compare their performance for different spectral efficiencies. We will show that the two-layer and three-layer LACO offer the best link performance over HACO and ADO when the spectral efficiency is about 1 bps/Hz and 2 bps/Hz, respectively, for a fixed electrical transmission power. Next, we will contrast the link performances of these OFDM-based schemes considering transmit electrical power, clipping noise, date rate, spectral efficiency. We will show the undeniable advantage of ACO in terms of energy efficiency and the advantage of DCO in offering the best system flexibility. Furthermore, we show that LACO makes a good compromise between power efficiency and operational range flexibility, although it requires a higher computational complexity and, consequently, imposes a longer latency at the Rx.

In **Chapter** 6, we will present the preliminary experimental testbed that we have set up and provide details on the equipment used.

1.2.2 Contribution

The main contributions of this work are summarized in the following.

- Compare simple modulation techniques such as OOK with DCO-OFDM in the UWOC context and showing the real interest of using high spectral efficiency techniques.
- Investigating the use of optimal bias setting method to maximize DCO-OFDM-

based link performance.

- Comparison of ACO, DCO, and LACO-OFDM schemes for a fixed data rate and electrical transmit power, and demonstrating the advantage of DCO in terms of link range flexibility, the interest of LACO in making the best compromise between energy efficiency and operational range at the expense of high computational complexity, as well as the advantage of ACO in terms of energy efficiency.
- Contrasting the performances of LACO, ADO, and HACO-OFDM schemes considering a fixed spectral efficiency and transmit electrical power, and showing the advantage of LACO in offering the best link performance.

1.2.3 Author's publication

T. Essalih, M. A. Khalighi, S. Hranilovic, H. Akhouayri. *Optical OFDM for SiPM-Based Underwater Optical Wireless Communication Links.* Invited paper, MDPI Sensors, no. 21: 6057, 2020.

CHAPTER 2

Underwater Wireless Optical Communications

2.1 Introduction

An underwater wireless optical communication (UWOC) link consists of a transmitter, channel, and receiver, Fig. 2.1.

The purpose of the transmitter block is to modulate signals and feed them to the optical source. In the context of optical transmission when using LED, at the Tx, we use intensity modulation with direct detection (IM/DD). In other words, the transmitted bits are modulated in intensity that is, the corresponding signal after modulation must be positive and real before being transmitted.

The channel can introduce strong attenuation of the light beam before it reach the receiver. Therefore, it is necessary to have an accurate estimation of this attenuation. The channel must be carefully modeled, based on the different characteristics of the water. Several parameters can indicate the amount of light received by the receiver, namely, the distance between the transmitter and the receiver, the concentration of specific substances in the water, and the light rays' divergence.

Finally, we proceed to the receiver, which is designed to collect the received light beams in order to recover the transmitted data. For this, the receiver must have a high sensitivity to detect low-intensity signals due to the aquatic channel's high attenuation.

In this chapter, we will give more detail about the transmitter, channel, and receiver of an UWOC system. In Section 2.2, we will focus on the classical modulation schemes. In Section 2.3, we describe the typically-used optoelectronic components in an

UWOC system. In particular, Section 2.4 will present several types of receivers suitable for UWOC. Then, details on the channel models will be discussed in Section 2.5. Afterwards, in Section 2.6, we will discuss some practical problems that challenge the system's performance. Finally, Section 2.7 summarizes the chapter.

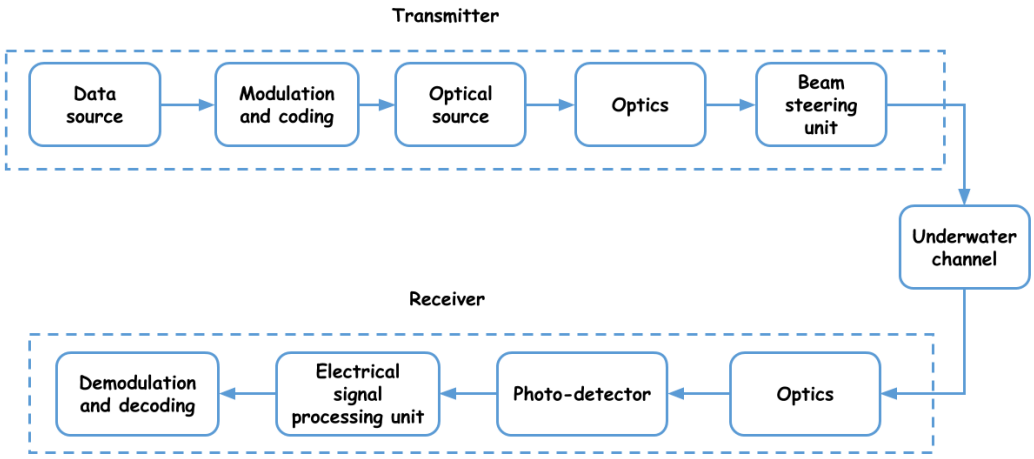

Figure 2.1 — The general block diagram of an UWOC link from [3]

2.2 Signal Modulation

Conventionally, the signal is modulated to adapt to the characteristics of the channel; signals can be modulated in amplitude, phase, or frequency. Choosing the appropriate modulation scheme can significantly improve data rates and the reliability of the UWOC links. IM/DD is mostly employed in UWOC systems where the modulation is mainly based on emitter intensity variations [24, 25], when a non-coherent source like an LED is used at the Tx, intensity modulation becomes the only option.

We can distinguish two signal modulation types: single-carrier modulation (SCM) and multi-carrier modulation (MCM). The first (depending on data rate) uses all the available bandwidth (BW) to transmit signals, while the second split the available bandwidth into several sub-bands and multiplex the signals on there subbands.

This section provides more details on these two modulation types.

2.2.1 Intensity modulation

As explained above, these modulation techniques use optical signal intensity variations to modulate the transmitted data. Principally, the average power P_{avg} and symbol period T_s are set to transmit data at a specific data rate R_b (in bps). The most commonly used intensity modulation techniques are presented in the following [24]:

Non-return to zero OOK

OOK is the classical modulation technique used in optical communication (fiber or free-space optical communication FSO), which has the main advantage of implementation simplicity. We consider the non-return to zero (NRZ) OOK, which is characterized by rectangular pulses; each pulse lasts for a period of T_s. It simply consists of assigning two optical power intensity levels $P_{\text{On,OOK}}$ and $P_{\text{Off,OOK}}$ ($P_{\text{On,OOK}} > P_{\text{Off,OOK}}$) for bits '1' and '0', respectively. The bandwidth of the system is equal to the transmitted data rate $\text{BW}_{\text{OOK}} = R_b$, and the average power can be expressed as follows:

$$P_{\text{avg,OOK}} = \frac{P_{\text{On,OOK}} + P_{\text{Off,OOK}}}{2}. \tag{2.1}$$

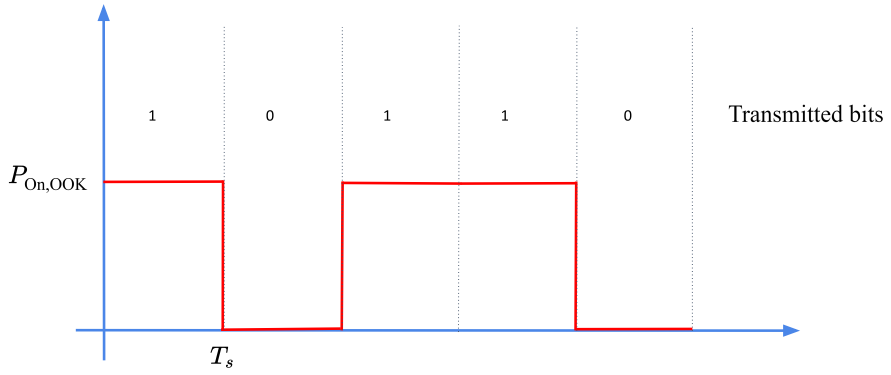

Figure 2.2 — NRZ-OOK modulation signal with $P_{\text{Off,OOK}}$ set to zero

PPM

Pulse position modulation (PPM) is the most efficient amplitude modulation in terms of energy efficiency. Besides, in comparison to OOK, PPM does not require dynamic thresholding for optimal detection when hard detection is performed at Rx [24–28].

Let us assume a classical M-ary PPM with a symbol that corresponds to k bits where $k = \log_2(M)$. Each symbol is assigned to a frame of M intervals, or "slots". Meaning that $M-1$ slots are set to "Off" state while one slot is set to "On" state; the corresponding optical power for "On" and "off" states is $P_{\text{On,PPM}}$ and $P_{\text{Off,PPM}}$, respectively. The position of the "On" slot depends on the k bits to be transmitted (see Fig.2.3). In this case the average transmit optical power is :

$$P_{\text{avg}} = \frac{1}{M}((M-1)P_{\text{Off,PPM}} + P_{\text{On,PPM}}) \tag{2.2}$$

The bandwidth of PPM as a function of data rate R_b can be expressed as $\text{BW}_{\text{PPM}} = MR_b/k$, so compared to OOK, PPM has a lower bandwidth efficiency to achieve the same data rate [25, 29] .

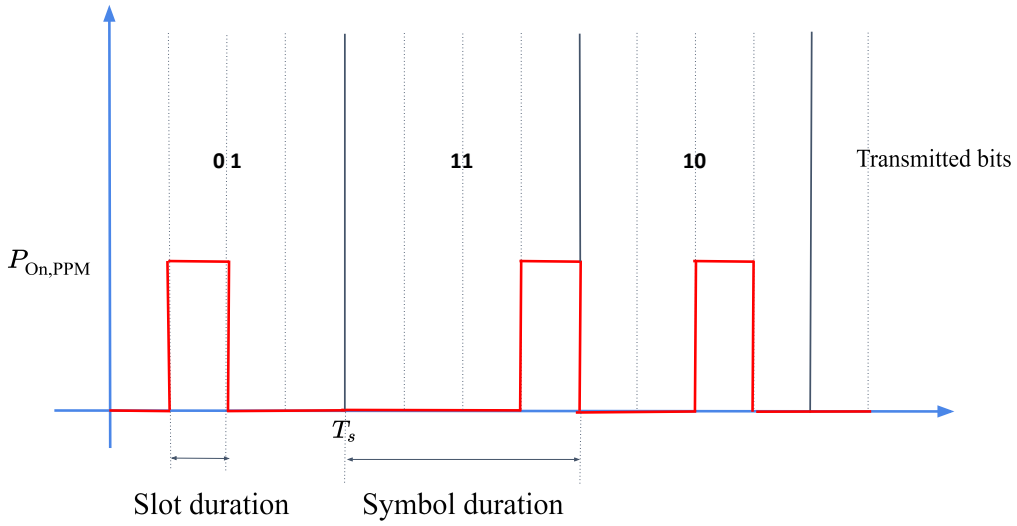

Figure 2.3 — Illustration of PPM signaling with $M = 4$ and $P_{\text{Off,PPM}}$ set to zero. T_s denotes symbol duration.

PAM

Pulse amplitude modulation (PAM) is a multi-level scheme, where symbols are modulated using M different intensity levels, as shown in Fig. 2.4. OOK, for instance, can be considered as a PAM scheme with $M = 2$. For $(M > 2)$, PAM intensity levels can be written as [30] :

$$P_m = \frac{2mP_{\text{avg}}}{M-1} + P_{\text{Off,PAM}}; \quad m = 0, 1, ...M-1 \tag{2.3}$$

where P_{avg} is the average optical power and $P_{\text{Off,PAM}}$ is the lowest intensity used. For the same symbol period as OOK, PAM can transmit $k = \log_2(M)$ bits per symbol, so for a fixed data rate, the signal bandwidth using PAM is $\text{BW}_{\text{PAM}} = \text{BW}_{\text{OOK}}/k$ [29]. As a result, PAM with $(M > 2)$ has a higher bandwidth efficiency compared to OOK.

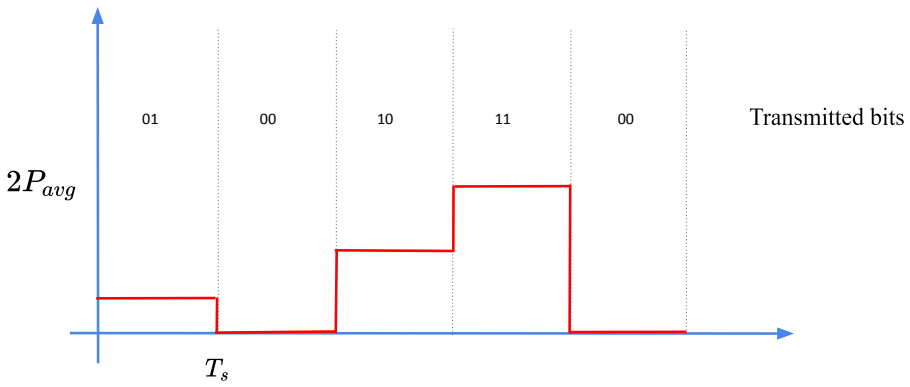

Figure 2.4 — Example of PAM modulation with $M = 4$ P_{avg} set to zero, T_s denotes the time symbol duration.

2.2.2 Multi-carrier modulation

The modulation schemes presented above can be considered as SCM since they use almost the entire available bandwidth for signal transmission. Given the limited system bandwidth, for too much increased data rate, they lead to inter-symbol interference (ISI) necessitating channel equalization at the receiver [31, 32].

As an alternative approach, MCM can be used, such as orthogonal frequency division multiplexing (OFDM) [33, 34] widely used in RF communications. MCM schemes consists of partitioning the bandwidth into a number of sub-channels and multiplexing signals in parallel on them. This allows dealing with flat sub-channel when a single-tap equalizer can be used at the Rx for signal detection. Frequency multiplexing at the Tx and demultiplexing at the Rx can be done using inverse fast Fourier transform (IFFT) and fast Fourier transform (FFT) operation, respectively.

However, OFDM signaling usually results in a high peak-to-average power ratio (PAPR) that can result in a degradation of the system performance. More details about optical OFDM signaling will be later presented in Chapter 4.

2.3 Transmitter

At the Tx, similar transmission techniques as in optical fiber or FSO systems can be used, the particularity concerns the requirement of high energy efficiency and wavelength range that should lie in the blue-green part of the visible spectrum, which corresponding to a low attenuation in relatively turbidity waters. LEDs and LDs are typical choices for optical sources. Solid-state laser technology offers better power efficiency and very focused beams, but it is of higher cost. In this thesis, we consider using classical LED sources for optical transmission.

2.3.1 Laser diodes

LDs are made based on a PN junction formed by two layers of doped Gallium Arsenide, which is forward-biased by an external voltage source [35]. In most UWOC experimental works, LD has been used at the transmitter.

In [36], an experimental transmission link was reported with a data rate of 4.8 Gbps using an LD on 450 nm over a distance of 5.4 m using a water tank with mirrors to reflect light in order to obtain a larger distance. In [37], Nakamura *el al.* established experimentally in a water tank an UWOC link with a data rate of 1.45 Gbps over 4.8 m using a LD with $\lambda = 405$ nm. Using a $\lambda = 450$nm a data rate of 12Gbps was reported in [38] over a distance of 1.7m. In [39], using a LD with $\lambda = 520$nm, a data rate of 5.5Gbps was achieved for a combined air-water transmission link of 26 m (5 m air channel). Recently, a data rate of 500Mbps was reported in [39] over a range of 100 m using a 10 m water tank and mirrors.

While all the above mentioned works were carried out in clear waters, in [40] a comparison was made between blue, green, and red wavelength for the case of turbid waters (based on Monte-Carlo simulations) where the advantage of red wavelength was demonstrated.

Although LDs have a high modulation bandwidth, they are of relatively high cost, compared to LEDs, and their spectral characteristics are sensitive to temperature change [29]. Note that, although LDs have typically a narrow beamwidth, they can be used with a diffuser in order to increase their beamwidth and decrease the link sensitivity to pointing errors.

2.3.2 Light emitting diode (LED)

LEDs would be a suitable alternative to LDs in UWOC applications due to their lower price, compactness, and also their lower power consumption. An LED is a light source that combines a P-type semiconductor with an N-type semiconductor. The holes and electrons in the PN-junction are combined when applying a forward voltage, which releases energy in the form of light [41].

LEDs offer around 20% electrical-to-optical efficiency, supporting relatively high switching speeds, with a typical modulation BW of 10MHz. LEDs have typically larger beam divergence and can be put in array easily to increase the transmit power. A few works considered the use of LEDs at the Tx for UWOC systems. For instance, a data rate of $\sim$ 161 Mbps was achieved in [42] over a range of 2m using a compact low-cost LED on $\lambda = 450$nm.

In order to model mathematically the beam divergence of LEDs, the classical Lambertian model can be used [22]. This way, the LED radiation pattern P_t can be expressed as :

$$P_t = P_{\text{Tx}} \frac{m+1}{2\pi} \cos^m(\theta), \;\; \theta \in [0, \pi/2], \tag{2.4}$$

where P_{Tx} is the transmitted optical power, $\theta \in [0, \pi/2]$ is the LED angle of irradiance and m is the Lambertian order given by $m = -\ln(2)/\ln(\cos(\theta_{1/2}))$ (with $\theta_{1/2}$ being the Tx semi-angle at half-power).

2.4 Receiver

The channel attenuation is typically very severe in underwater scenarios, thus the need for an appropriate receiver design. In order to ensure reliable signal transmission over relatively larger link range, the PD should have a high sensitivity, gain, photo-detection efficiency, and a low noise level. The photodiode (PD) transforms the optical signal into an electrical signal, which is proportional to the optical power received. Different types of PD can be used, such as PIN PDs, avalanche photodiodes (APDs), PMTs, and SiPMs. This section will give some details about working principles and some other practical aspects of these four types of PDs.

2.4.1 PIN PDs

A PIN PD is fabricated using two highly doped P- and an N-type semiconductor layers, separated by a very lightly N-doped region (theoretically intrinsic). In normal operating conditions, PIN PDs work with a low bias voltage typically between 2-5 Volts. The advantage of PIN PDs includes their fast response time and low cost but they have no internal gain. In UWOC context, some experimental works have investigated the use of PINs at the Rx [42–44], and reported high data rates of around hundreds of Mbps to several Gbps over short distances of several meters. For instance, a data rate of 12.5 Gbps over 1.7m was reported in [44] using a PIN PD at the Rx.

2.4.2 APDs

APDs are usually employed in long-range fiber-optics and long-range FSO systems. An APD has an internal gain (typically around 100) due to a process called repeated electronic ionization or avalanche. However, this also results in an increase of the shot noise level. APDs have basically the same semiconductor structure as PIN PDs, but with some additional advantages such as a higher quantum efficiency (about 60-70%) and potentially a faster response [29]. However, APDs need a higher voltage bias than PINs which is typically between $50 - 100$V [45].

2.4.3 PMTs

PMTs are vacuum tubes equipped with a photo-emissive cathode (photocathode) followed by focusing electrodes, an electron multiplier (dynode), and an electron collector (anode). Photons of the received optical signal are converted into electrons and then

multiplied through several dynodes by secondary emission phenomenon, which are then collected by the anode [46]. PMTs have an extremely high sensitivity, a low noise level, and an ultra-fast response, compared to APDs and PIN PDs. Moreover, it provides an internal gain of up to 10^7, which comes at the expense of a higher cost, a high operating voltage (up to 1kV), and bulkiness. PMTs have been investigated in some UWOC works based on simulation results such as [22, 47], and the commercially available BlueComm modem [48], for instance.

2.4.4 SiPMs

SiPMs, are arrays of APDs biased at Geiger mode, with the capacity of detecting one single photon arriving on their surface. Compared to PMTs, they have the same order sensitivity and internal gain (up to 10^6), but with the principal advantage of a low voltage bias typically around 20-30 V. However, their main limitations are much smaller active area and a small DR.
More details on SiPMs, their operating principle, and modeling will be provided in Chapter 3.

2.5 Aquatic channel modeling

Modeling the communication channel correctly is an essential step in the design of any communication systems. In UWOC links, the most important phenomena that affect the link performance are scattering and absorption of light beams, which can be modeled based on the type of water. This section provides a brief description of these phenomena and the channel mathematical modeling.

2.5.1 Absorption and Scattering

Due to the particles present in seawater, light beams are affected by both absorption and scattering. Absorption occurs when the optical signal loses its intensity as it propagates through the water channel. Absorption can be calculated based on different parameters, such as wavelength and the concentration of seawater substances like Phytoplanktons, color dissolved organic material, non-algal materials, and pure seawater composition [29]
On the other hand, scattering can lead to a partial or total change in the direction of photons when colliding with other particles in the water [3]. The diffuse attenuation coefficient K (in the unit of m^{-1}) caused by these phenomena describes the loss of

optical power per meter and depends mainly on the water turbidity and the wavelength of the signal [29].

This thesis considers the classical Beer-Lambert (BL) model to calculate the channel attenuation in the underwater environment. The BL model considers an exponential decrease of the optical power at a specific distance Z from the optical source caused by both absorption and scattering. More specifically, it takes into account any single photon scattering. In other words, by the BL model, each scattered photon is considered as lost and does not contribute to the received signal intensity. By this model, the channel loss L_{ch} is given by [22] :

$$L_{ch} = \exp(-KZ) \tag{2.5}$$

2.5.2 Channel impulse response

For pure sea, clean ocean, and coastal waters, the delay spread of the aquatic channel is negligible while working under data rates below Gbps [21]. Then, the limitation of the channel capacity depends mostly on the limited bandwidth of the optical source and the PD. The bandwidth of the aggregated channel is determined by these of the optical source, the PD, and the aquatic channel. The impulse response (IR) of the aggregated channel h_{eq} can be expressed as follows [22]:

$$h_{eq}(t) = h_{os}(t) * h_{ch}(t) * h_{pd}(t) \tag{2.6}$$

where $h_{os}(t)$, $h_{ch}(t)$, and $h_{pd}(t)$ denote the IRs of the optical source, the aquatic channel, and the PD, respectively, and "$*$" denotes the convolution operator. Since the channel is considered as frequency non-selective [21], we have $h_{ch}(t) = \delta(t)L_{ch}$, where $\delta(t)$ is the Dirac function, and L_{ch} is the channel loss given by (2.5).

The IR of the optical source and the PD are modeled as a 1^{st}-order low pass filter with 3-dB cut-off frequencies of $f_{c,os}$ and $f_{c,pd}$, respectively. This way, $h_{os}(t)$ and $h_{pd}(t)$ can be written as follows [22]:

$$h_{os}(t) = \exp\left(-2\pi f_{c,os} t\right) \quad \text{for } t \geq 0 \tag{2.7}$$

$$h_{pd}(t) = \exp\left(-2\pi f_{c,pd} t\right) \quad \text{for } t \geq 0 \tag{2.8}$$

The aggregated channel can be frequency-selective especially when working with relatively high data rates, which can cause inter-symbol interference (ISI) at the Rx side.

Equalization allows reducing ISI, which can be performed in time or frequency domains, Time-domain equalization usually requires high computational complexity, that becomes problematic, especially when working at high data rates. A reduced complexity can be achieved using frequency-domain equalization [31,32]. Also, another appropriate solution (that we will focus on in this thesis) is to use optical OFDM which allows decreased equalization complexity.

2.6 Other Challenging Channel Impairments

2.6.1 Turbulence

Similar to FSO turbulence can limit the performance of UWOC links by causing channel fading [49], i.e., fluctuations in the intensity of the received signal. Turbulence is the result of refractive index variations along the transmission path, which can be due to the change in water temperature, and salinity or air bubbles. Several works have modeled turbulence for UWOC links [50–53]. Throughout this thesis, we assume that temperature and salinity gradients are negligible [25]. Consequently, the effects of turbulence on the transmission link is considered to be negligible.

2.6.2 Beam obstruction

One of the problems facing UWOC is the obstruction of the beam by living marine organisms such as fish. It is essential to maintain a continuous optical link between the Tx and Rx, which can be managed using channel reinforcement techniques such as automatic repeat request (ARQ) [3,29] or by employing spatial diversity techniques [54].

In this thesis, we assume that there is a negligible risk of beam obstruction.

2.6.3 Solar noise

Solar radiations can increase the Rx background noise level when at relatively shallow waters. The impact of solar noise was investigated in [31, 55] on different types of PDs, such as PIN, APD, PMT, and SiPM. Considering a worst-case configuration for a vertical UWOC link the effect of different Rx characteristics such as the optical filter used, the field of view (FOV), and the aperture size was studied. They concluded that a PIN PD is less much sensitive to background noise, in contrast to a PMT or an SiPM, these latter cannot be used at relatively low depth at the risk of decreased Rx sensitivity or

even saturation. In this thesis, solar noise is considered to be negligible, i.e., we assume working at relatively large depths.

2.6.4 Link misalignments

Communicating with ROVs and AUVs can be challenging due to beam misalignments. Pointing errors can significantly reduce the performance of such underwater links [56,57]. Also, precise localization and tracking are either dificult to use or can result in decreased energy consumption. The use of arrays of LEDs at the Tx and, or PDs at the Rx could reduce the effect of pointing errors. For instance, it was proposed in [58] to use a quasi-omnidirectional link using compact arrays of seven LEDs and seven PDs in the shape of truncated hexagonal pyramidal structures.

2.7 Chapter summary

In this chapter, we presented a general overview of UWOC systems by providing details on the main parts of the transmission link. We discussed, in particular, signal modulation techniques, as well as different types of transmitters and PDs including SiPMs, on which we focus in this thesis.We also presented briefly UWOC channel modeling and described the main channel important factors in practice. The next chapter will provide details on the operating principle, models, limitations, and deployment of SiPM using OOK in a UWOC link.

CHAPTER 3

Silicon Photomultiplier

3.1 Introduction

UWOC aims to establish a communication link for ROVs and AUVs in the seawater environment. The latter introduces an extreme signal attenuation caused by absorption and scattering (see Section 2.5.1). Therefore, it is necessary to use a sensitive PD, which allows detecting a sufficient number of photons to reconstruct the transmitted signal properly. PMTs, for example, can cover a relatively long link distance. However, this technology presents several difficulties in practice, such as bulkiness and the need for high bias voltage [59], which is not practical for UWOC systems since they are designed to be energy efficient. Recently, SiPM has been researched to replace PMTs as it offers a better solution that combines a high sensitivity, low bias voltage, compactness, and low cost. Apart from optical communications, SiPM is used in various medical imaging applications, biophotonics, and high energy physics.

SiPMs were investigated in several UWOC studies to prove its potential effectiveness. The authors of [22] presented a comparison between the performance of SiPM and PMT based on numerical results obtained using LED as a Tx and OOK as a modulation scheme. They subsequently tested these results with an experimental device at [60], establishing a 60 m link at a rate of 3 Mbps. Moreover, a study was conducted on the limitation of SiPM in [31], using OOK and PPM. They evaluated the use of single-carrier frequency domain equalization (SC-FDE), while in [32] they used PAM instead with SC-FDE as well. Besides the numerical results studies, experimental work has also employed SiPM in their tests. Shen *el. al* established a 46m link with a data rate up to Mbps level using PPM modulation, a $450nm$ laser diode in [61], and a blue LED in [62]. Both experiments achieved a bit error rate (BER) lower than the forward error correction (FEC). Finally, by using OFDM (see Chapter 4), the authors demonstrated a data rate of 312.03 Mbps over a 21m distance in [39], while in [63], the authors

demonstrated a UWOC link over only 10m distance using OOK with decision feedback equalizer (DFE) by obtaining 1 Gbps with SiPM as well. Table 3.1 provides a summary of works mentioned above.

year	Paper	Type of Tx	Modulation	Data Rate	Link range	Results	Water Type
2017	[22]	LED	OOK	-	-	Sim	Clear and turbid
2017	[60]	120 bleu LED	OOK	3Mbps	60m	Exp	Jerlov I
2018	[64]	2 Blue LEDs	PAM	12.288Mbps	2m	Exp	Tap Water
2018	[61]	Blue LD	PPM	1.875Mbps	46m	Exp	Tap water
2019	[62]	Blue LED	PPM	-	46m	Exp	Tap water
2019	[32]	Blue LED	PAM + FDE	-	-	Sim	Clear waters
2019	[31]	Blue LED	PPM+FDE	-	-	Sim	Clear waters
2020	[39]	LD	O-OFDM	312.03Mbps	21m	Exp	Tap water
2020	[65]	LD	OOK+DFE	1Gbps	40m	Exp	Tap water

Table 3.1 : Summary of SiPM's state-of-the-art.

The remainder of this chapter will be presented as follows. In Section 3.2, we present the SiPMs working principle, performance parameters, and the photon-counting procedure. Later, we investigate the use of SiPMs in UWOC links using OOK modulation in Section 3.3. Lastly, Section 3.4 concludes the chapter.

3.2 SiPM receivers

For more efficient use of SiPM receivers, a technical explanation is necessary to understand their operation. In this section, we will detail the working principles of the SiPMs and outline their performance parameters. Then, we will cover the photon counting

procedure. Finally, we will evoke some of the limitations of SiPMs, such as shot noise and non-linear distortion (NLD).

3.2.1 Working principal

The SiPM, (also called solid state photomultiplier (SSPM)), is a PD composed of an array of APDs operating in Geiger mode (by biasing the APD above the breakdown voltage). When the APD absorbs a photon, it generates a current pulse lasting several tens of nanoseconds resulting in a massive electrons flow.

Structure: The SiPM consists of a grid with hundreds or thousands of microcells; each contains an APD and a quenching circuit connected in parallel. The microcells in a SiPM are of similar size, ranging from $10\,\mu m$ to $100\,\mu m$ depending on the quenching circuit in place. The active surface of a SiPM varies from $1\,mm^2$ to $6\,mm^2$ and operates along a spectrum range varying from ultraviolet to infrared.

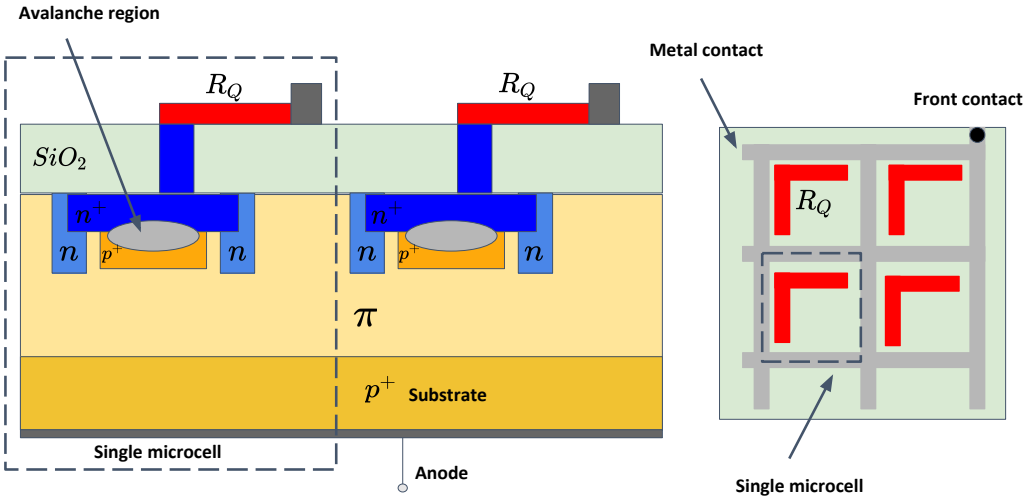

Figure 3.1 — Stucture of SiPM, inspired from [4]

Operation : The gain limitation is avoided when APDs operate in Geiger mode, the latter can be achieved by slightly increasing the voltage (by 10% -20%) above the breakdown voltage [66]. When operating in this mode, APDs provide a high gain and are referred to as single photon avalanche diodes (SPADs) [67]. The difference between

the breakdown voltage and the bias voltage is known as the overvoltage; it controls the device functioning and can be adjusted. When the SPAD absorbs a photon, the generated charge carrier triggers an avalanche in the gain region of a microcell (see Fig. 3.1).

In general, when an avalanche is triggered, the current continues to flow, so it must be stopped or " quenched" by a quenching circuit. This circuit usually contains a resistor (RQ) and in this case, it is called passive quenching (PQ), which is the most commonly used in manufacturing SiPMs.

Fig. 3.2 represents the electrical diagram of two microcells powered by an external voltage bias V_{bias}. The SPAD is modeled by a capacitor C in parallel with a resistor R_s, a switch S, and a voltage source V_{bd}. The SPAD+RQ circuit represents a microcell, and these microcells are connected in parallel. The process of photon detection by an SiPM can be described as follow [4] :

- The S switch is held open as long as the SPAD is not receiving a photon yet. In this case, the voltage around C is equal to the bias voltage V_{Bias}. (see Fig.3.2)

- When a photon is captured, it produces avalanche by closing S; this leads to a discharge of capacitor C through the resistor R_s. The time constant equals to $\tau = R_sC$. Please note that the value of R_s is negligible compared to R_Q.

- The voltage around R_Q increases due to the current flowing through the microcell.

- When the voltage around SPAD reaches the breakdown voltage V_{bd}, the discharge stops, and C begins to recharge again, this lowers the current that flows through the microcell.

- Finally, C is fully recharged, the S switch takes the open position, and the SPAD is ready to detect another incoming photon.

Now let us see how the current behaves during the detection. S is closed, and the current increases, as explained before. t_i is the initial time at which a photon arrives at the SPAD surface, as in Fig. 3.3, the current increases proportionally by $[1 - exp(-\frac{t}{R_sC_s})]$ since it is an RC circuit [4]. The voltage around the SPAD drops to about V_{br}, corresponding to a maximum current value of i_{max} given by [4] :

$$i_{max} = \frac{V_{bias} - V_{bd}}{R_Q + R_S} = \frac{V_{ov}}{R_Q + R_S} \tag{3.1}$$

where V_{ov} is the overvoltage. When the current reaches i_{max} the time correspond to t_{max} (which is about $\sim 1ns$), then, the current decreases according to $exp(-\frac{t}{R_QCj})$. If

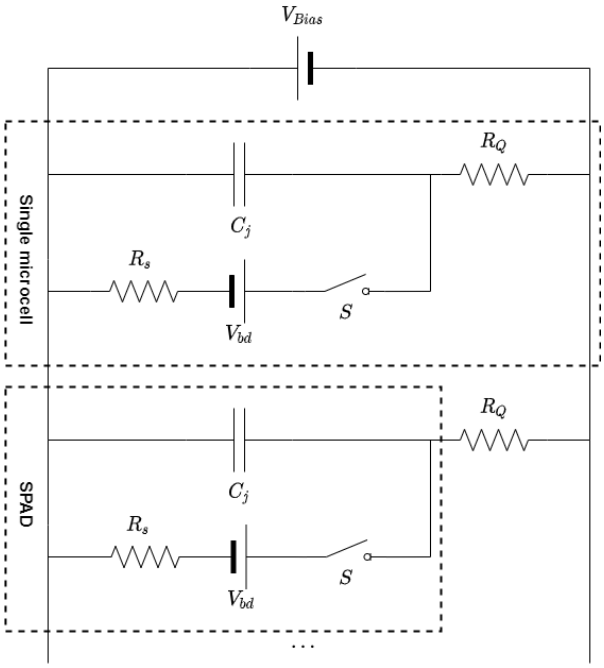

Figure 3.2 — Equivalent Circuit of SiPM (two representative microcells) reproduced from [4]

two microcells fire simultaneously, the resulting current will be the superposition of the two pulses.

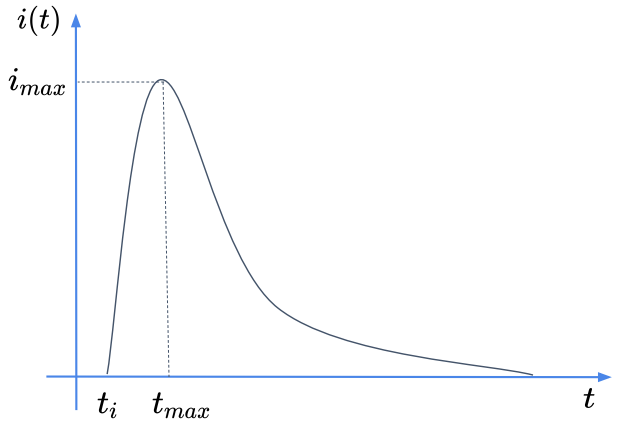

Figure 3.3 — A graph of the current flowing in a microcell of SiPM, inspired from [4]

It is worth mentioning that another electronic circuit can also be used to quench a SPAD, known as active quenching (AQ). This method can be achieved by lowering the bias voltage below the breakdown voltage for a limited time until the breakdown is quenched [29]. AQ provides a higher count rate, tight control of parameters, and no paralyzation of microcells during SPAD saturation (see Section 3.2.4) compared to PQ. However, it is more complex to build and requires more space and energy. In this thesis, we will focus on the PQ method because there are several products available in the market with a variety of characteristics, and also because it offers a good fill factor (see Section 3.2.2) [68].

3.2.2 Performance Parameters

Gain :

When a photon is detected by a cell, electrically, it can be considered as a discharge of the capacitor C_j (see Section 3.2.1). So, the amount of charge in one pulse is about $Q = i_{max}\tau$ and the gain G can be written as [4] :

$$G = \frac{Q}{e} = \frac{i_{max}\tau}{e} = \frac{V_{ov}}{e(R_Q + R_S)}.R_Q C_j \tag{3.2}$$

with e, the charge of the electron. In addition, since $R_Q >> R_S$, G can be defined as :

$$G = \frac{V_{ov}C_j}{e} \tag{3.3}$$

According to equation 3.3, the gain depends mainly on the overvoltage and the junction capacity. Let us note by N_{fired}, the number of microcells or pixels fired simultaneously. As previously mentioned; the current resulting from the SiPM $i_r(t)$ is the superposition of the currents generated by each cell, i.e., $i_r(t) = \sum_{k=1}^{N_{\text{fired}}} i_k(t)$, meaning that the total gain G_t of a SiPM is equal to [67] :

$$G_t = \frac{V_{ov}C_j N_{\text{fired}}}{e} \tag{3.4}$$

Photon detection efficiency (PDE) :

Defined as the probability that the photon hitting SiPM surface will trigger an avalanche which can be defined as [67] :

$$\Gamma_{\mathrm{PDE}}(\%) = \mathrm{FF}.P_G(V).\mathrm{QE}(\lambda) \tag{3.5}$$

where FF is the fill factor, QE is the quantum efficiency, and P_G is the probability of Geiger discharge, also known as the avalanche initiation probability. Note that the surface of the SiPM is not fully sensitive to light, given that space is reserved for the quenching circuit. The FF is defined as the ratio of the sensitive surface (also named active surface) over the total surface of SiPM; it is always given in percentage [67]. QE, on the other hand, is the probability that an incident photon creating an electron-hole pair can trigger an avalanche; generally, this probability depends on the received signal wavelength.

Dark count rate (DCR)

Dark noise is the dominant noise of a SiPM. SPADs can generate electrons due to temperature, causing an avalanche even in the dark (the reason why it is called dark noise). It depends on the active area, the overvoltage, and the temperature. It is considered as noise since the microcell generates a pulse without any photon detection, increasing the intensity of the current generated by the SiPM. The average number of dark noise per second is called dark count rate f_{DCR} expressed in Hz, f_{DCR} value is independent of the received signal. Note that an increase of V_{Bias} or temperature leads to a proportional increase of the DCR [67].

Optical crosstalk (CT) :

When a primary received photon triggers an avalanche in a microcell, it can generate a second photon that can cross the silicon layer to cause a second avalanche in neighboring microcells. CT is another type of SiPM noise because the secondary photon is not part of the received signal [67]. We distinguish two scenarios of the trajectory pursued by the secondary photon [4]:

-Moves directly to the following microcell Fig.3.4 (a).

- Reflected by the substrate region. Fig.3.4 (b).

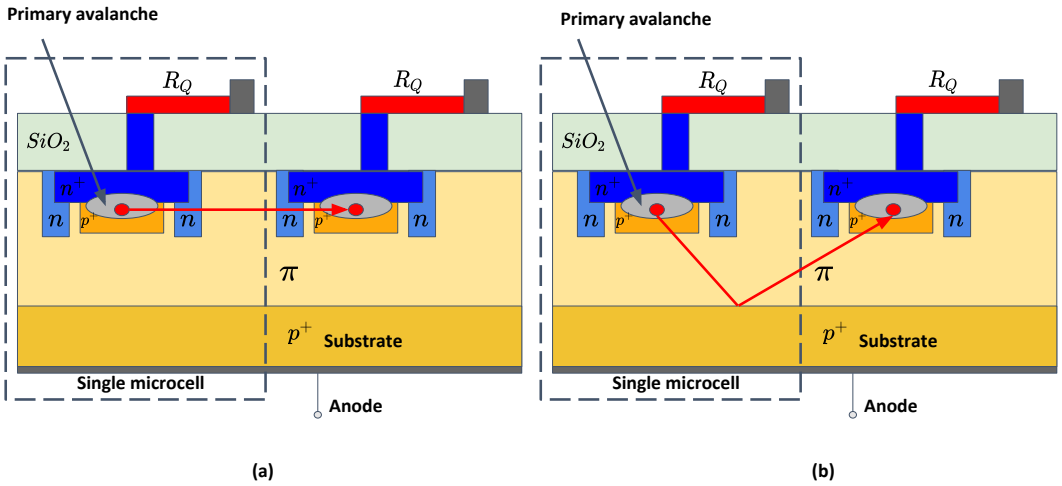

Figure 3.4 — Primary and secondary avalanche caused by CT, Inspired from [4]

CT is modeled by the probability P_{CT} depending on the values of FF and V_{ov} [4]. As the overvoltage increases, the probability P_{CT} also increases.

Afterpulsing (AP) :

AP is another type of noise generated by the SiPMs. It can be characterized as the probability of triggering two successive avalanches in the same microcell caused by a single photon due to charge carriers blocked during the primary avalanche. P_{AP} denotes the probability of AP, and it increases proportionally to the bias voltage, since increasing the bias voltage leads to an increase in the number of charge carriers in an avalanche [69].

Dead time τ_d :

As explained in section 3.2.1, the SPAD needs time to recharge, depending on the time characteristic of the RC circuit. By not respecting the recovery time (also called dead time), the second incoming photon cannot be detected. During this time, C is not fully recharged, yet it will be discharged again without triggering a new avalanche. The recovery time will be extended accordingly, as shown in Fig. 3.5 [70].

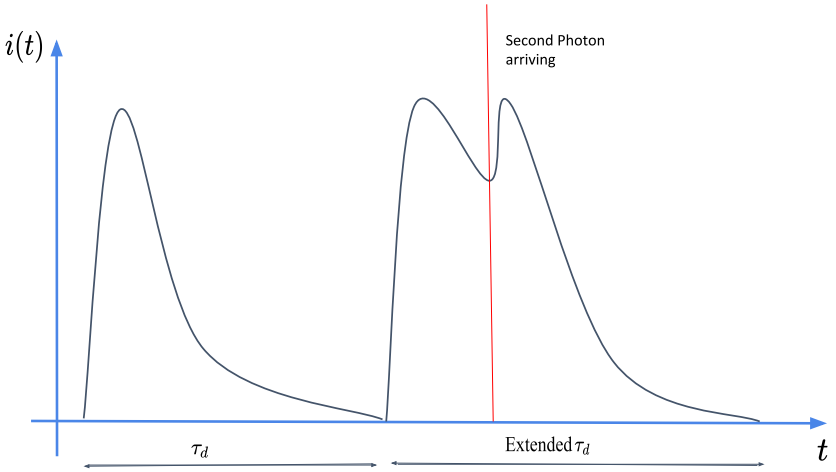

Figure 3.5 — Illustration of dead time effect on the current pulse.

3.2.3 Photon counting

The SPAD is considered a single photon counter since it generates a pulse once a photon is detected (see Fig.3.3). When the SiPM operates in linear mode, i.e., the output of the SiPM is proportional to the intensity of the input optical signal. The number of current pulses is equal to the number of photons detected during a certain period T_s, as shown in Fig. 3.6 (the red curve represents $i_r(t)$).

The total number of photons counted by SiPM C_{ph} over a period T_s is [29] :

$$C_{ph} = \sum_{i=1}^{N_{\text{SiPM}}} c_{ph}(i) \tag{3.6}$$

where N_{SiPM} represents the number of SPADs, and $c_{ph}(i)$ the number of photons of the i^{th} SPAD.

The photon counting process is modeled by a Poisson distribution. We denote by μ the average number of photons received on the surface of the SiPM , the photon count probability $P_r(C_{ph} = k)$ is expressed by [22, 23, 71] :

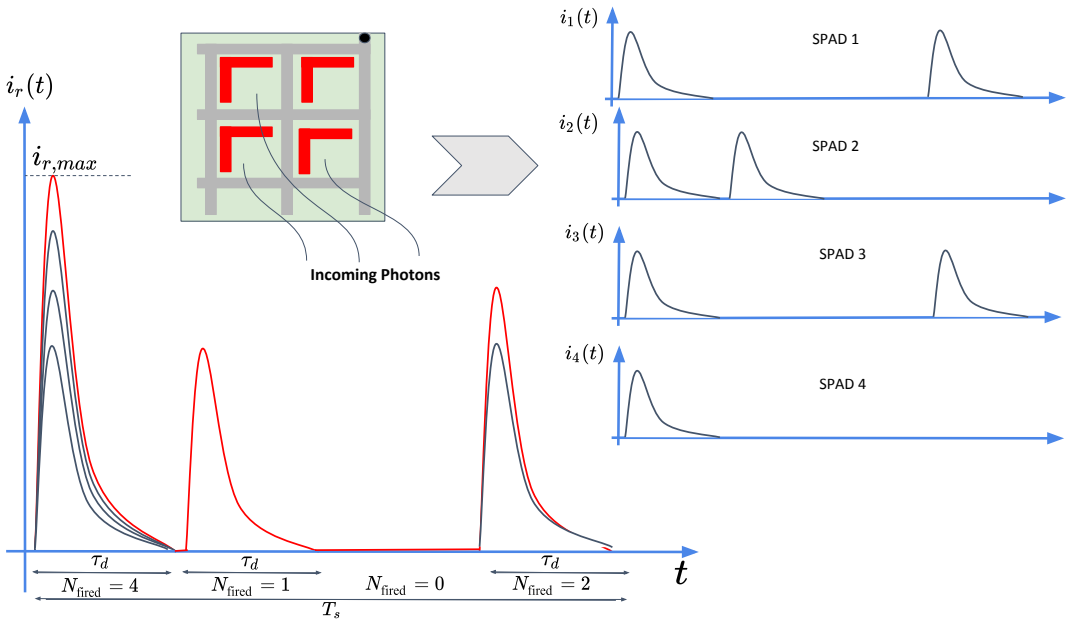

Figure 3.6 — Example of the resultant current pulse of SiPM for $N_{\text{SiPM}} = 4$.

$$P_r(C_{ph} = k) = exp(-\mu)\frac{\mu^k}{k!} \tag{3.7}$$

The average photon count μ can be expressed as a function of the received optical power P_{Rx} as [22, 23]:

$$\mu = \left[\frac{\Gamma_{\text{PDE}}}{E_p}P_{\text{Rx}} + f_{\text{DCR}}\right](1 + P_{\text{AP}} + P_{\text{CT}})T_s \tag{3.8}$$

where T_s the counting period, $E_p = hc/\lambda$ the photon energy, λ the received signal wavelength, h the Planck constant, and c the speed of light.

3.2.4 Non-linear distortion

The increase in the number of photons received from the increase of optical power causes SiPM to operate in a non-linear mode. At a particular high-intensity value of the received signal, SPADs cannot detect all received photons since τ_d is no longer respected. The NLD means that the photon count becomes non-proportional to the received intensity since τ_d will be extended, and the SPADs will be saturated [72]. To summarize, the probability of two photons interacting with the same microcell with a time delay lower

Table 3.1 — Hamamatsu C13366 3050GA SiPM parameters [6]

Photon Detection Efficiency Γ_{PDE}	40%
Surface Area A_{SiPM}	$9\,\mathrm{mm}^2$
Dark Count Rate f_{DCR}	25 kHz
Dead Time τ_d	68.1 ns
Number of SPADs N_{SiPM}	3600
CrossTalk Probability P_{CT}	3%
Afterpulsing Probability P_{AP}	0.1%
3-dB Cut-Off Frequency	4 MHz

than τ_d increases. NLD depends on the quenching methods used. For example, for the AQ device, the recovery time is not extended; the SPAD does not count photons when SPAD is recharging. Therefore the maximum photon detected will be constant after a specific intensity value [72]. The relation between μ the average photon count and μ_{PQ} the real photon count in passive quenching configuration is given by [23, 72] :

$$\mu_{\mathrm{PQ}} = \mu \; exp(-\frac{\mu\tau_d}{T_s N_{\mathrm{SPAD}}}) \tag{3.9}$$

For a better visualization of NLD, we simulate the number of photons received as a function of the received optical intensity P_{Rx} in dBm, over an average counting period $T_s = 1\ \mu s$ and 1 ms. We consider the Hamamatsu C13366 3050GA SiPM [6] with the main characteristics provided in the Table 3.1.

In Fig. 3.7, we can identify the linear zone from the non-linear zone caused by NLD. Obviously, a time interval $T_s = 1$ ms allows having a higher μ_{PQ} than that of $T_s = 1\mu s$ since the SiPM has more time to count photons. Above a particular power value, both curves drop sharply, which corresponds to the NLD. Note that the power value leading to saturation is the same for both time intervals. For the dark region, where no light is received, SiPM counts photons generated by DCR. Based on equation (3.8) we define μ_{dark} as :

$$\mu_{\mathrm{dark}}(P_{\mathrm{Rx}} = 0) = (f_{\mathrm{DCR}} T_s)(1 + P_{\mathrm{AP}} + P_{\mathrm{CT}}) \tag{3.10}$$

P_{AP} and P_{CT} are both included in μ_{dark} equation since an avalanche generated by DCR can also generate after-pulsing and crosstalk. From Table 3.1, we notice that the

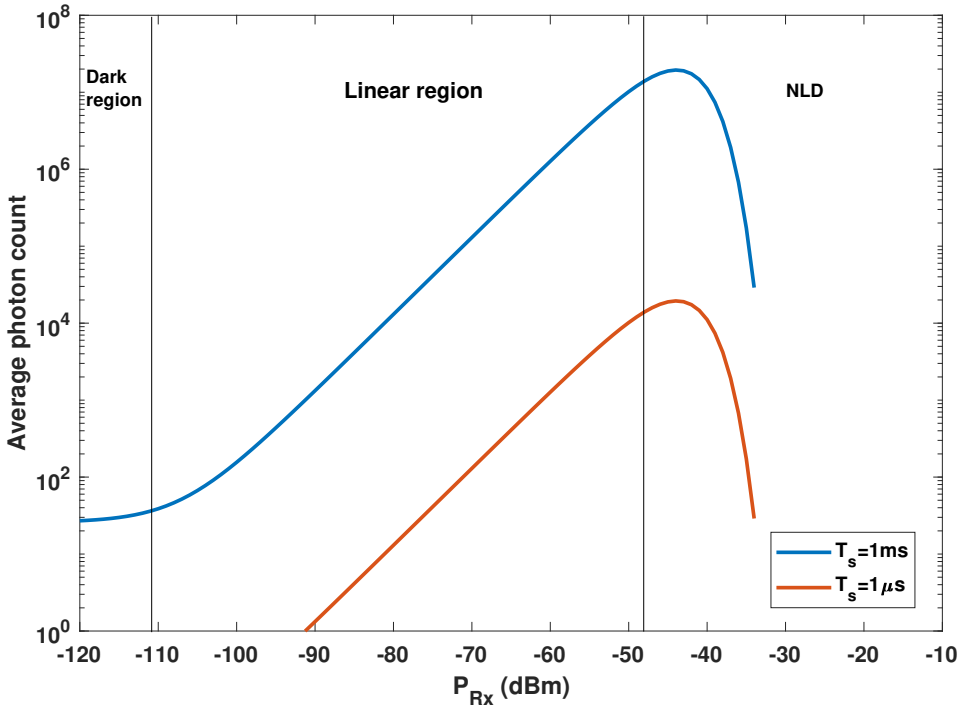

Figure 3.7 — SiPM photon-count as a function of optical received power P_{Rx}

value of f_{DCR} is very low, thanks to the cooling system inside the SiPM module we are using [6], it maintains a temperature of about $-10°C$. According to Fig. 3.7, we realize that for a brief time interval (in this case $T_s = 1\ \mu s$), we have almost no photons generated in the dark region because of this low value of f_{DCR}.

3.3 SiPM-Based receiver using OOK in UWOC

This Section provides a simple OOK link transmission using LED and SiPM as the Tx and the Rx, respectively. LED is modeled as explained in Section 2.3.2, and the channel attenuation is modeled by the Beer-Lambert model described in Section. 2.5. We provide numerical results to show the effect of transmitted power and data rate on link performance.

3.3.1 Parameters specification

In this work, at the Tx, we consider a NICHIA NSPB510AS [5] LED with emitting wavelength $\lambda = 470\,\text{nm}$ and 3-dB cut-off frequency of $10\,\text{MHz}$ [22]. A Lambertian emission pattern is considered for the LED with $m \approx 45$, corresponding to a half-angle of $\approx 10^\circ$ [22]. The I-V characteristics of the LED are shown in Fig. 3.8. For the sake of simplicity, in our analysis, in this chapter we ignore the I-V non-linearity within the LED DR and consider the approximate linearized characteristics Fig. 3.8. Let us denote the lower and upper limits for the LED bias voltage by V_{min} and V_{max}, respectively, and we consider $P_{\text{Tx},e}$ the transmit electrical power.

Without loss of generality, the imperfect conversion efficiency of the LED is neglected. Indeed, an important part of the electrical power consumption at the Tx is due to the conversion efficiency of the LED, typically about 80%, where the corresponding power loss is converted to thermal dissipation.

At the Rx, consider a Hamamatsu C13366 3050GA SiPM [6] Note that this low DCR is obtained by maintaining the chip temperature at -10° Celsius by means of a thermoelectric cooler. The thermal noise effect is reasonably neglected, compared to the SiPM shot noise [73]. The background noise effect is also neglected, assuming that the Rx operates at relatively deep waters [31, 55]. Hence, only the shot and dark noises of the SiPM are taken into account.

Lastly, concerning the aquatic channel, the case of clear waters is considered with the diffuse attenuation coefficient $K = 0.08\,\text{m}^{-1}$ [55]. Table 3.1 and Table 3.2 contain the main parameters of the Tx, channel, and the Rx, used in the simulations.

The limitation caused by the aggregated channel is also taken into account in these simulations, as described in Section 2.5.2. The BW of the aggregate channel is determined by the SiPM BW (~ 4 MHz), which is smaller than the LED BW (~ 10 MHz), and the aquatic channel BW. We assume that the average counting period of the SiPM is equal to the period of the OOK symbols $T_{\text{OOK}} = T_s$, which corresponds to a BW equal to $1/T_s$.

For signal demodulation, the threshold must be optimal to obtain low errors. we indicate by $\mu_{\text{PQ},0}$ and $\mu_{\text{PQ},1}$ the real average number of SiPM photons, which corresponds to the symbols "Off" and "On", respectively. the optimal detection threshold μ_{th} is defined as [32] :

LED central wavelength λ	470nm
LED cut-off frequency	10 MHz
LED Lambertian order m	45
LED I-V parameters (V_{min},V_{max},I_{min},I_{max})	(2.75 V, 4.03 V; 1 mA, 110 mA)
Channel diffuse attenuation coefficient K	0.08m^{-1}

Table 3.2 — Physical Tx and channel parameters used in the simulations.

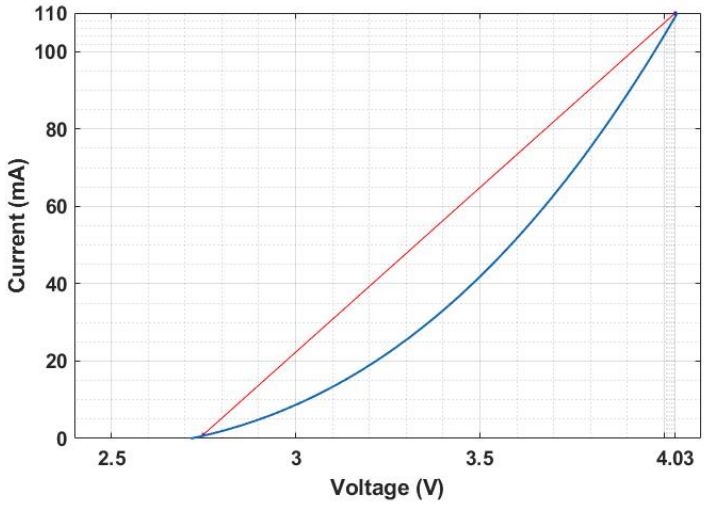

Figure 3.8 — I-V characteristics of the LED [5]. Blue curve: real characteristic; red line: approximate linearized characteristic with $V_{min} = 2.75$ V , $V_{max} = 4.03$ V , $I_{min} = 1$ mA , $I_{max} = 110$ mA

$$\mu_{\text{th}} = \frac{\mu_{\text{PQ},0} - \mu_{\text{PQ},1}}{\log(\mu_{\text{PQ},1}/\mu_{\text{PQ},0})} \tag{3.11}$$

3.3.2 Numerical results

In Fig. 3.9 bit error ratio (BER) plots as a function of link distance (Z) are presented, considering an electrical transmit power of $P_{\text{Tx},e} = 65$mW and 125mW. The transmitted electrical power corresponding to "Off" symbols is set to 2.75 mW (given $V_{min} = 2.75$ V and $I_{min} = 1$ mA). The transmit power for "On" symbols is set to get the average transmit electrical power desired.

Similar to [23], we define the low BER interval (LBI, in units of meter) for a given

transmission scheme, indicating the interval of link range satisfying a low enough BER. The LBI can be considered a measure of link operation flexibility, i.e., in which range interval the system can function with a low enough BER. In other words, the larger the LBI, the more flexible is the designed system with respect to the actual link distance. For instance, considering OOK modulation with $R_b = 5$ Mbps, a target BER of 10^{-3} and a $P_{\mathrm{Tx},e} = 65\mathrm{mW}$, the LBI is around 45.7 m, as shown in the figure.

From Fig. 3.9, we notice that using $P_{\mathrm{Tx},e} = 125\mathrm{mW}$, OOK achieves a maximum transmission distance $Z_{\max}$ =59.2m, while only reaches $Z_{\max}$ =52.3m in the case of $P_{\mathrm{Tx},e} = 65\mathrm{mW}$. We can also analyze the NLD caused by SiPM from the same figure. In general, the saturation appears when the Tx is close to Rx, since the channel's attenuation increases along with the distance. In the NLD zone from Fig.3.7, the number of photons decreases linearly with characteristics that are the inverse of that of the linear zone, which explains the BER = 1 in short distances.

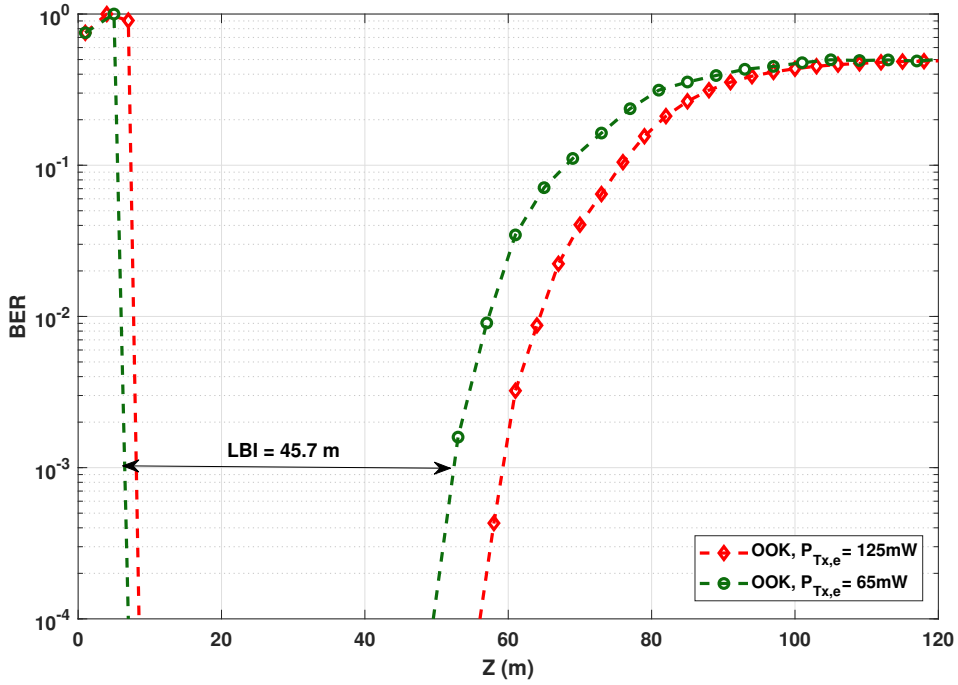

Figure 3.9 — BER as a function of Z using OOK for $P_{Tx,e} = 65\mathrm{mW}$ and 125mW; $R_b = 5$ Mbps

Let us now study the impact of data rate on the performance of OOK modulation. For this, we fix $P_{\mathrm{Tx},e} = 125\mathrm{mW}$ and we variate the data rate of $R_b = 1, 5, 10, 15$ and

20 Mbps. As expected, for increased R_b, the BER performance degrades due to the decreased signal-to-noise ratio (SNR) as a result of shorter symbol duration, and also due to increased ISI as shown in Fig. 3.10. For instance, for BER $= 10^{-3}$, the maximum transmission distance $Z_{\max}$ is around 73.7, 59.2, and 49.5 m for OOK with R_b = 1, 5, and 10 Mbps, respectively. For R_b = 20 Mbps that is much higher than the aggregate channel BW, the link with OOK effectively becomes nonoperational. (The LBIs and $Z_{\max}$ for the different R_b values are summarized in Table 3.3).

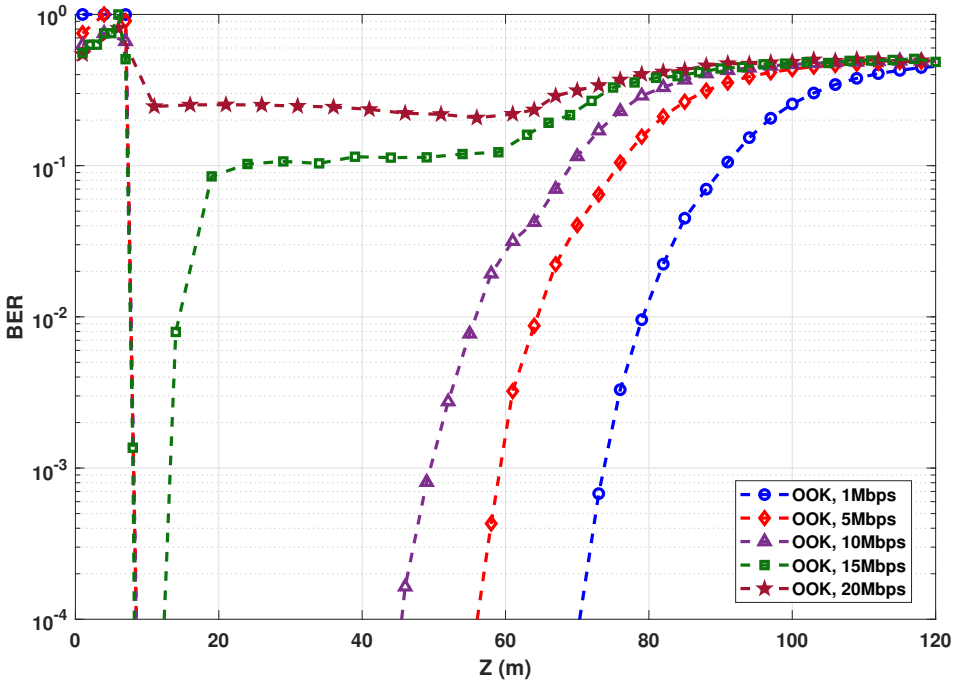

Figure 3.10 — BER as a function of Z using OOK; $R_b = 1, 2, 5$ and 10 Mbps; $P_{\mathrm{Tx},e}$ = 125mW.

3.4 Conclusion

In this chapter, we discussed the use of SiPM in UWOC applications since it has shown good potentials from the literature presented earlier. We also explained the working principle and the performance parameters of SiPMs, including shot noise, which is the most dominating noise using this PD. We then explained that SiPM could be considered as a counting device; a Poisson distribution models the number of counted photons,

Table 3.3 — LBI and maximum attainable range for OOK according to Fig. 3.10; $P_{\mathrm{Tx,e}} = 125\,\mathrm{mW}$, $\mathrm{BER} = 10^{-3}$.

R_b (Mbps)	LBI (m)	Z_{max} (m)
1	65.6	73.7
5	51.1	59.2
10	41.4	49.5
15	5.1	13.2
20	-	-

which is proportional to the received optical signal intensity operating in a linear mode. Next, we studied the effect of the non-linear distortion of SiPM and how it impacts the number of received photons. Later, we studied the performance of SiPM in UWOC using a simple OOK modulation scheme and showed that the LBI and $Z_{\max}$ values depend on $P_{\mathrm{Tx},e}$. Finally, we showed that for a higher R_b, the performances degrade as a result of a shorter T_s. In the case of R_b= 10 Mbps, the link becomes non-operational because the BW used is larger than the aggregate channel BW.

The shot noise variance depends on the intensity of the received signal since its modeled by Poisson distribution. Consequently, the optimal value of the threshold detection given above in OOK modulation is not precise. When using multi-level modulation schemes, symbol detection must be handled cautiously; the variance of the receiver noise increases when intensity levels are high, therefore symbols with high intensity are more at risk of having more errors during detection than low-intensity symbols [32]. Noise-dependency can be prevented by performing the so-called square root transformation (SQRT) [32, 74], which will prevent system performances deterioration. The SQRT helps to ensure uniformity of noise effect for all transmitted intensity levels.

Addressing the issues outlined above, we will concentrate on the next chapter on O-OFDM and its application, which allows the use of a simple channel equalization on the Rx side to overcome the aggregated channel limitation, which means that O-OFDM is capable of improving link performances compared to other SCM schemes. It is also worth mentioning that it has been proven in [74] that the noise can be considered signal-independent when using O-OFDM signaling, which makes it a better candidate for UWOC systems with SiPM receivers.

CHAPTER 4

Optical OFDM for UWOC systems

4.1 Introduction

One efficient approach to deal with channel frequency-selectivity is to use optical orthogonal frequency-division multiplexing (O-OFDM). O-OFDM is popular in indoor visible light communication (VLC) systems [75] and is proposed as a basis for evolving standards [18, 76]. Among the most popular techniques proposed in the literature so far, we principally focus on DC-biased and asymmetrically-clipped O-OFDM (DCO- and ACO-OFDM), which will be detailed later.

Due to the use of IM/DD signaling, the transmitted signal must be strictly positive and real. Therefore, most proposed O-OFDM schemes impose the Hermitian symmetry constraint in the frequency domain to obtain a real signal in the time domain [77]. In order for DCO-OFDM to ensure unipolarity of the transmitted signal, a DC bias is added to the signal before upper and lower clipping, which results in a relatively high spectral efficiency at the cost of a lower power efficiency. In ACO-OFDM, on the other hand, only the odd sub-carriers are modulated, resulting in a time-domain signal with anti-symmetry property. After applying hard clipping to the negative part, the resulting clipping noise does not affect the modulated sub-carriers. Nevertheless, this incurs a spectral efficiency loss of factor 2, compared to DCO-OFDM, but provides a better power efficiency [78].

An alternative technique to ACO-OFDM is the so-called flip-OFDM [79], also known as U-OFDM [80–82], which consists of transmitting the positive amplitude portions of the signal followed by the flipped negative amplitude portions, separated by a cyclic prefix (CP) to avoid interference between the negative and positive blocks. Compared

to ACO, the effective Rx noise variance for signal detection is doubled, but the Rx has a lower computational complexity. Another proposed alternative to ACO-OFDM (with the same spectral efficiency), is the so-called pulse-amplitude-modulation discrete-multi-tone (PAM-DMT) [83], by which PAM symbols are converted to imaginary signals before applying the Hermitian symmetry. However, the resulting high signal PAPR can cause a significant performance degradation, given the limited DR of the Tx opto-electronic components (mainly the emitter and its driver).

Several works have considered the use of O-OFDM for UWOC links, where a simple single-tap equalizer can be used to equalize the frequency-selective aggregate channel. These latter approaches have been primarily applied experimentally in clear underwater environments with a LD Tx and DCO-OFDM signaling. For instance, a data rate of 1.45 Gbps over a range of 4.8 m was reported in [37] based on pre-emphasized O-OFDM symbols and using an APD at the Rx, attaining a BER of 9.1×10^{-4}. A similar approach was used in [36] while adjusting the LD bias, where a data rate of 4.8 Gbps with a BER of 2.6×10^{-3} was reported over 5.4 m. Using a power-loading technique [84] at the Tx and a simple PIN PD with a lens at the Rx, a data rate of 1.3 Gbps over 6 m was achieved in [40] with a BER of 2×10^{-3}. In [44], using power-loading and pre-emphasizing at the Tx and a PIN PD with a lens at the Rx, a 12.4 Gbps link was established over 1.7 m. Furthermore, using an LED and without power-loading, [42] demonstrated a 161 Mbps data rate over 2 m using a PIN PD and a pair of focusing lenses, achieving a BER of 2.5×10^{-3}.

On the other hand, downlink/uplink transmission was considered in [38] over 26 m, including a 5 m air and a 21 m water channel, where a 5.5 Gbps data rate with BER $\approx 2 \times 10^{-3}$ was achieved using power-loading at the Tx with an APD at the Rx. This experiment was repeated in [85] using an SiPM with a plano-convex lens at the Rx, where a data rate of 312 Mbps was achieved with a BER of $\sim 3 \times 10^{-3}$.

This chapter aims to assess the limitation of highly sensitive SiPM receivers when using O-OFDM signaling, specifically DCO-OFDM. For this, we consider the use of an LED at the Tx with an SiPM at the Rx since it has the obvious advantage of allowing significant range extension compared to PIN or APD counterparts on the one hand, and operational robustness and implementation simplicity compared to PMTs (see Chapter 3). Given the limited DR of an SiPM, which primarily impacts Rx performance at relatively short ranges [22, 23], the use of O-OFDM signaling could impose further limitations in practice. To the best of our knowledge, the performance of an SiPM-based Rx with O-OFDM signaling, taking into account the limited DRs of the Tx and the Rx,

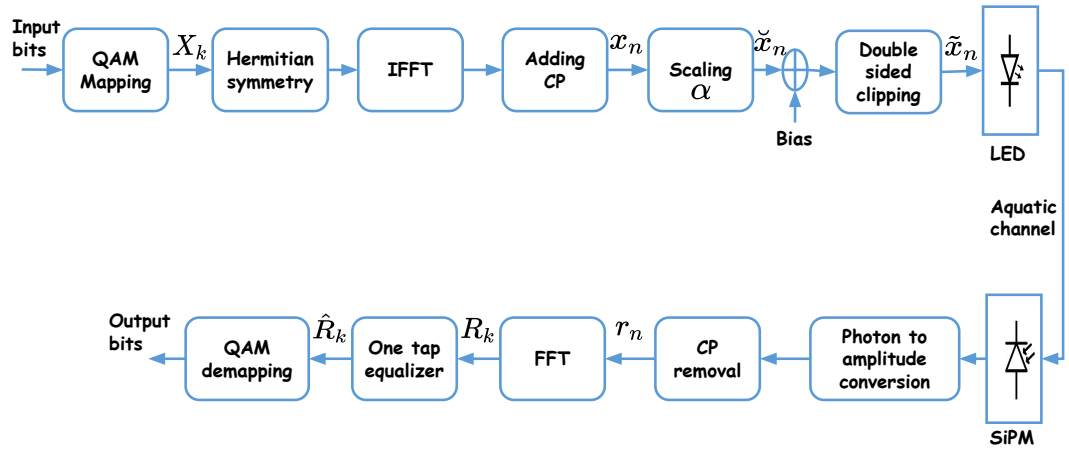

Figure 4.1 — Block diagram of the DCO-OFDM signaling scheme.

has not been investigated in detail so far.

More specifically, we study the performance of DCO-OFDM technique for a given electrical power at the Tx, as it directly impacts the underwater unit's power consumption, which is crucial in underwater missions. As the bias value takes most of the transmit electrical power, we also investigate the interest of an optimization algorithm to calculate the DC bias, considering the LED I-V characteristics. Moreover, we study the impact of SiPM dark current rate and LED non-linearity on the link performance.

The remainder of this chapter is organized as follows. Section 4.2 presents the DCO-OFDM technique. Then, in Section 4.3, we describe signal adaptation to LED DR and the methods used to calculate DC bias. Next, a set of numerical results is presented in Section 4.4 to study the performance of an SiPM-based system. The impact of SiPM DCR and LED non-linearity on the link performance are investigated in Section 4.5 and Section 4.6, respectively. Lastly, Section 4.7 concludes the chapter.

4.2 DCO-OFDM

Figure 4.1 shows the block diagram of DCO-OFDM signaling for a typical SiPM-based UWOC link. First, blocks of input data bits are mapped into M-QAM (complex) symbols X_k, $k = 0, 1..., N-1$, which are then passed through an IFFT block generating the "time-domain" OFDM signal x_n:

$$x_n = \frac{1}{\sqrt{N}} \sum_{k=0}^{N-1} X_k \exp\Big(j\frac{2\pi}{N}nk\Big), \quad n = 0, ..., N-1. \tag{4.1}$$

As explained previously, to ensure that x_n is real, Hermitian symmetry is imposed on X_k symbols before IFFT such that [77]:

$$\begin{cases} X_0 &= X_{N/2} = 0, \\ X_k &= X^*_{N-k}, \qquad 0 < k < N/2, \end{cases}$$

where .* denotes complex conjugate. After IFFT, a CP is added to each block to avoid ISI as a result of the delay spread τ_0 of the aggregate channel. The length of the CP, N_{CP}, is set as to be larger than τ_0/T_s, where T_s is the OFDM symbol duration, allowing hence to restore the signal at the Rx using a one-tap equalizer. Afterwards, a scaling factor α is applied to the signal in order to adequately fit it to the LED DR (this will be further clarified latter in Section 4.3); the resulting signal is denoted by $\breve{x}_n = \alpha x_n$. Next, to obtain a positive signal, a DC bias is added to $\breve{x}_n$ before upper and lower clipping due to the limited LED DR, which gives rise to the so called "clipping noise." The resulting double-side clipped signal is denoted by $\tilde{x}_n$.

Without loss of generality, we consider driving the LED with a voltage, i.e., x_n, $\breve{x}_n$, and $\tilde{x}_n$ are all in units of Volts. Note that this is not restricting, as there is a bijection relationship between the input current and voltage of the LED, as described in Section 3.3.1.

After being transmitted through the aquatic channel, the received optical intensity at the Rx is converted to an electrical signal. "Photon to amplitude conversion" performs the conversion of the number of generated photo-electrons at the SiPM output to an electrical signal amplitude [23]. Here, it is obtained by multiplying C_{ph} by the photon energy E_p. Afterwards, after removing the CP, the recovered time-domain OFDM symbols r_n are passed through an FFT block whose output is given by:

$$R_k = \frac{1}{\sqrt{N}} \sum_{n=0}^{N-1} r_n \exp\Big(-j\frac{2\pi}{N}nk\Big), \quad k = 0, ..., N-1. \tag{4.2}$$

The obtained signals $\hat{R}_k$ after equalization of the aggregate channel are then passed to the QAM-demapping block to recover the transmitted bits.

An important point here concerns QAM signal demodulation since the Rx is obviously shot noise limited due to the use of an SiPM. As mentioned before in chapter 3, it has been shown in [74] that for the case of O-OFDM signaling, although the time-domain signal r_n at the Rx (before the FFT block in Fig. 4.1) is affected by signal-dependent noise, for the frequency-domain signal (i.e., R_k at the output of the FFT block) the noise is independent of the signal (see Appendix A). As a result, conventional QAM demodulation can be used in our case, that is, by assuming an effectively signal-independent noise.

Assuming M-QAM constellation for X_k, the spectral efficiency of DCO-OFDM is given by:

$$\gamma_{\text{DCO}} = \frac{\log_2 M \ (N-2)}{2\,(N+N_{\text{CP}})} \quad \text{(bps/Hz)}. \tag{4.3}$$

4.3 Adapting the Signal Amplitude to the LED dynamic rang

In practice, before intensity modulation of the LED, the signal needs to be fit to the LED I-V characteristics, or in other words, to its DR. Figure 3.8 shows the I-V characteristics of the LED that we consider in this work [5]. Unless otherwise specified, we ignore the I-V non-linearity within the LED DR and consider the approximate linearized characteristics (the red plot in Fig. 3.8) in the sequel.

Firstly, power-normalized QAM constellations are considered, see Fig. 4.1. It can be shown that the signal x_n after IFFT is also power normalized, i.e., $\mathbb{E}\left\{x_n^2\right\} = 1$, where $\mathbb{E}\{.\}$ denotes the expected value. After adding the CP, the scale of the signal is changed by multiplication by a factor α to obtain $\breve{x}_n$. Afterwards, the DC bias, denoted by B_{DC}, is added to it.

$P_{\text{Tx,e}}$ primarily depends on the scaling factor α and the DC bias B_{DC}. Having fixed these two parameters, we calculate $P_{\text{Tx,e}}$ by averaging the power corresponding to each symbol, which is obtained from its product by the bijective current according to the linearized LED I-V characteristics. We consider two ways to set the bias, as explained in the following.

4.3.1 Method 1 (Classical approach)

Firstly, as a simple method, we use the classical approach of considering the so-called *clipping factor* $\mathcal{K}$ [86], which is defined in the following equation, where the effect of the scaling factor is taken into account:

$$B_{\rm DC} = \mathcal{K}\sqrt{\mathbb{E}\{\breve{x}_n^2\}} + V_{\min} \approx \mathcal{K}\,\alpha + V_{\min}. \tag{4.4}$$

In the sequel, the clipping factor in decibel is used, i.e., $\mathcal{K}_{\rm dB} = 10\,\log_{10}\mathcal{K}$.

4.3.2 Method 2 (Optimal approach)

As a second approach, we consider the approach in [87] to calculate the the optimum value of $B_{\rm DC}$ so as to minimize the mean square error $\mathcal{E}$ between $\breve{x}_n$ and double-side clipped signal $\tilde{x}_n$, while taking $V_{\min}$ and $V_{\max}$ of the LED into consideration, where

$$\mathcal{E} = \mathbb{E}\left\{\sum_{n=0}^{N-1}(\tilde{x}_n - \breve{x}_n)^2\right\}. \tag{4.5}$$

For given α, $V_{\min}$, and $V_{\max}$, the optimum bias is calculated numerically by setting $\partial\mathcal{E}/\partial B_{\rm DC}$ to zero.

Assuming a large enough N, the time-domain signal x_n can be modeled as a zero-mean independent identically-distributed Gaussian random variable with the standard deviation σ_x, based on the Central Limit theorem. Therefore, from (4.5), $\mathcal{E}$ can be expressed by [87]:

$$\begin{aligned}\mathcal{E} \;=\; & N\,\Big[V_{\min}^2\Phi(L) + (B_{\rm DC}^2 + \sigma_{\breve{x}}^2)\big(\Phi(U) - \Phi(L)\big)\\ & +2\,B_{\rm DC}\,\sigma_{\breve{x}}\big(\Phi(L) - \Phi(U)\big) + \sigma_{\breve{x}}^2\,L\big(\phi(L) - \phi(U)\big)\\ & +V_{\max}^2\,\big(1 - \Phi(U)\big) + \sigma_{\breve{x}} - 2\,R_{\tilde{x}_n\breve{x}_n}\Big],\end{aligned} \tag{4.6}$$

where $\sigma_{\breve{x}}$ denotes the standard deviation of $\breve{x} = \alpha x_n$, and $R_{\tilde{x}_n\breve{x}_n}$ is the covariance of $\tilde{x}_n$ and $\breve{x}_n$. Also,

$$\begin{cases} U & = (V_{\max} - B_{\rm DC})/\sigma_{\breve{x}} \\ L & = (V_{\min} - B_{\rm DC})/\sigma_{\breve{x}} \\ \Phi(y) & = \frac{1}{\sqrt{2\pi}}\int_{-\infty}^{y}\exp(-u^2/2)du \\ \phi(v) & = \frac{1}{\sqrt{2\pi}}\exp(-v^2/2). \end{cases} \tag{4.7}$$

The optimal bias can be obtained by taking the partial derivation of (4.6) with respect to B_{DC} and setting the result to zero [87]:

$$\frac{\partial \mathcal{E}}{\partial B_{\mathrm{DC}}} = 2B_{\mathrm{DC}}\big(\Phi(U) - \Phi(L)\big) + 2\,\sigma_x\big(\phi(L) - \phi(U)\big) = 0. \tag{4.8}$$

Note that, in theory, solving (4.8) may result in several local minima, that should be between $V_{\min}$ and $V_{\max}$. The optimum B_{DC} should be selected so as to result in the global minimum $\mathcal{E}$ from (4.6). Here, we calculate numerically the optimum bias from (4.8) for given α, $V_{\min}$, and $V_{\max}$. Also, according to the assumption of power-normalized x_n, $\sigma_x = 1$, and consequently, $\sigma_{\breve{x}} = \alpha$.

Unless otherwise specified, we consider the first approach in the presented thesis, that is, the bias is set by considering a clipping factor $\mathcal{K}_{\mathrm{dB}}$.

4.4 Performance Study of the UWOC Link

Considering real characteristics of practical components, a set of numerical results is provided in this section to study the performance of DCO-OFDM technique considering the Tx, channel and SiPM parameters presented in Table 3.1 and Table 3.2.

We consider a 4-QAM signal constellation, which results in a spectral efficiency of $\eta \approx 1\,\mathrm{bps/Hz}$. Also, the number of sub-carriers $N = 1024$ by default, which results in an effectively flat channel per sub-channel for the considered data rates. Depending on R_b, the CP length N_{CP} is set appropriately (i.e., large enough, compared to the aggregate channel delay spread) in order to avoid ISI. Lastly, The BW of the aggregate channel is determined by those of the SiPM ($\sim 4\,\mathrm{MHz}$), the LED ($\sim 10\,\mathrm{MHz}$), and the aquatic channel.

4.4.1 Comparison with OOK

First of all, in order to elucidate the real interest of O-OFDM signaling, let us compare the performances of DCO-OFDM and OOK modulation schemes (details on OOK signaling in Section 3.3.2) for a typical scenario. In Fig. 4.2 BER plots as a function of link distance are presented, considering an electrical transmit power of $P_{\mathrm{Tx,e}} = 125\,\mathrm{mW}$.

First, notice a high BER for very short link ranges (e.g., $Z \lesssim 8\,\mathrm{m}$ for OOK), which is due to SiPM saturation [22, 32]. For relatively large link ranges (e.g., $Z \gtrsim 45\,\mathrm{m}$ for OOK at $R_b = 10\,\mathrm{Mbps}$), the BER reasonably increases due to decreased SNR as a result of channel attenuation.

Table 4.1 — LBI and maximum attainable range for OOK and 4-QAM DCO-OFDM transmission schemes according to Fig. 4.2; $P_{\mathrm{Tx,e}} = 125\,\mathrm{mW}$, $\mathrm{BER} = 10^{-3}$.

	R_b (Mbps)	LBI (m)	$Z_{\max}$ (m)
DCO	1	106.6	118.8
	5	92.8	105
	10	86.4	98.8
	15	82.2	94.4
	20	78.9	91.3
OOK	1	65.6	73.7
	5	51.15	59.2
	10	41.4	49.5
	15	5.1	13.2
	20	-	-

As expected, for increased R_b, the BER performance degrades due to the decreased SNR as a result of shorter symbol duration, and also (for the case of OOK) due to increased ISI. As explained in Section 3.3.2, for OOK, the link becomes non-operational when using $R_b \gtrsim 15$ Mbps. However, DCO-OFDM is robust against channel frequency selectivity and even for $R_b = 20\,\mathrm{Mbps}$ we obtain a relatively large $Z_{\max}$. On the other hand, the BER performance is affected more by SiPM saturation due to the higher PAPR and the more complex waveform compared to OOK, which explains the saturation limit at slightly larger distances (i.e., around 12 m at $\mathrm{BER} = 10^{-3}$). Nevertheless, DCO remains quite advantageous in terms of LBI. For instance, for $R_b = 1\,\mathrm{Mbps}$, the LBI is $\sim 107\,\mathrm{m}$, in contrast to $\sim 65.5\,\mathrm{m}$ for OOK. LBI and $Z_{\max}$ for the different R_b values are summarized in Table 4.1.

4.4.2 Impact of Bias Selection for DCO-OFDM

We provide in this Section the impact of DC bias selection for the case of DCO-OFDM signaling. For this, we consider $P_{\mathrm{Tx,e}} = 50\mathrm{mW}\, R_b = 20\,\mathrm{Mbps}$, and 4-QAM signal constellation. We have compared in Fig. 4.3 the BER performance when using the optimal bias, with the case where B_{DC} is calculated based on considering a clipping factor, see Section 4.3. It can be clearly seen that the best energy efficiency is obtained for the case of optimized bias. For $\mathcal{K}_{\mathrm{dB}} = 7\,\mathrm{dB}$, the BER performance is relatively close to the

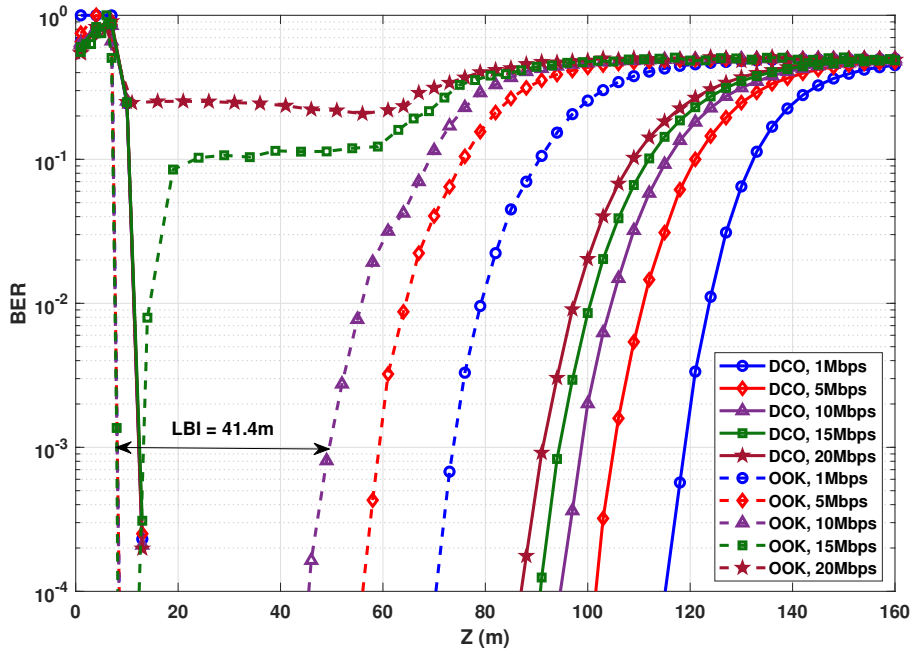

Figure 4.2 — BER comparison of OOK and DCO-OFDM (with 4-QAM) for $P_{\mathrm{Tx,e}} = 125\,\mathrm{mW}$. $N = 1024$. $N_{\mathrm{CP}} = 2$, 2, 3, and 5, for $R_b = 1$, 2, 5, and 10 Mbps, respectively.

optimum bias case. Indeed, for a too low $\mathcal{K}_{\mathrm{dB}}$, the performance is limited by the clipping noise, whereas for a relatively large $\mathcal{K}_{\mathrm{dB}}$, the system suffers from a poor energy efficiency due to using a too large bias.

Although the interest of optimal bias setting is obvious, its calculation (which is done numerically, see Section 4.3) needs a high precision (and therefore, a high computational cost), which is explained in detail in Section 4.4.4. Therefore, in the case of changing transmit power, for instance, in an adaptive UWOC transmission system, where the bias needs to be adjusted dynamically (based on the estimated channel state information), it would be preferable to fix the bias simply by setting the clipping factor.

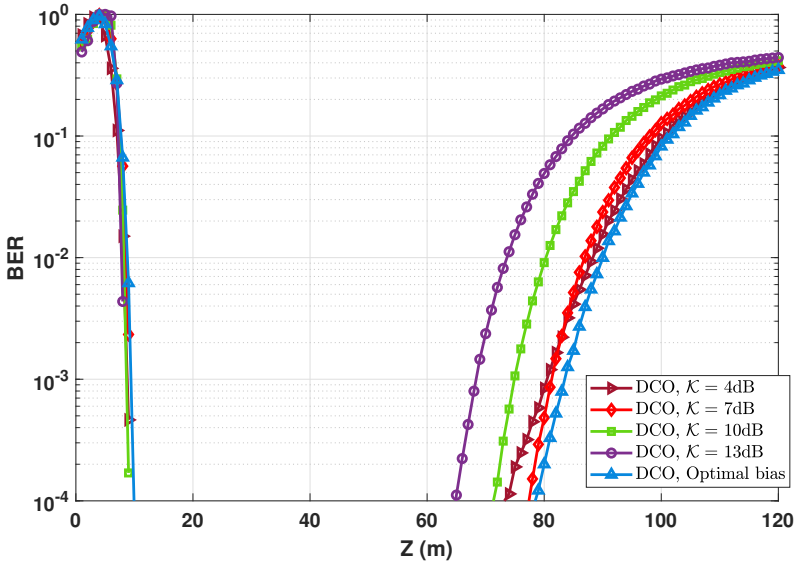

Figure 4.3 — BER performance of DCO-OFDM using optimized and non-optimized DC bias. One LED at the Tx with $P_{\mathrm{Tx,e}} = 50\,\mathrm{mW}$; $N = 1024$; $N_{\mathrm{CP}} = 9$; $R_b = 20\,\mathrm{Mbps}$. The corresponding clipping factors are $\alpha = 0.12$ for the optimum bias (corresponding to $B_{\mathrm{DC}} = 2.932$), and $\alpha = 0.145$, 0.0922, 0.062, and 0.0432 for $\mathcal{K}_{\mathrm{dB}} =$ 4, 7, 10, and 13 dB (corresponding to $B_{\mathrm{DC}} = 2.9279$, 2.9344, 2.9357, and 2.9377 V), respectively.

4.4.3 Performance of DCO-OFDM with Optimal and Non-optimal DC Bias

To explain in more detail the behavior for the optimal bias with increased transmit power, we have shown in Fig. 4.4 the color maps of Z versus $P_{\mathrm{Tx,e}}$ for the case of $R_b = 20\,\mathrm{Mbps}$ with $\eta \approx 1\,\mathrm{bps/Hz}$ for the cases of optimal bias and classical bias setting with $\mathcal{K} = 7\,\mathrm{dB}$. These results require careful interpretation, as explained in the following.

For the case of optimal B_{DC}, by increasing $P_{\mathrm{Tx,e}}$, the optimal bias increases until it attains nearly the middle of the LED characteristics, i.e., $V_{\mathrm{av}} = (V_{\max} + V_{\min})/2 = 3.39\,\mathrm{V}$. After this limit, if the transmit power is further increased, B_{DC} remains almost unchanged, but instead, the scaling factor is increased to account for increased transmit power. This results in an increased clipping noise level and a BER deterioration consequently. Meanwhile, fixing the maximum B_{DC} at V_{av} will make the signal be clipped "symmetrically" from upper and lower sides.

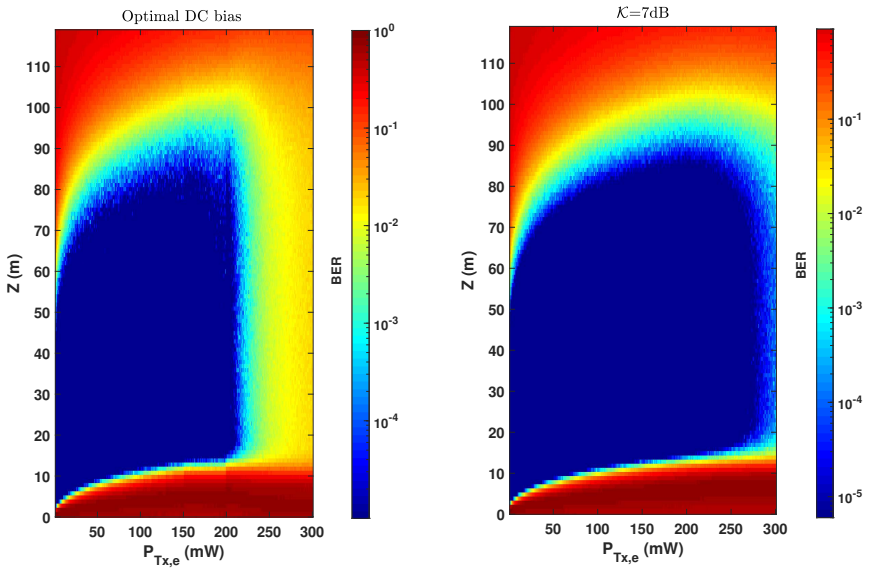

Figure 4.4 — Comparison of the BER performance for DCO-OFDM: Optimal DC bias (HP); DC bias obtained by setting a clipping factor of 7 dB; DC bias obtained by setting $\mathcal{K} = 7\,\text{dB}$ but limited to 3.9 V. $N = 1024$; $N_{\text{CP}} = 9$; $R_b = 20\,\text{Mbps}$, $\eta \approx 1\,\text{bps/Hz}$.

For the classical method, from Section 4.3, B_{DC} increases steadily by increasing the transmit power. For too large $P_{\text{Tx,e}}$, signal will primarily suffer from upper clipping. Meanwhile, increasing $P_{\text{Tx,e}}$ will result mainly in increased B_{DC}. Hence, since α is smaller, the BER will not deteriorate as one can see for the case of optimal bias. Note that this does not mean an advantage for the classical biasing: the increased $P_{\text{Tx,e}}$ does not result in an improvement of $Z_{\max}$ or LBI. In other words, in the sense of energy efficiency, in either case, $P_{\text{Tx,e}}$ should not exceed a certain maximum transmit power. Overall, the interest of optimal bias setting is that it results in a larger LBI and $Z_{\max}$.

4.4.4 Required Precision for Calculating the Optimal Bias for DCO-OFDM

As explained in Section 4.4.2, although the optimized DC bias provides the best energy efficiency, its calculation requires high accuracy, and equivalently entails a high computational cost. This Section clarifies this issue and shows why in practice the use of optimal DC bias could be of little interest.

Remember from Section 4.3 that the optimal bias B_{DC} is calculated so as to minimize the mean square error $\mathcal{E}$. Figure 4.5 shows the partial derivation of $\partial\mathcal{E}/\partial B_{\mathrm{DC}}$ as a function of B_{DC} considering a transmit power of $P_{\mathrm{Tx,e}} = 50\,\mathrm{mW}$.

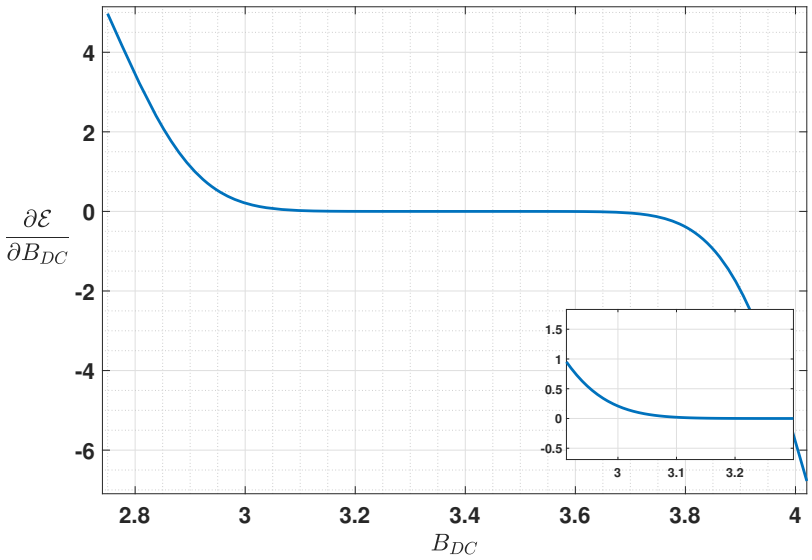

Figure 4.5 — Partial derivation of $\mathcal{E}$ with respect to B_{DC} for calculating the optimal bias for DCO-OFDM. 4-QAM modulation, $P_{\mathrm{Tx,e}} = 50\,\mathrm{mW}$; $N = 1024$; $N_{\mathrm{CP}} = 9$; $R_b = 20\,\mathrm{Mbps}$.

Notice that the derivate is very close to zero for a large range of B_{DC} (between 3 and 3.8); notice also the zoomed part in the figure. This signifies that the calculation of the exact optimal bias needs a high numerical precision. For instance, for the considered case study, we have calculated the optimal bias using a relatively low precision of 10^{-2} (the corresponding B_{DC} is ~ 2.9406, that we will refer to as LP: Low Precision), where the resulting BER performance was worse than that with a clipping factor of 7 dB. With a higher numerical precision of 10^{-5} (the corresponding B_{DC} is ~ 2.932, that we will refer to as HP: High Precision), we could attain a better performance, as can be seen from Fig. 4.6. Although calculating precisely the bias is rather straightforward for a theoretical study, it would not be the case for a practical hardware implementation of the system with limited accuracy (e.g., using pre-registered look-up tables for a set of transmit powers $P_{\mathrm{Tx,e}}$). So, in this sense, the use of optimal biasing for DCO-OFDM signaling would rather have little interest in practice.

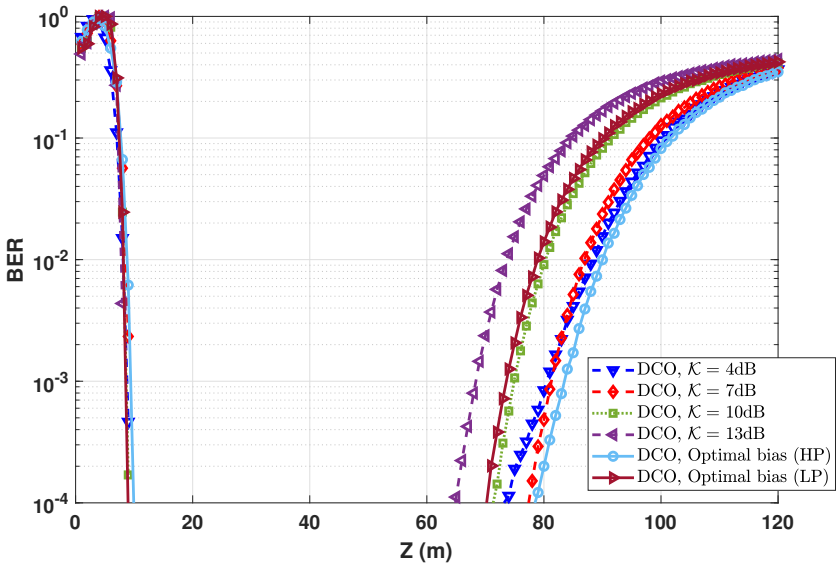

Figure 4.6 — Comparison of the BER performance for DCO-OFDM obtained using low- and high-precision (LP and HP) optimal bias calculation with those calculated based on clipping factors of 4, 7, 10, and 13 dB. $P_{\text{Tx,e}} = 50\,\text{mW}$; $N = 1024$; $N_{\text{CP}} = 9$; $R_b = 20\,\text{Mbps}$.

4.5 DCR Impact on the Link Performance

DCR is in fact, a key parameter of an SiPM, as described in Chapter 3, equation (3.10). A higher DCR can effectively modify both LBI and the maximum achievable distance. In fact, due to the relatively low DCR of the considered SiPM, the attainable operation ranges are quite larger than those with an older generation of SiPMs, e.g. [88]. (see, for instance, the numerical results presented in [22, 29, 32]).

To better see the effect of DCR on the link performance, consider 4-QAM DCO-OFDM modulation with $P_{\text{Tx,e}}$=125 mW. We keep the same Tx, channel, and Rx parameters used in previous sections, and we vary f_{DCR} at 25 kHz, 7, 70, and 700 MHz (note that the value of $f_{\text{DCR}} \approx 7$ MHz compares to Sensl MicroSB-30050 SiPM [88]). Figure 4.7 compares the BER performance as a function of link distance. We notice that switching from 7 MHz to 70 MHz costs about 9.7m loss of maximum achievable link Z_{max} for a target BER of 10^{-3}, which corresponds to an LBI loss of 9.7 m since the saturation reasonably occurs at the same Z for all f_{DCR} values.

Let us now evaluate the impact of DCR on the link distance while varying the data

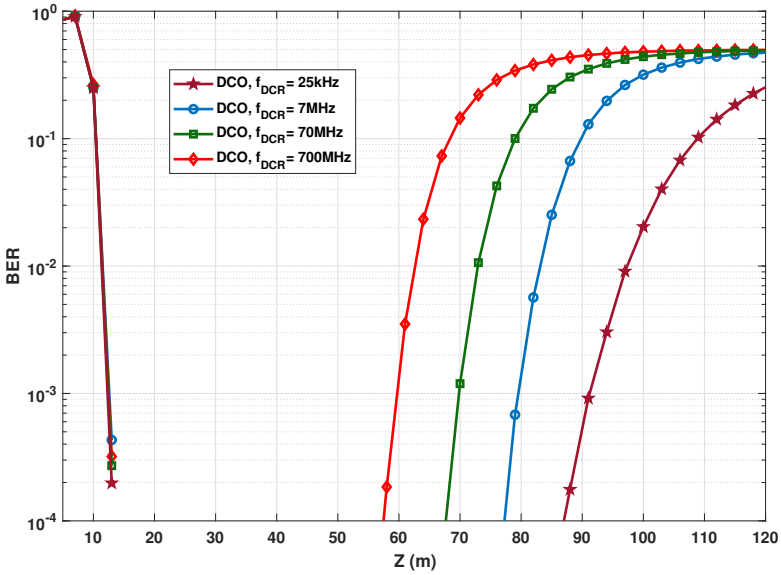

Figure 4.7 — BER performance for 4-QAM DCO-OFDM for DCR=25kHz, 7, 70, and 700MHz. $P_{\mathrm{Tx,e}} = 125\,\mathrm{mW}$; $\mathcal{K} = 7\,\mathrm{dB}$; $N = 1024$; $N_{\mathrm{CP}} = 9$; $R_b = 20\,\mathrm{Mbps}$.

rate and setting f_{DCR} to 7 and 700 MHz. Note that the increase in data rate implies the decrease of the time symbol T_s, which means the decrease of the photon counting time interval (see Chapter 3). As expected, from Figure 4.8, we notice that the difference in LBI for the two considered f_{DCR} values decreases when increasing the data rate. For instance, for $R_b = 1$ Mbps, the difference in LBI is much higher than with $R_b = 100$ Mbps (The difference in LBI is about 22.2 m, and 12.8 m for $R_b = 1$ Mbps, and $R_b = 100$ Mbps, respectively). This shows that the DCR effect on the maximum attainable link range decreases when increasing the data rate.

We conclude from these results that choosing an SiPM with a low DCR is very important to guarantee a maximum achievable link range and more system flexibility, which explains our choice to use the Hamamatsu C13366 3050GA [6] with $f_{\mathrm{DCR}} = 25$ kHz.

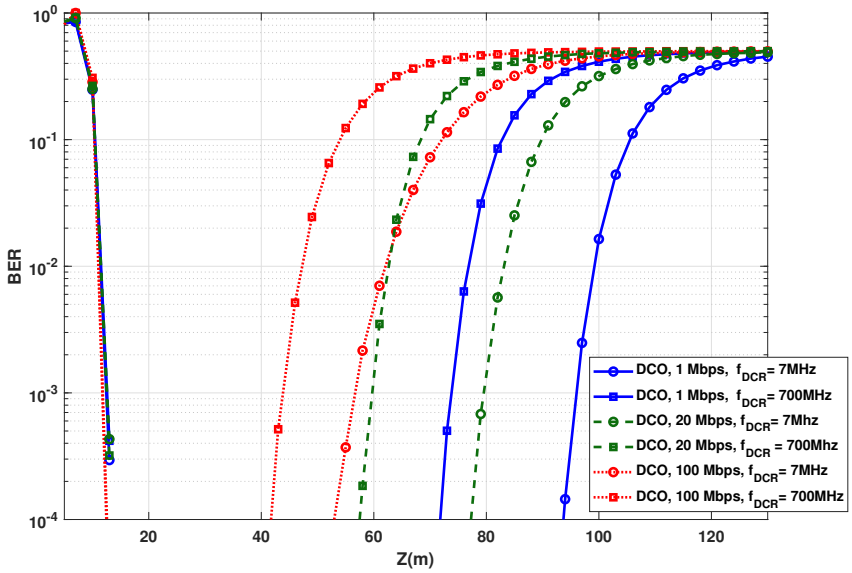

Figure 4.8 — BER performance for 4-QAM DCO-OFDM for DCR = 7 and 700MHz. $P_{\mathrm{Tx,e}} = 125\,\mathrm{mW}$; $\mathcal{K} = 7\,\mathrm{dB}$; $N = 1024$; $N_{\mathrm{CP}} = 9$; $R_b = 1, 20$ and $100\,\mathrm{Mbps}$.

4.6 LED Non-linearity Impact

So far, we consider focus on LED and SiPM DR in our study. Let us now study the impact on the link performance when considering the real non-linear LED model (blue curve in Figure 3.8). We consider a typical configuration with 4-QAM DCO-OFDM, $R_b = 20$ Mbps, and $P_{\mathrm{Tx,e}} = 50\,\mathrm{mW}$. Note that the bias and scaling factor settings will be different from those previously used in a linear model to obtain the same electrical transmit power [1]. Figure 4.9 shows the BER results for the clipping factor of $\mathcal{K}_{\mathrm{dB}} = 4$, 7, 10, and 13 dB, we notice the best performance is obtained for $\mathcal{K}_{\mathrm{dB}} = 10\,\mathrm{dB}$.

Consider the case $\mathcal{K}_{\mathrm{dB}} = 7$, corresponding to $B_{\mathrm{DC}} = 3.094$ and the DC current of 14.67 mA. Here, due to the small slope of the I-V LED curve, the LED output signal variations are very small, this signal "compressing" results in performance degradation as can be seen from Fig. 4.9. In order to skip this "lower region" of the LED characteristics, we should use a higher B_{DC}, as it is the case for $\mathcal{K}_{\mathrm{dB}} = 7$, and 13 dB.

We notice from Fig. 4.9 that $\mathcal{K} = 10\,\mathrm{dB}$ makes a good compromise between the

[1] The corresponding clipping factors for the non-linear case are $\alpha = 0.249$, 0.172, 0.121, and 0.085 for $\mathcal{K}_{\mathrm{dB}} = 4$, 7, 10, and 13 dB, corresponding to $B_{\mathrm{DC}} = 3.056$, 3.094, 3.112, and 3.12 V.

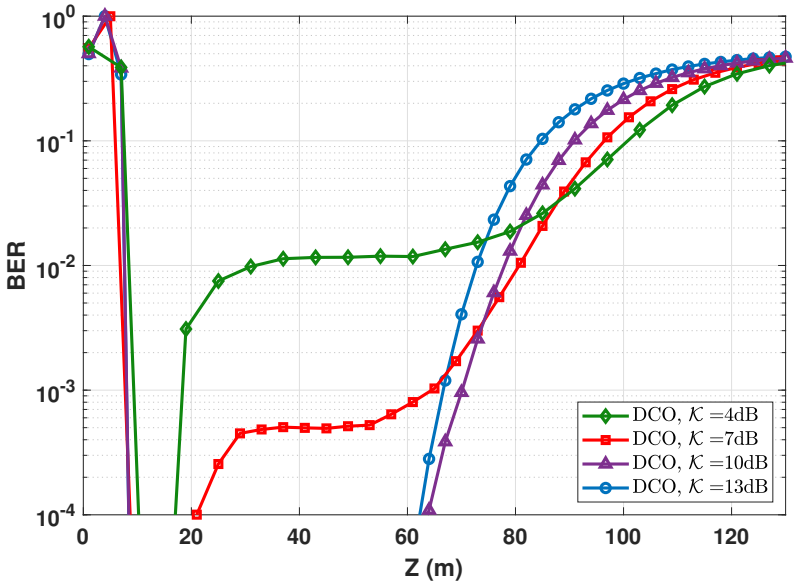

Figure 4.9 — BER performance for 4-QAM DCO-OFDM obtained using non-linear LED characteristics. $P_{\mathrm{Tx,e}} = 50\,\mathrm{mW}$; $N = 1024$; $N_{\mathrm{CP}} = 9$; $R_b = 20\,\mathrm{Mbps}$.

scaling factor and the clipping noise level. For the considered $P_{\mathrm{Tx,e}}$, The obtained LBI and $Z_{\max}$ are about 62.2 m and 70 m, respectively. Notice that, compared to the linear LED model case, the link flexibility (i.e., the LBI) loss is about 16.7 m (see Table 4.1).

4.7 Conclusion

In this chapter, we first introduced optical OFDM signaling, and then presented in more detail, the DCO-OFDM scheme. The presented numerical results confirmed a significant advantage of using O-OFDM signaling compared to amplitude modulation schemes, such as OOK in the considered UWOC application. Since power consumption is a critical factor for underwater units, we studied two approaches to set the DC bias for DCO-OFDM, taking into account the scaling factor needed to adapt the signal to the DR of the LED. We compared the use of both classical and optimal methods to fix the DC bias; the latter showed little interest in practice since it requires high computational accuracy with a marginal improvement of the system performance. Then, we showed the importance of using an SiPM with a low DCR to increase the maximum attainable link and range flexibility. Lastly, we evaluated the impact of the LED non-linearity on

the link performance. In the presented study, we did not consider any bit or power loading at the Tx in order to see better the limits of the transmission scheme.

As explained in the introduction to this chapter, the ACO-OFDM technique is more power-efficient compared to DCO-OFDM, but at the expense of a loss of factor 2 in the spectral efficiency. Other techniques have been suggested in the literature to improve ACO-OFDM spectral efficiency and to maintain its power efficiency advantage. In the following chapter, we will study the applications of ACO-based high spectral efficiency schemes (with close spectral efficiency to DCO), and will compare their performance in UWOC systems using SiPM as Rx.

CHAPTER 5

Spectrally enhanced ACO-OFDM schemes for SiPM-based UWOC links

5.1 Introduction

To improve the spectral efficiency of ACO-OFDM while preserving its power efficiency advantage, several techniques have been proposed in the literature so far. In [89], enhanced U-OFDM (eU-OFDM) was proposed, which combines multiple U-OFDM signals at the Tx (by sending them on different "depths") and performs iterative detection at the Rx based on successive interference cancellation to remove the interference between the signals of different depths. The proposed ADO-OFDM [90], uses ACO on odd sub-carriers and DCO signaling on even sub-carriers. The HACO-OFDM [91] is similar to ADO but uses PAM-DMT on even sub-carriers (instead of DCO), where the negative part of the corresponding signals is clipped before transmission (more details on HACO and ADO will be provided in the following section). The recently proposed LACO-OFDM uses the "uncoded" sub-carriers in an ACO-OFDM scheme through the use of several data transmission layers (see Section 5.2.2 for more details), resulting in an improved spectral efficiency [92]. LACO-OFDM has also the advantage of more flexibility, in the sense that the overall transmission data rate and performance can be adjusted by setting independently the signal constellation size and the allocated power within each layer.

Another proposed scheme, called hybrid PAM-DMT (HPAM-DMT) [93], uses a similar concept as LACO, where the transmitted signal is composed of different "groups"

of signals: the first group consists in a real PAM-DMT (RPAM-DMT) signal, and the successive groups are obtained from RPAM-DMT modulated signals sent on specific sub-carriers. The advantage of HPAM-DMT over LACO is its lower computational complexity at the Rx, but this comes at the drawback of a lower power efficiency.

A more detailed comparison of the above-mentioned techniques can be found in [94–96]. In particular, it was shown in [96] that the two-layer LACO and HACO are more power-efficient compared to ADO for a given spectral efficiency. For a spectral efficiency of larger than ~ 4 bps/Hz, the four-layer LACO-OFDM outperforms the other proposed hybrid schemes in terms of power efficiency [96].

Our aim in this chapter is to quantify the performance of three techniques of LACO-OFDM, HACO-OFDM, and ADO-OFDM, and to compare their performances with these of DCO-OFDM, ACO-OFDM. To compare the performances of these schemes, we mostly fix the electrical power at the Tx, as it impacts directly the power consumption of the underwater unit, which is of crucial importance in underwater missions. We take into account the required DC-bias (to minimize the clipping noise) for the five considered schemes, given the LED characteristics. Indeed, the required DC bias for ACO-, HACO-, and LACO-OFDM in practice is commonly neglected in the related theoretical works, which could affect the general conclusions on the choice of the appropriate transmission technique. Taking into account the effects of upper and lower signal clipping at the Tx, SiPM saturation at the Rx at relatively short ranges, and beam attenuation in water, we show that, overall, ACO-OFDM has an undeniable advantage over the two other schemes in terms of energy efficiency for low-to-moderate spectral efficiencies. However, DCO-OFDM allows a higher flexibility (i.e., provides a good tolerance) in terms of operational range when relaxing the constraint on the transmit power. Meanwhile, we show that LACO-OFDM makes a good compromise between energy efficiency and operational range flexibility. Furthermore, we show that HACO-OFDM offers almost the same performances as LACO for a spectral efficiency of ~ 1 bps/Hz. However, HACO link performances degrade as the data rate increases; on the other hand, ADO offers the lowest LBI and $Z_{\max}$ among all the considered O-OFDM schemes.

The remainder of this chapter is organized as follows. In Section 5.2, details about the considered O-OFDM techniques are presented. Next, numerical results are presented in Section 5.3 to study the performance of an SiPM-based system. Lastly, Section 5.4 concludes the chapter.

5.2 Description of the Considered Signaling Schemes

5.2.1 ACO-OFDM

In ACO-OFDM, data is sent only on odd sub-carriers. After applying the Hermitian symmetry, the resulting transmitted frame of symbols (before IFFT) has the following form:

$$\left[0,\, X_0,\, 0,\, X_1,\, 0, ..., X_{N/4-1},\, 0,\, X^*_{N/4-1},\, 0, ..., X^*_1\,\right].$$

This way, after IFFT, the negative part of x_n can be clipped without loss of information [86]. The other steps are similar to what described for DCO-OFDM in the previous chapter (see Section 4.2). Note that, as we will explain later, in practice, a DC bias should still be added to $\breve{x}_n$ after adding the CP and scaling, in order to account for the LED I-V characteristics.
Considering an M-QAM signal constellation for X_k, the spectral efficiency of ACO-OFDM is:

$$\gamma_{\text{ACO}} = \frac{\log_2 M \;\; N}{4\,(N + N_{\text{CP}})} \quad \text{(bps/Hz)}. \tag{5.1}$$

5.2.2 LACO-OFDM

The general block diagram of LACO-OFDM is shown in Fig. 5.1. The transmitted signal is obtained as the superposition of L frames of symbols, each one corresponding to a "layer." Within each layer, the signaling principle is similar to ACO-OFDM, as explained in the following [92, 97].

- For the first layer, ACO-OFDM signaling is used where $N/4$ symbols and their complex conjugates (according to the Hermitian symmetry requirement) are sent on the odd sub-carriers $2q+1$ with $q = 0, 1, .., N/2-1$. These are then transformed into time domain after N point IFFT.

- For the subsequent layers, the corresponding frames are mapped onto the remaining even sub-carriers:

- For the second layer, $N/8$ symbols and their complex conjugates are sent on sub-carriers $2(2q+1)$ with $q = 0, 1, ..., N/4-1$; they are transformed into time domain after N-point IFFT, while the amplitudes of the remaining sub-carriers are set to zero.

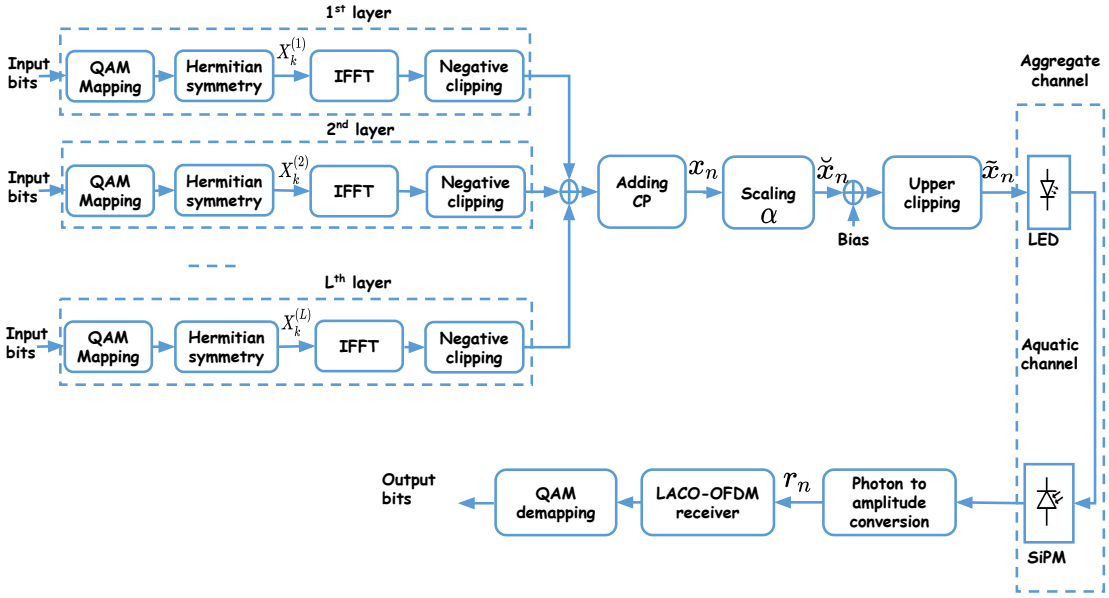

Figure 5.1 — Block diagram of LACO-OFDM signaling with L layers.

- In general, for the ℓ^{th} layer, $\ell > 1$, $(N/2^{\ell+1})$ symbols and their complex conjugates are sent on sub-carriers $2^{\ell-1}(2q+1)$ with $q = 0, 1, ..., N/2^{\ell+1} - 1$. Then, setting the amplitudes of the remaining sub-carriers to zero, they are transformed into time domain after N-point IFFT.

Note that the constellation size in each layer can be adjusted to result in a desired overall data-rate R_b (in bps). Afterwards, the time-domain signals of the L layers are superimposed before adding the CP, applying scaling, adding a bias, and clipping, as shown in Fig. 5.1. Here, lower clipping of the time-domain signal will generate distortion in the frequency domain, which concerns those sub-carriers unused for a given layer [97]. Nevertheless, since this affects the even sub-carriers, only signals of the layers $\ell \geq 2$ are distorted. For a given sub-carrier used in the ℓ^{th} layer, the resulting distortion from all lower layers will be added to the transmitted signal in the frequency domain. For example, the third layer uses sub-carriers $4, 12, ..., (N/16)$, which will be affected by distortion from layers 1 and 2.

To recover the transmitted data, iterative detection is done at the Rx, as proposed in [92], where symbols are recovered layer by layer in an iterative way from r_n, as shown in Fig. 5.2. Note that the first layer is not affected by distortion, and hence, the

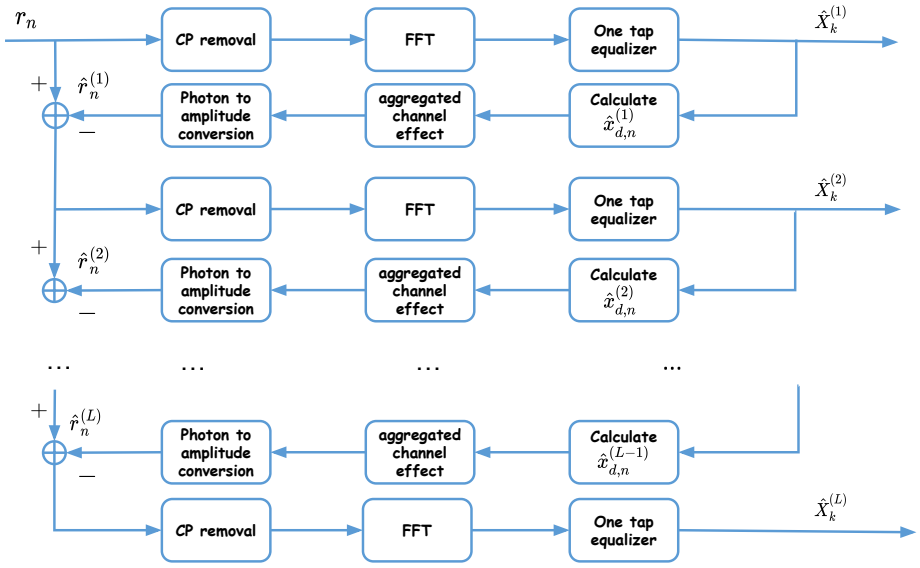

Figure 5.2 — Successive layer-based LACO-OFDM signal detection at the Rx with L layers.

corresponding symbols, $\hat{X}_k^{(1)}$, can be detected directly, as in ACO-OFDM, see Subsection 5.2.1. These symbols are then used in the next iteration to remove the distortion of the second layer. For signal detection in the ℓ^{th} layer, we proceed as follows (see Fig. 5.2):

- Use detected symbols in the previous layers to obtain the corresponding time-domain signals $\hat{x}_{d,n}^{(1)}, \cdots, \hat{x}_{d,n}^{(\ell-1)}$, as it is done at the Tx;
- Calculate their contribution $\hat{r}_n^{(1)}, \cdots, \hat{r}_n^{(\ell-1)}$ in the received signal;
- Subtract the resulting signals from r_n;
- Use the same steps as for the first layer on the (partially) distortion-removed signal to obtain $\hat{X}_k^{(\ell)}$.

The obtained $\hat{X}_k^{(1)}, \cdots, \hat{X}_k^{(L)}$ are then passed to a QAM demapper to retrieve the transmitted bits.

As explained, compared to ACO, LACO transmits L frames in parallel, which allows using lower-order signal constellations within layers. Hence, it potentially needs a lower SNR for signal detection to achieve a target BER, as compared with ACO-OFDM. In

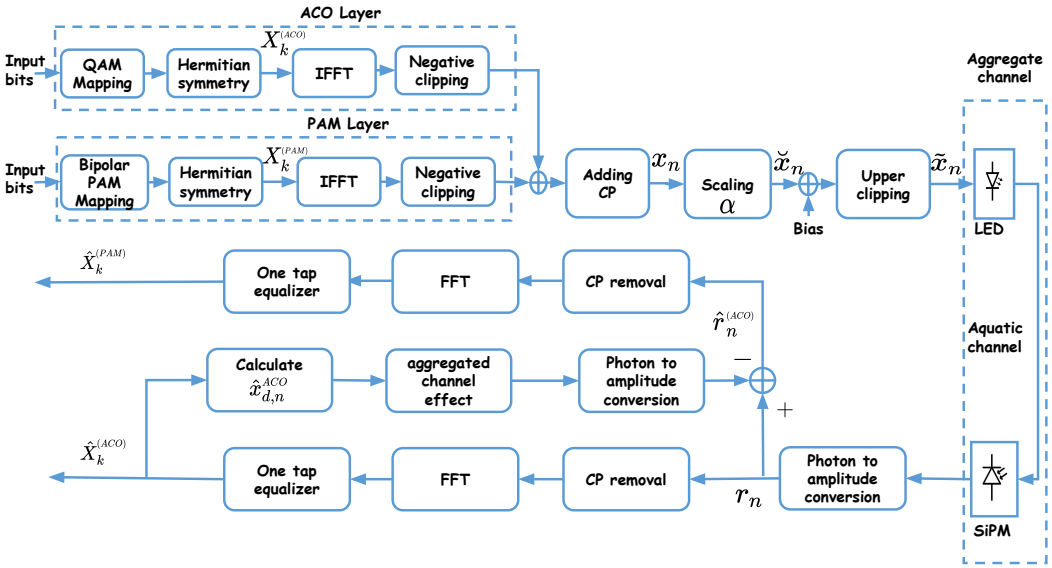

Figure 5.3 — Block diagram of the HACO-OFDM signaling scheme .

other words, LACO would have a better power efficiency, in addition to the advantage of having a lower PAPR [92, 98]. Assuming that different signal constellation sizes are used in different layers (to adjust the overall spectral efficiency), i.e., M_i-QAM signal constellation in the i^{th} layer, the spectral efficiency of LACO-OFDM is:

$$\gamma_{\text{LACO}} = \frac{N}{2(N+N_{\text{CP}})} \sum_{i=1}^{L} \frac{1}{2^i} \log_2 M_i \quad \text{(bps/Hz)}. \tag{5.2}$$

5.2.3 HACO-OFDM

Hybrid ACO-OFDM uses only two layers during signal modulation; the first layer is ACO-OFDM occupying the odd subcarriers (exactly like in the first layer of LACO) [95]. While in the second layer, PAM-DMT is used on the remaining even subcarriers, as illustrated in Fig. 5.3.

As mentioned previously in Section 4.1, the PAM-DMT signal is generated by mapping the real PAM symbols into the imaginary part and then feeding them into the IFFT block. The anti-symmetry property is thus respected, and the signal can be clipped without any loss of information since the distortion generated from negative clipping falls on the real part of the PAM signal [30, 91]. Hermitian symmetry before IFFT is also

imposed here, and the frequency domain symbols are set as follows :

$$\big[0,\, 0,\, iC_1,\, 0,\, iC_2,\, 0, ..., C_{N/4-1}, 0,\, 0,\, -iC_{N/4-1},\, 0, ..., -iC_1\,, 0\big].$$

where $i^2 = -1$, and for $q = 1, 2, ..., \frac{N}{4} - 1$ C_q are the symbols of the PAM constellation. The two resulting ACO-OFDM and PAM-DMT signals are superimposed after negative clipping. Then the time domain signal is fed to the LED after adding CP, scaled by α signal, added the DC bias, and upper clipped, as represented in Fig. 5.3. Note that, the distortion in the frequency domain resulting from the negative clipping of the first layer (i.e., ACO) will affect only the even subcarriers (as explained in the case LACO signaling), resulting in a deterioration ofthe PAM-DMT layer performance.

At the receiver side, first the ACO symbols $\hat{X}_k^{(\mathrm{ACO})}$ are detected. Their interference on the PAM-DMT signal is then removed as follows: the detected ACO symbols $\hat{X}_k^{(\mathrm{ACO})}$ are used to estimate the corresponding time signal $\hat{x}_{d,n}^{(\mathrm{ACO})}$, using which its contribution $\hat{r}_n^{(\mathrm{ACO})}$ in the received signal r_n is calculated. Next, $\hat{r}_n^{(\mathrm{ACO})}$ is subtracted from r_n to estimate the PAM symbols. Finally, $\hat{X}_k^{(\mathrm{ACO})}$ and $\hat{X}_k^{(\mathrm{PAM})}$ are passed to QAM and PAM demappers, respectively.

Since all subcarriers are used in the HACO scheme, it can achieve the same spectral efficiency as DCO with the same constellation order. However, as PAM real-valued symbols are used to modulate the imaginary part of each subcarrier, they need higher intensity levels compared to QAM to insure the same error probability, which could degrade the overall energy efficiency of HACO. However, as HACO requires a lower DC bias than DCO, it is a more energy efficient scheme. Furthermore, HACO's PAPR is lower than these of ACO and PAM-DMT [91] because it allows the use of a lower order signal constellation to achieve the same spectral efficiency. Assuming the modulation orders M_{ACO}-QAM and M_{PAM}-PAM corresponding to the ACO and PAM layers, respectively, the spectral efficiency of the HACO-OFDM scheme is :

$$\gamma_{\mathrm{HACO}} = \frac{N-2}{4(N+N_{\mathrm{CP}})}\,[\log_2(M_{\mathrm{ACO}}) + \log_2(M_{\mathrm{PAM}})] \quad (\mathrm{bps/Hz}). \tag{5.3}$$

5.2.4 ADO-OFDM

ADO-OFDM uses two layers for signal modulation similar to HACO, but it uses one ACO layer and one DCO layer. As shown in Fig. 5.4, the time domain signal of ACO and DCO layers are generated separately, while DCO is done on the even subcarriers. A DC bias is to the DCO signal before combining with ACO signal. It is important to

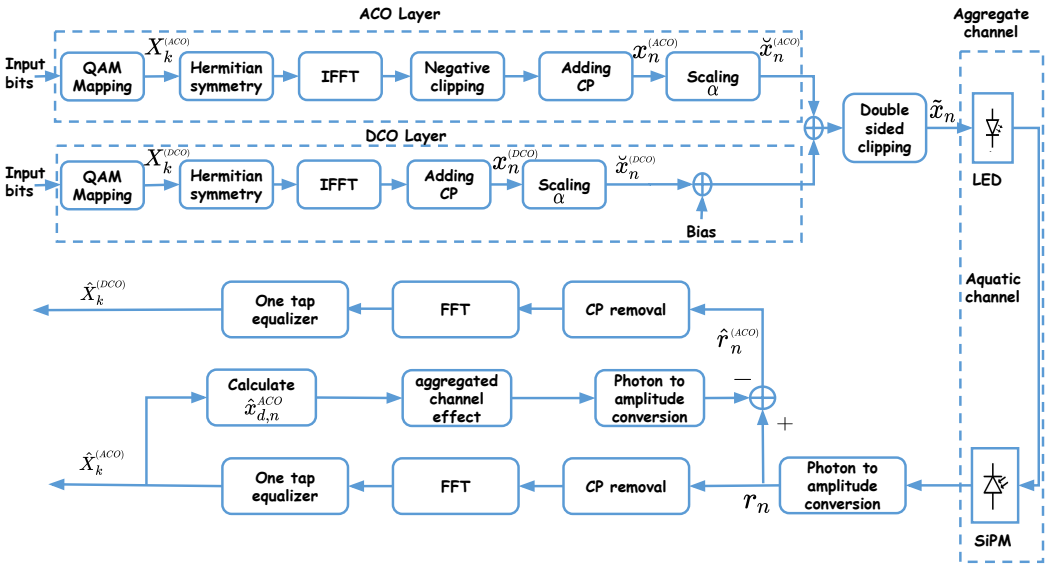

Figure 5.4 — Block diagram of the ADO-OFDM signaling scheme .

note that the ACO layer time domain signal does not need a DC bias as a bias is already added to the second (DCO) layer, see Figure 5.4. This does not change the detection process at the Rx since the DC component corresponds to the first subcarrier after FFT, which is set to zero.

As shown in Fig. 5.4 the Rx side, the ACO-OFDM symbols $X_k^{(\mathrm{ACO})}$ are estimated first. Then their contribution is removed from r_n before detecting the DCO symbols $X_k^{(\mathrm{DCO})}$.

Assuming that the modulation orders M_{ACO}-QAM and M_{DCO}-QAM for ACO and DCO layers, respectively, the spectral efficiency of the ADO-OFDM scheme is given by :

$$\gamma_{\mathrm{ADO}} = \frac{N-2}{4(N+N_{\mathrm{CP}})}\left[\log_2(M_{\mathrm{ACO}}) + \log_2(M_{\mathrm{DCO}})\right] \quad (\mathrm{bps/Hz}). \tag{5.4}$$

5.2.5 Computational Complexity

From a practical implementation point of view, an important point is the computational complexity of the Tx and the Rx for a given signaling scheme. At the Tx side, DCO and ACO use an N-point IFFT with the computational complexity of $\mathcal{O}(N\log_2(N))$. As a

result, the computational complexity of HACO and ADO is $\mathcal{O}(2N\log_2(N))$ as they use two layers. For LACO, since an N-point IFFT is used for each layer, the computational complexity is on the order of $\mathcal{O}(LN\log_2(N))$. However, as for $\ell > 1$, most of the corresponding symbols are equal to zero, the computational complexity per layer can be reduced by preforming an $N/2^{\ell-1}$-point IFFT for the ℓ^{th} layer. Then, the overall effective computational complexity can be written as $(2-\frac{1}{2^{L-1}})\mathcal{O}(N\log_2(N)))$ [92,98].

At the Rx side, DCO and ACO both need an N-point FFT with the computational complexity of $\mathcal{O}(N\log_2(N))$. For LACO, an N-point FFT is needed per each layer as well as a convolution with the aggregate CIR for $\ell > 1$. Similar to what explained above, we can perform $N/2^{\ell-1}$-point FFT for $\ell > 1$. Also, the computational complexity of the convolution is $\mathcal{O}(N_{\text{ch}}N)$, where N_{ch} stands for the approximate length of the aggregate CIR. Overall, the computational complexity of the Rx will be $(5-\frac{1}{2^{L-3}})\mathcal{O}(N\log_2(N)))+(L-1)\mathcal{O}(N_{\text{ch}}N)$ [92]. Lastly, for HACO and ADO, the Rx computational complexity is $3\mathcal{O}(N\log_2(N)))+\mathcal{O}(N_{\text{ch}}N)$.

5.2.6 Adapting signal to DR of the LED

It is obvious that the signal intensity needs to be fit to the I-V LED characteristics. For a given scaling factor α, the ADO bias is calculated based on a fixed clipping factor, as described in Section 4.3 for the case of DCO-OFDM. As for HACO, LACO and ACO, the DC bias is set to $V_{\min}$.

Different criteria can be considered for fixing the scaling factor α [99,100]. For ADO, HACO and LACO, a different α can be used for each layer. Unless otherwise specified, here, it is fixed so as to obtain the same transmit electrical power, $P_{\text{Tx,e}}$, for the different considered OFDM schemes in order to make a fair comparison between them. This choice of fixing $P_{\text{Tx,e}}$ is justified by the fact that it determines the power consumption of the Tx, which is an essential factor for mobile units (we will further relax this condition and discuss the obtained results in Section 5.3). Note that for ADO, HACO and LACO, we use the same α in each layer, although in general it can be adjusted within each layer to further optimize the performance.

As explained in Section 4.3, $P_{\text{Tx,e}}$ primarily depends on the scaling factor α and the DC bias B_{DC}. Having fixed these two parameters, we calculate $P_{\text{Tx,e}}$ by averaging the power corresponding to each symbol, which is obtained from its product by the bijective current according to the linearized LED I-V characteristics (see Fig. 3.8).

5.3 Performance Study of the UWOC Link

Considering real characteristics of practical components, a set of numerical results is provided in this section to study the performance of the different O-OFDM techniques.

In the presented study, unless otherwise mentioned, to compare the performances of the different transmission schemes, the same overall link data rate, R_b, is considered. For this, the overall spectral efficiency is set to $\eta \approx 1$ bps/Hz. For DCO and ACO, the considered default signal constellations are 4-QAM and 16-QAM, respectively. On the other hand, for ADO, 4-QAM is used in both ACO and DCO layers. For HACO, 4-QAM and 4-PAM are used for ACO and PAM layers, respectively. For LACO, we use two layers with, by default, 8-QAM and 4-QAM in the first and the second layers, respectively. For the considered $\eta \approx 1$ bps/Hz, only two layers can be considered for LACO. Also no bit or power loading is considered at the Tx in order to better see the limitations of each transmission scheme.

As explained previously, for the cases of ACO, HACO, and LACO-OFDM, B_{DC} is simply set to $V_{\min}$, i.e., 2.75 V, see Fig. 3.8. For ADO- and DCO-OFDM, based on a given α, we consider the classical approach of fixing a clipping factor to set the bias (see Section 4.3). The number of sub-carriers is set to $N = 1024$ by default, which results in an effectively flat channel per sub-channel for the considered data rates. Depending on R_b, the CP length N_{CP} is set appropriately (i.e., large enough, compared to the aggregate channel delay spread) in order to avoid ISI. The BW of the aggregate channel is determined by those of the SiPM (~ 4 MHz), the LED (~ 10 MHz), and the aquatic channel. The considered parameters for the Tx, channel, and the Rx are according to Tables 3.1 and 3.2.

5.3.1 Link performance study of improved spectral efficiency schemes with the respect to DCO-OFDM

This section compares the performances of ADO, HACO, and LACO in order to investigate the most high efficient scheme with the respect to DCO.

Performance link study when $\eta \approx 1$ bps/Hz:

First, lets see the impact of DC bias setting on the performance of ADO-OFDM similar to what we presented for DCO in Section 4.4. Figure 5.5 shows the BER plots as a function of link distance. For $R_b = 20$ Mbps with $T_s = 5.165 \times 10^{-5}$ sec and $P_{\text{Tx,e}} = 50$

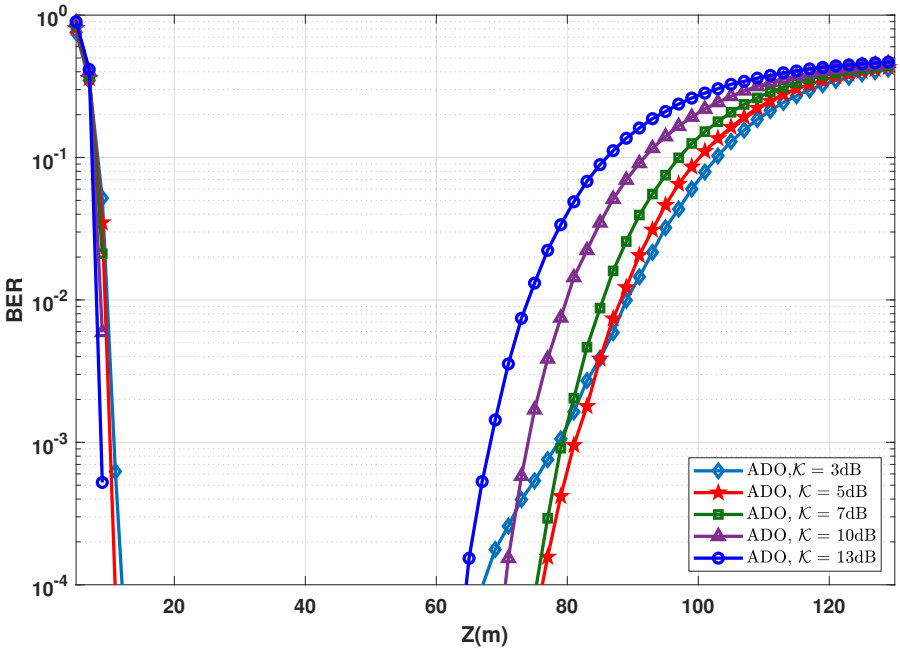

Figure 5.5 — BER performance of ADO-OFDM using classical DC bias. $P_{\mathrm{Tx,e}} = 50\,\mathrm{mW}$; $N = 1024$; $N_{\mathrm{CP}} = 9$; $R_b = 20\,\mathrm{Mbps}$. The corresponding clipping factors are $\alpha = 0.142$, 0.115, 0.0935, 0.0695, and 0.0515 for $\mathcal{K}_{\mathrm{dB}} = 3$, 5 7, 10, and 13 dB (corresponding to $B_{\mathrm{DC}} = 2.8495$, 2.8693, 2.8832, 2.8962, and 2.9085 V

mW. B_{DC} is calculated based on the considered clipping factor $\mathcal{K}_{\mathrm{dB}}$ (see Section 4.3). It can be noticed that the best performance in terms of LBI and maximum attainable distance $Z_{\max}$ is achieved with $\mathcal{K}_{\mathrm{dB}} = 5$ dB. Compared to DCO, which needs a larger clipping factor of $\mathcal{K}_{\mathrm{dB}} = 7$ dB to achieve the best link performance (see Section 4.4), ADO needs a smaller $\mathcal{K}_{\mathrm{dB}}$, as expected, as it uses an ACO signal in the first layer. However, the corresponding LBI and $Z_{\max}$ are 71.3 and 81.5 m, respectively, which are lower than those of DCO, i.e., 78.9 and 91.3 m, respectively (see Table 4.1). which signifies that DCO remains more energy efficient. In the sequel, we consider $\mathcal{K}_{\mathrm{dB}} = 5$ dB for ADO-OFDM.

Let us now compare the performance of the three considered schemes. Figure 5.6 presents BER plots as a function of the link distance Z for different R_b. The latter is fixed by setting the duration of the OFDM symbol T_s while keeping N unchanged. We can notice the advantage of LACO over ADO and HACO, with the largest attainable link span, e.g., $\sim 85\,\mathrm{m}$ for $R_b = 20\,\mathrm{Mbps}$ and a target BER of 10^{-3} (the corresponding LBI

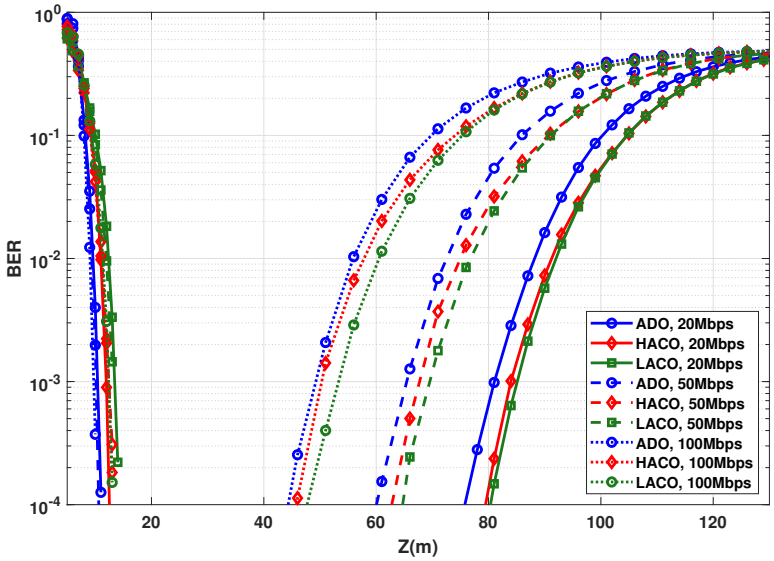

Figure 5.6 — BER performance as a function of distance for ADO-, HACO-, and LACO-OFDM. $P_{\text{Tx,e}} = 50\,\text{mW}$, $N = 1024$; $N_{\text{CP}} = 9$, 20, and 28, for $R_b = 20$, 50, and 100 Mbps, respectively, $\eta \approx 1\,\text{bps/Hz}$.

and $Z_{\max}$ are summarized in Table 5.1). We also notice a slight advantage of HACO over LACO regarding LBI for $R_b = 20$ Mbps. However, HACO loses this advantage when the data rate increases, which can be explained by using PAM modulation in the second layer. In fact, with increase in R_b, and hence decrease in symbol duration, the PAM modulation in the second layer of HACO requires more power than the QAM modulation for LACO. Note that, a better performance can be obtained for HACO by adjusting the allocated power between the two layers, i.e., using appropriate scaling factors in the two layers.

Impact of increasing QAM Constellation Size

Consider now the case of $\eta \approx 2\,\text{bps/Hz}$. We further consider the LACO scheme with 2,3 and 4 layers and compare its performance with these of ADO and HACO. For this, we consider the signal constellations presented in Table 5.2. Note that using larger constellation sizes allows increasing the data rate, while keeping the same OFDM symbol duration T_s. Nevertheless, in order to make a fair comparison with the previous case (i.e., $\eta \approx 1\,\text{bps/Hz}$), the same R_b values as before are considered, i.e., 20, 50, and 100 Mbps,

Table 5.1 — LBI and maximum attainable range for ADO, HACO, an LACO-OFDM transmission schemes according to Fig. 5.6; $P_{\mathrm{Tx,e}} = 50\,\mathrm{mW}$, BER$= 10^{-3}$, $\eta \approx 1\,\mathrm{bps/Hz}$.

	R_b (Mbps)	LBI (m)	$Z_{\max}$ (m)
ADO	20	70.6	81.1
	50	55.3	65.4
	100	39.5	49.2
HACO	20	72	84
	50	55.4	67.7
	100	38.1	50.4
LACO	20	71.6	85.1
	50	56.4	69.5
	100	40.6	53

Table 5.2 — Signal constellation in different layers of the considered LACO, ADO, and HACO-OFDM transmission schemes for $\eta \approx 2\,\mathrm{bps/Hz}$.

	1st layer	2nd layer	3rd layer	4th layer
2 layers LACO	64-QAM	16-QAM	-	-
3 layers LACO	32-QAM	16-QAM	16-QAM	-
4 layers LACO	32-QAM	16-QAM	8-QAM	4-QAM
ADO	16-QAM	16-QAM	-	-
HACO	16-QAM	16-PAM	-	-

and accordingly, T_s is multiplied by 2.

Figure 5.7 shows BER plots versus link distance for LACO-OFDM with 2, 3 and 4 layers for $P_{\mathrm{Tx,e}} = 50$ mW. First, we notice that the three-layer LACO achieves the largest attainable link span and LBI due to a lower PAPR compared with the 2-layer LACO [95]. To achieve the same $P_{\mathrm{Tx,e}}$ the 3-layer LACO uses a lower α compared to the 2-layer case, which allows to avoids significant signal clipping as it is the case the 2-layer LACO. One would expect that the 4-layer LACO provides still a better performance. However, although adding another layer (compared to 3-layer LACO) decreases further the PAPR, due to using the same α in all layers results in a performance degradation [1] In fact, as shown in [95], the 4-layer LACO has a slightly better performance than

[1]For instance, the 4-QAM modulation in the 4^{th} layer will be allocated the same power as the 32-QAM

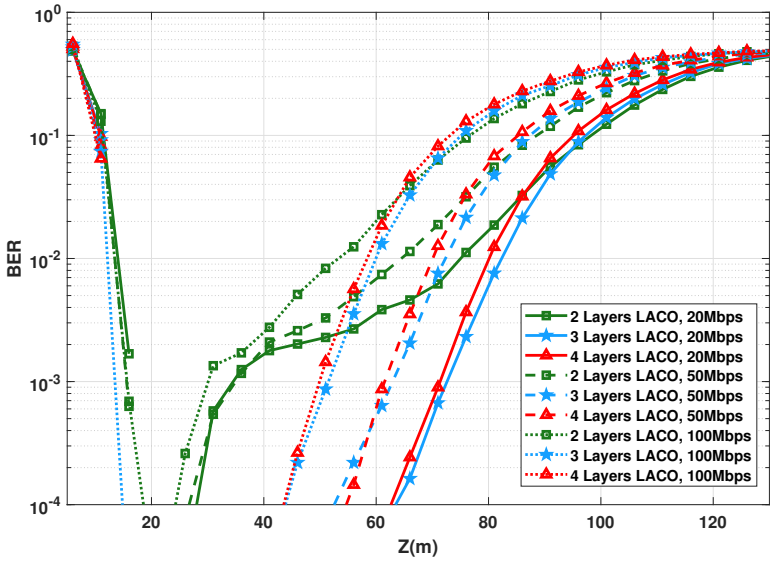

Figure 5.7 — BER performance as a function of distance for 2, 3 and 4-layers LACO-OFDM. $P_{\mathrm{Tx,e}} = 50\,\mathrm{mW}$, $N = 1024$; $\eta \approx 2$ bps/Hz; $N_{\mathrm{CP}} = 5$, 11, and 20, for $R_b = 20$, 50, and 100 Mbps, respectively.

3-layer LACO for higher spectral efficiencies ($\eta > 3.5$) but at the expense of a much higher computational complexity, as explained in Section 5.2.5.

Finally, BER performances against Z are plotted in Fig. 5.8 for ADO, HACO, and the 3-layer LACO. We notice the undeniable advantage of LACO over the other transmission schemes. The PAPR of HACO is almost the same as that of the 2-layer LACO [95], which suffers from severe signal clipping for $P_{\mathrm{Tx,e}} = 50$ mW. For ADO, the PAPR increases using a 16QAM constellation, resulting in a sever lower clipping.

In the following, based on presented results and given the advantage of LACO over ADO and HACO, we will consider LACO with 2-layers for $\eta \approx 1$ bps/Hz and with 3-layers for $\eta \approx 2$ bps/Hz.

5.3.2 Clipping Effect on the Link Performance

Let us now study the impact of signal clipping on the performance of O-OFDM schemes The considered signal constellations 4-QAM and 16-QAM for DCO and ACO, respec-

modulation at the 1st layer, which is, of course, not optimal.

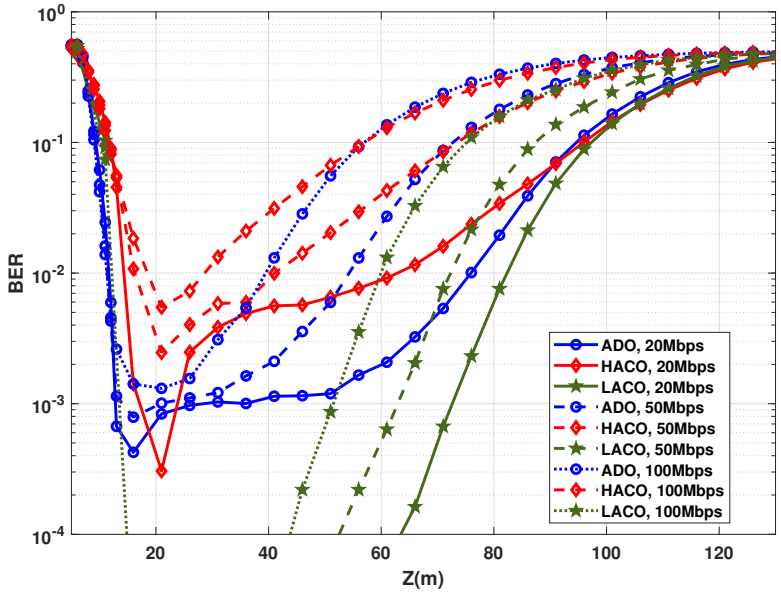

Figure 5.8 — BER performance as a function of distance for ADO, HACO and 3-layer LACO-OFDM. $P_{\mathrm{Tx,e}} = 50\,\mathrm{mW}$, $N = 1024$; $\eta \approx 2$ bps/Hz; $N_{\mathrm{CP}} = 5$, 11, and 20, for $R_b = 20$, 50, and 100 Mbps, respectively.

tively. For LACO, ADO, and ADO we will use the same configuration as in Section 5.3.1, which results in the same spectral efficiency of $\eta \approx 1$ bps/Hz. Figure 5.9 contrasts the BER performances of these schemes as a function of $P_{\mathrm{Tx,e}}$. The link data rate is fixed to 20 Mbps and the link distance is fixed to $Z = 20$ and 70 m, corresponding to relatively moderate and high channel attenuation, respectively.

From Fig. 5.9, for relatively low transmit powers, i.e., $P_{\mathrm{Tx,e}} \lesssim 25\,\mathrm{mW}$, notice the close performances of the five techniques, in particular for the relatively short range of $Z = 20\,\mathrm{m}$. For $Z = 70\,\mathrm{m}$, ACO and LACO outperform DCO and HACO, with a slight advantage for ACO; For instance, at a target BER of 10^{-3}, the required $P_{\mathrm{Tx,e}}$ is around 9.7, 13.2, 15.4, and 19.4 mW for ACO, LACO, HACO, and DCO schemes, respectively. As for ADO, the considered distance is too high and cannot achieve a low BER even when increasing transmit electrical power.

Meanwhile, the performances of these schemes are affected differently for relatively large transmit powers. For instance, for $Z = 20\,\mathrm{m}$, upper signal clipping limits the link performance for $P_{\mathrm{Tx,e}}$ larger that about 90.4, 125.6, 174.8, 230.6 and 310 mW for ACO,

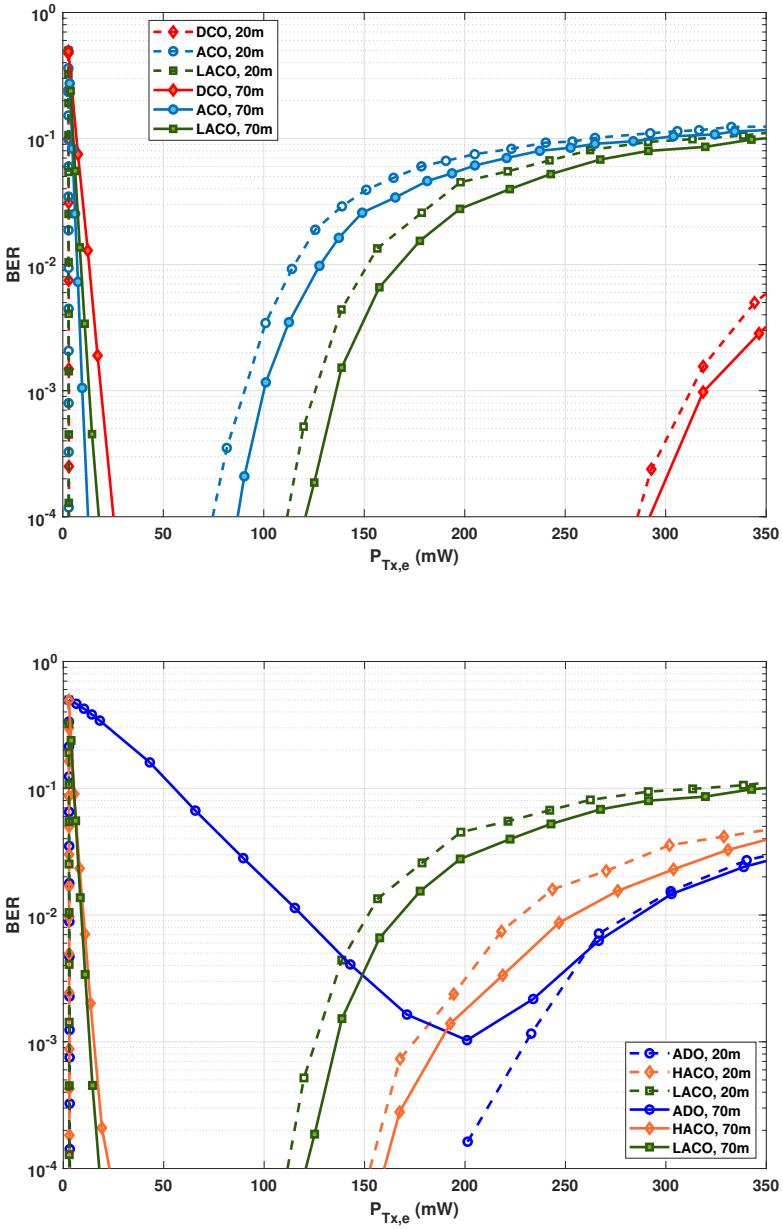

Figure 5.9 — Contrasting clipping effect on DCO-, ACO-, LACO-, ADO-, and HACO-OFDM BER performances for $Z = 20$ and 70 m. $R_b = 20$ Mbps, $N = 1024$, $N_{\mathrm{CP}} = 9$.

LACO, HACO, ADO, and DCO cases, respectively. The advantage of DCO can be explained by the smaller modulation size used, which results in a lower signal PAPR, and hence, a less detrimental effect of the clipping noise. For LACO and HACO, which has a lower PAPR than ACO, the clipping effect appears for a smaller $P_{\text{Tx,e}}$; yet, we again notice a neat advantage of DCO.

Notice that, as explained previously, here a non-zero bias is considered for ACO, HACO, and LACO due to the LED characteristics. The presented results show how these schemes are compared in practice. In particular, for relatively low $P_{\text{Tx,e}}$, there is evidence of higher energy efficiency of ACO, LACO, and HACO over DCO and ADO; these latter suffers from the higher DC-bias used. Meanwhile, since DCO has the lowest PAPR [95, 101], it is more robust than the other considered schemes with respect to increasing the transmit power. Note that, in addition to having a lower PAPR, DCO uses a smaller α. For instance, for $P_{\text{Tx,e}} = 25\,\text{mW}$, α is set to 0.0455, 0.056, 0.153, 0.079 and 0.092, for DCO, ADO, ACO, HACO, and LACO-OFDM schemes, respectively.

It is worth focusing on the difference between the upper limits of $P_{\text{Tx,e}}$ for $Z = 20$ and 70 m in Fig. 5.9. One would expect the same limit irrespective of Z, since clipping affects the signal at the Tx side. However, the SiPM saturation at the Rx also affects the link performance for relatively high $P_{\text{Tx,e}}$. Consequently, we notice a lower limit for $P_{\text{Tx,e}}$ for a smaller Z, where the Rx saturation becomes increasingly important.

In order to better contrast the performances of the five signaling schemes, while taking into account the effects of signal clipping, channel attenuation, and Rx saturation, we have presented color maps of BER versus $P_{\text{Tx,e}}$ and Z in Fig. 5.10 and 5.11 for $R_b = 20$, 50, and 100 Mbps.[2] Considering a target BER of 10^{-3}, we notice a larger link span for ACO and LACO, compared with DCO for relatively small transmit powers, whereas DCO-OFDM offers the largest LBI. On the other hand, for relatively large $P_{\text{Tx,e}}$, as already noticed in Fig. 5.9, DCO undeniably shows more robustness due to having a lower PAPR and a lower sensitivity to Rx saturation, and in this sense, can be considered as to be a more flexible transmission scheme. As for ADO, we notice that it has the smallest LBI and the lowest $Z_{\max}$ among all considered schemes. LACO and HACO provides a larger LBI, as compared with ACO, and more flexibility of setting the transmit power. In fact, ACO, LACO, and HACO use a low DC bias and are penalized by their higher PAPR for high transmit powers. DCO, on the other hand, uses a larger

[2]For the sake of completeness and following the computational complexity analysis presented in Section 5.2.5, for the considered LED and SiPM models, N_{ch} approximately equals 5, 10, et 20 for data rates of 20, 50, and 100 Mbps and the spectral efficiency of $\eta \approx 1$ bps/Hz.

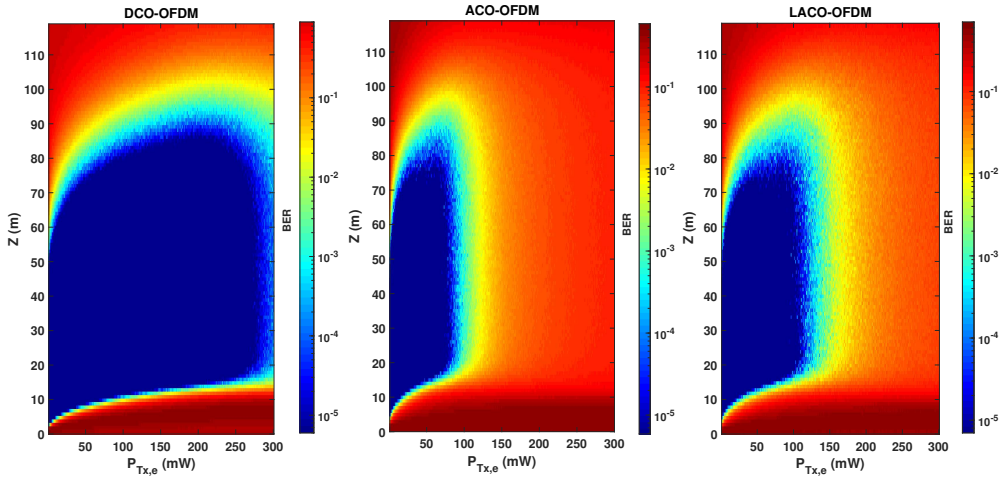

(a) $R_b = 20$ Mbps

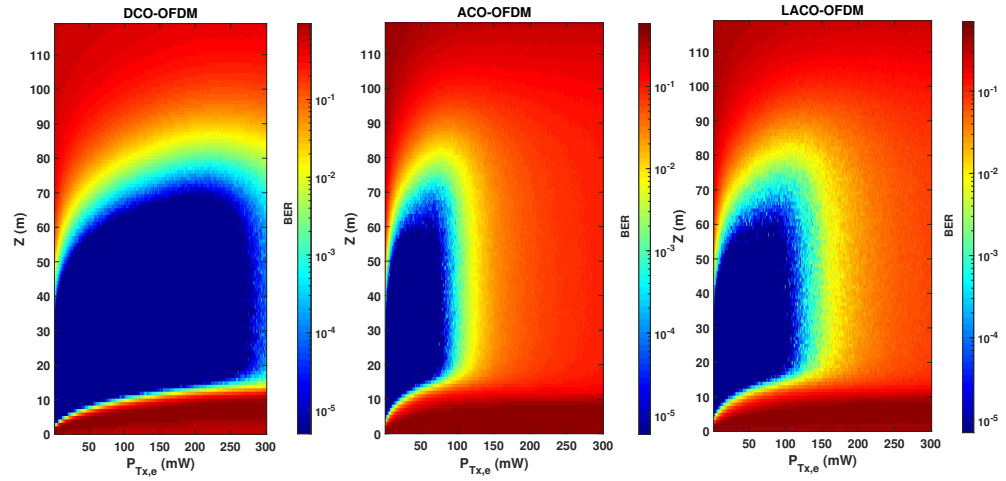

(b) $R_b = 50$ Mbps

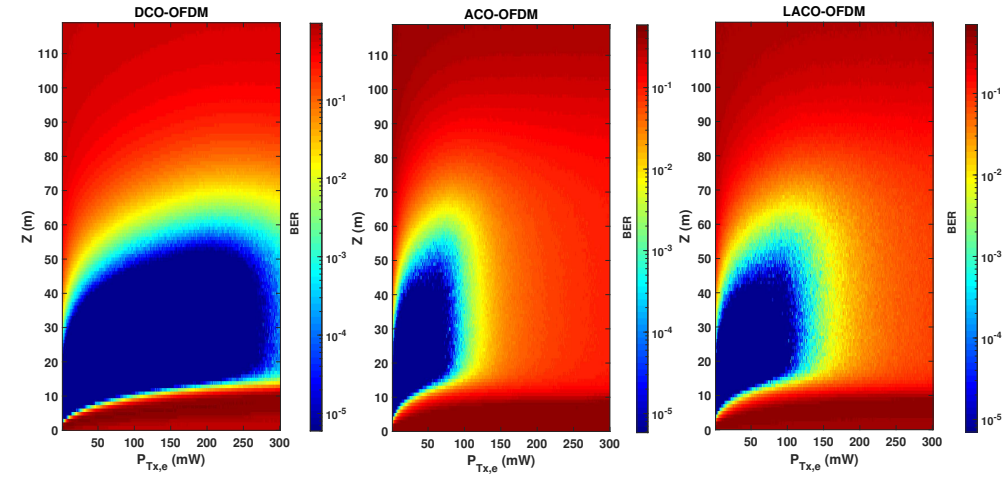

(c) $R_b = 100$ Mbps

Figure 5.10 — Comparison of BER performance versus the link range Z and the transmit electrical power $P_{\mathrm{Tx,e}}$ of DCO-, ACO-, and LACO-OFDM taking into account the LED DR and signal clipping. $N = 1024$, $N_{\mathrm{CP}} = 9$, 20, and 28, for data rates of (a) 20, (b) 50, and (c) 100 Mbps, $\eta \approx 1$ bps/Hz.

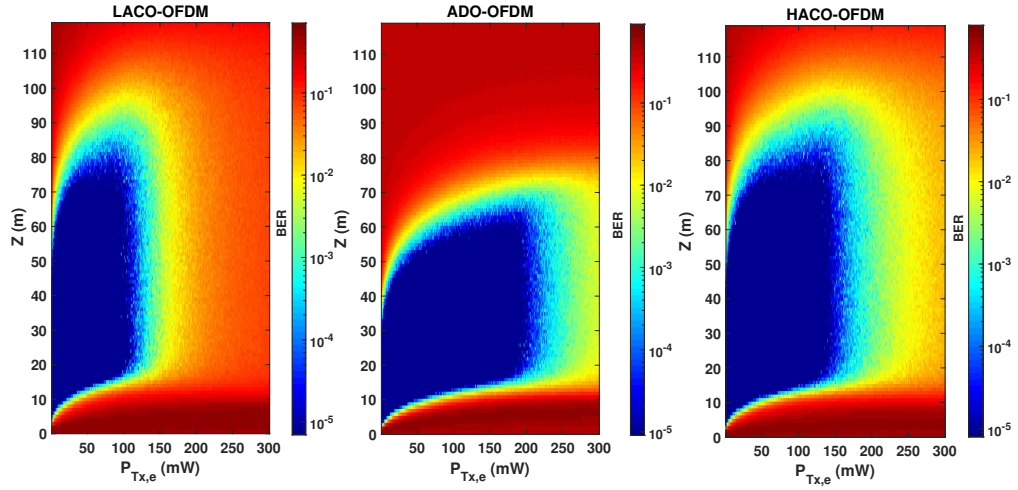

(a) $R_b = 20$ Mbps

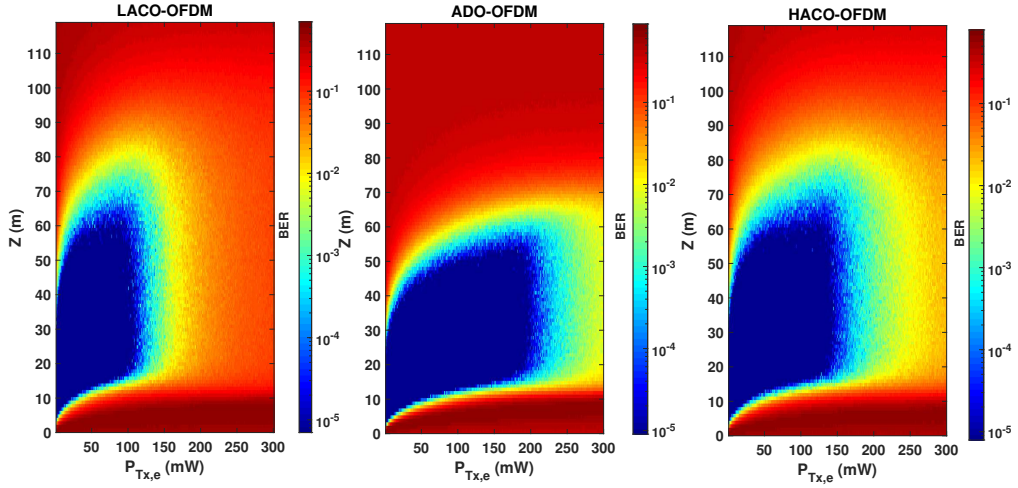

(b) $R_b = 50$ Mbps

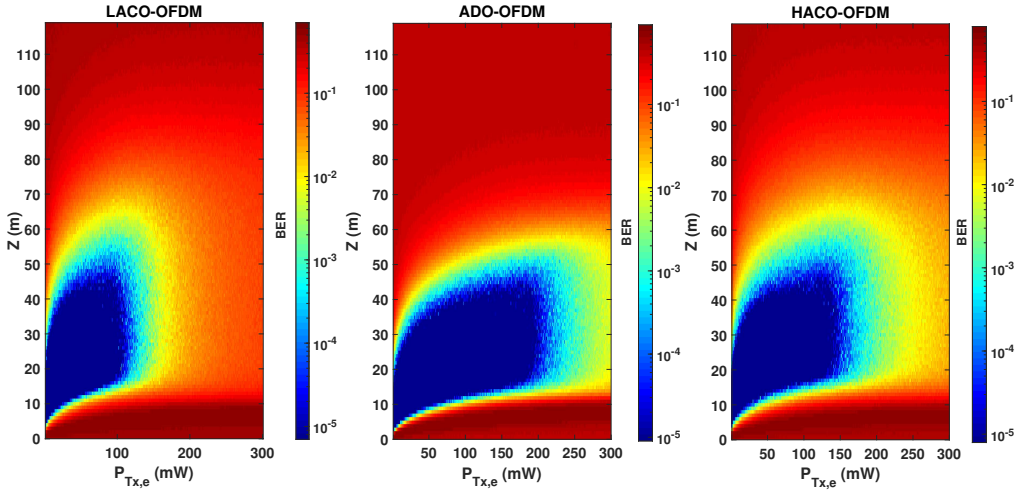

(c) $R_b = 100$ Mbps

Figure 5.11 — Comparison of BER performance versus the link range Z and the transmit electrical power $P_{\mathrm{Tx,e}}$ of LACO-, ADO-, and HACO-OFDM taking into account the LED DR and signal clipping. $N = 1024$, $N_{\mathrm{CP}} = 9$, 20, and 28, for data rates of (a) 20, (b) 50, and (c) 100 Mbps, $\eta \approx 1$ bps/Hz.

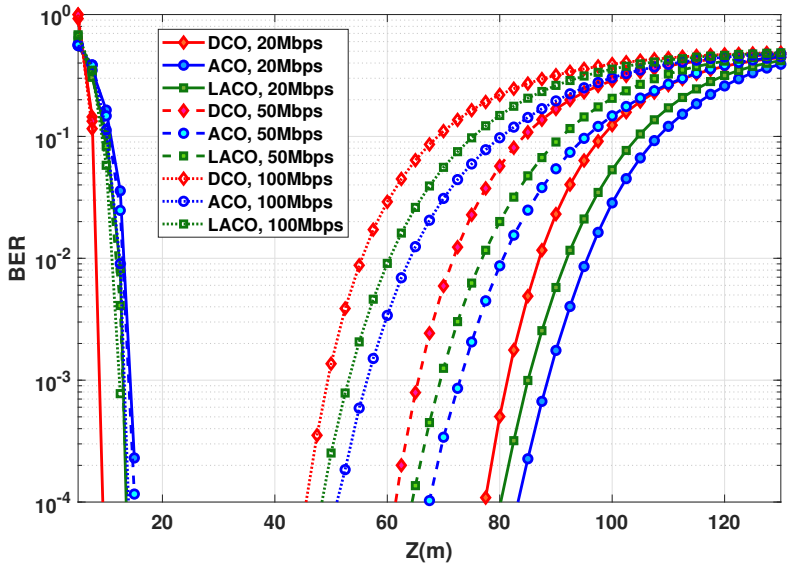

Figure 5.12 — BER performance as a function of distance for DCO-, ACO-, and LACO-OFDM. $P_{\text{Tx,e}} = 50\,\text{mW}$, $N = 1024$; $N_{\text{CP}} = 9$, 20, and 28, for $R_b = 20$, 50, and 100 Mbps, respectively, $\eta \approx 1 bps/Hz$.

DC bias and a smaller scaling factor for a given $P_{\text{Tx,e}}$. As a result, the clipping noise limits its performance for much higher transmit powers.

5.3.3 Impact of Data Rate and Transmit Power

Consider the BER performance as a function of link distance Z for DCO-, ACO- and LACO for different R_b. From Fig. 5.10, to have a sufficiently large LBI for all schemes and the considered bit rates, $P_{\text{Tx,e}}$ is set to 50 mW. BER plots are presented in Fig. 5.12, where we notice the best performance for ACO with the largest attainable link span, e.g., around 89 m for $R_b = 20$ Mbps and a BER of 10^{-3} (the corresponding LBI and $Z_{\max}$ are summarized in Table 5.3). So, ACO is the most power-efficient scheme. This confirms the results previously presented in Fig. 5.9 showing that ACO needs a lower $P_{\text{Tx,e}}$ to get a target BER, compared to DCO and LACO. We further notice that, for all schemes, LBI shrinks when increasing the data rate, which is due to the decrease in T_s, i.e., a shorter duration for collecting photons, see equation (3.8).

Table 5.3 — LBI and maximum attainable range for DCO, ACO, an LACO-OFDM transmission schemes according to Fig. 5.12; $P_{\mathrm{Tx,e}} = 50\,\mathrm{mW}$, BER$= 10^{-3}$, $\eta \approx 1\,\mathrm{bps/Hz}$.

	R_b (Mbps)	LBI (m)	$Z_{\max}$ (m)
DCO	20	72.5	81.4
	50	56.5	65.4
	100	40.5	49.3
ACO	20	73.8	88.6
	50	58.6	73
	100	42.8	56.3
LACO	20	71.6	85.1
	50	56.4	69.5
	100	40.6	53

5.3.4 Relaxing the Transmit Power Constraint

So far, our study was mainly based on the assumption of constrained transmit power, considering the Tx energy efficiency as the main criterion. Consider now as objective the maximization of the LBI in order to obtain the most flexible link operation, while relaxing the requirement of energy efficiency. Accordingly, considering a data rate of 20 Mbps and based on the results of Fig. 5.10, we set $P_{\mathrm{Tx,e}}$ to 50, 80, 140, 185 and 185 mW for ACO, LACO, HACO, ADO, and DCO, respectively, which allow to maximize the LBI for each scheme. The BER performances are contrasted in Fig. 5.13, where it is seen that DCO provides the best performance, as it could be expected. The corresponding LBIs and $Z_{\max}$ are summarized in Table 5.4 for a target BER of 10^{-3}.

In the sequel, we again fix $P_{\mathrm{Tx,e}}$, considering as the main criterion the link energy efficiency.

5.3.5 Impact of QAM Constellation Size

Up to now, the spectral efficiency of $\sim 1\,\mathrm{bps/Hz}$ was mostly considered, corresponding to the signal constellations of 4-QAM for DCO, 16-QAM for ACO, and 8-QAM and 4-QAM for layers 1 and 2 for LACO. Let us now consider larger signal constellations to see how these schemes are affected by a consequently increased PAPR. Accordingly, the constellation is set to 16-QAM for DCO and 256-QAM for ACO, resulting in a spectral

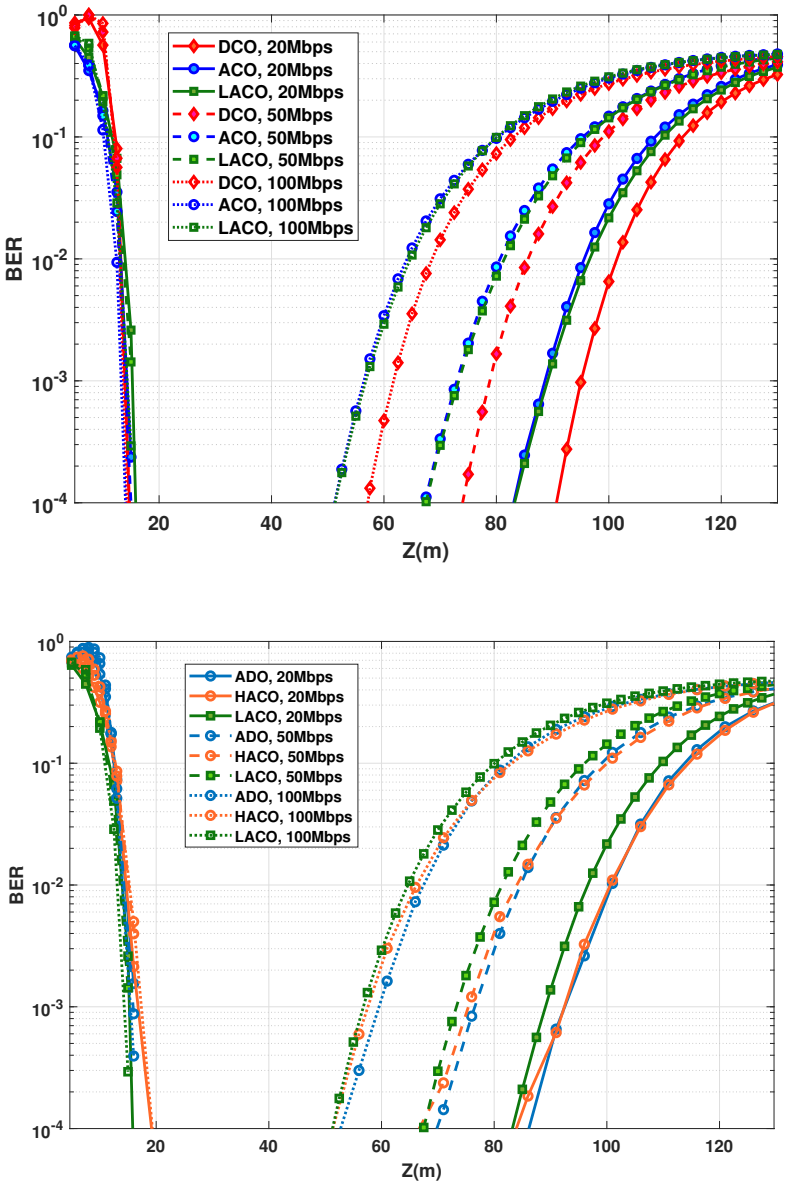

Figure 5.13 — BER as a function of Z for ACO-, LACO-, HACO-, ADO- and DCO-OFDM, with $P_{\mathrm{Tx,e}} = 50$, 80, 140, 185 and 185 mW, respectively. $R_b = 20$, 50, and 100 Mbps; N and N_{CP} as in Fig. 5.12 and 5.6, $\eta \approx 1$ bps/Hz.

Table 5.4 — LBI and maximum attainable range for DCO, ACO, LACO, ADO, and HACO-OFDM transmission schemes according to Fig. 5.13; BER = 10^{-3}, $\eta \approx$ 1 bps/Hz.

	R_b (Mbps)	LBI (m)	$Z_{\max}$ (m)
DCO	20	81	95
	50	64.9	78.9
	100	48	61.8
ACO	20	73.8	88.6
	50	58.6	73
	100	42.8	56.3
LACO	20	74.3	88.8
	50	58.9	73.2
	100	43.1	56.5
ADO	20	77.1	92.5
	50	60.7	76.2
	100	44.2	59.6
HACO	20	75.7	92.5
	50	58.3	75.4
	100	40.4	57.7

efficiency of ~ 2 bps/Hz. For LACO, we use three layers with the constellation sizes specified in Table 5.2. The choice of three layers for LACO permits the best performance for the considered spectral efficiency, as explained in Section 5.3.1.

The BER performances versus Z are compared in Fig. 5.14 for $P_{\text{Tx,e}} = 20$ and 50 mW. First, notice from Fig. 5.14(a) that (as it was the case in Fig. 5.12) for relatively short Z where the performance is limited by SiPM saturation, we have a shorter saturation range for DCO. This is due to the high PAPR of ACO and LACO because of using a larger signal constellation. Interestingly, LACO offers the best performance in terms of LBI and the maximum attainable distance for both considered $P_{\text{Tx,e}}$.

For $P_{\text{Tx,e}} = 50$ mW, from Fig. 5.14(b), notice that LACO and DCO have the same LBI. Also, given the large constellation sizes used for ACO, this transmit power appears to be too high, resulting in considerable signal clipping and, consequently, a poor performance. For LACO, using more layers allows reducing the constellation size in the first layer, (see Table 5.2, for instance, the case of 2-layer LACO is considered in [102] where

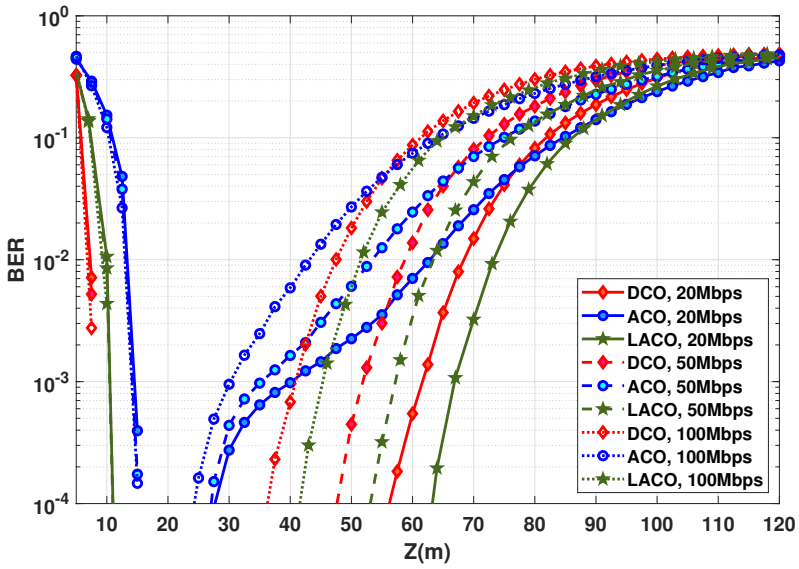

(a) $P_{\mathrm{Tx,e}} = 20\,\mathrm{mW}$

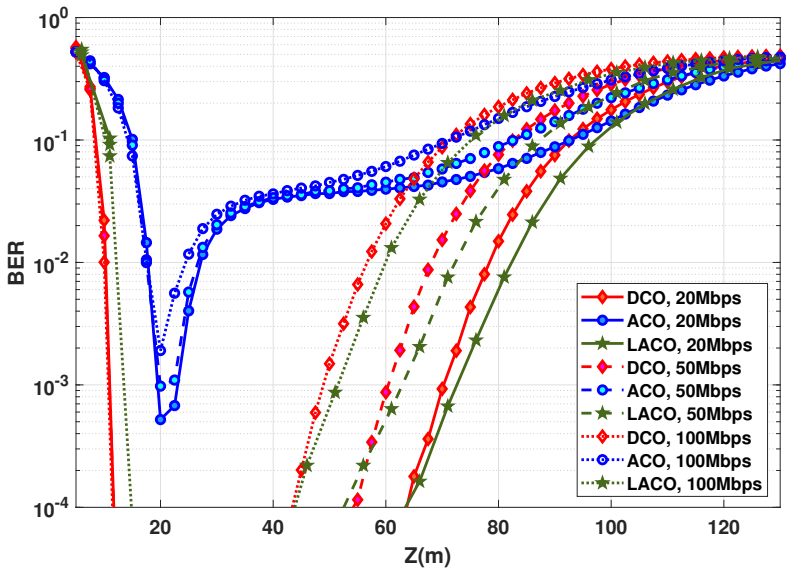

(b) $P_{\mathrm{Tx,e}} = 50\,\mathrm{mW}$

Figure 5.14 — BER performance as a function of distance for DCO, ACO and LACO-OFDM. Spectral efficiency of $\sim 2\,\mathrm{bps/Hz}$ using, e.g., 16QAM for DCO. $N = 1024$, $N_{\mathrm{CP}} = 5$, 11, and 20, for $R_b = 20$, 50, and 100 Mbps, respectively. Electrical transmit power of (a) 20 mW and (b) 50 mW.

Table 5.5 — LBI and maximum attainable range for DCO, ACO, and LACO-OFDM according to Fig. 5.14; BER $= 10^{-3}$, $\eta \approx 2$ bps/Hz.

		$P_{\text{Tx,e}} = 20\,\text{mW}$		$P_{\text{Tx,e}} = 50\,\text{mW}$	
	R_b (Mbps)	LBI (m)	$Z_{\max}$ (m)	LBI (m)	$Z_{\max}$ (m)
DCO	20	53.2	61.6	59.1	70.1
	50	43.6	51.9	49.5	60.3
	100	33.5	40.9	38	48.9
ACO	20	25.5	40.1	3.4	23.1
	50	20.8	35.2	–	–
	100	16.1	30.2	–	–
LACO	20	56.3	66.9	59.1	72.6
	50	46.7	57.3	49.5	63
	100	34.8	45.4	38.2	51.7

a rather poor performance is obtained). However, the advantage obtained by LACO comes at the expense of a higher computational complexity and more latency at the Rx due to processing multiple layers (see Section 5.2.5). From a practical point of view, it would be more interesting to use DCO rather than LACO, especially since the distance can be increased using multiple LEDs, as it will be explained in the next section. To better understand this limitation in the transmit power regarding the Rx performance, we have presented in Fig. 5.15 color maps of BER versus Z and $P_{\text{Tx,e}}$ for $R_b = 20$, 50, and 100 Mbps, where we can notice the significant reduction of the LBI, in particular, for ACO and LACO, as compared with Fig.5.10.

Table 5.5 summarizes the LBI and $Z_{\max}$ for different data-rates and the target BER of 10^{-3} for the three schemes.

5.3.6 Increasing Link Span Using Multiple LEDs

Since the limited LED DR constrains the transmit power, a rational solution for increasing the link span is to use multiple LEDs by putting them into an array, thus increasing the effective transmit optical power [32, 60]. Consider 100 LEDs at the Tx, modulated simultaneously, and set the transmit power per LED to $P_{\text{Tx,e}} = 50\,\text{mW}$ (this way, the total transmit electrical power is 5 W). We assume that we have almost the same radiation pattern (i.e., Lambertian with $m \approx 45$) as for a single LED. Figure 5.16 shows the BER plots for the three considered data rates and for spectral efficiencies of $\eta \approx 1$ bps/Hz (i.e.,

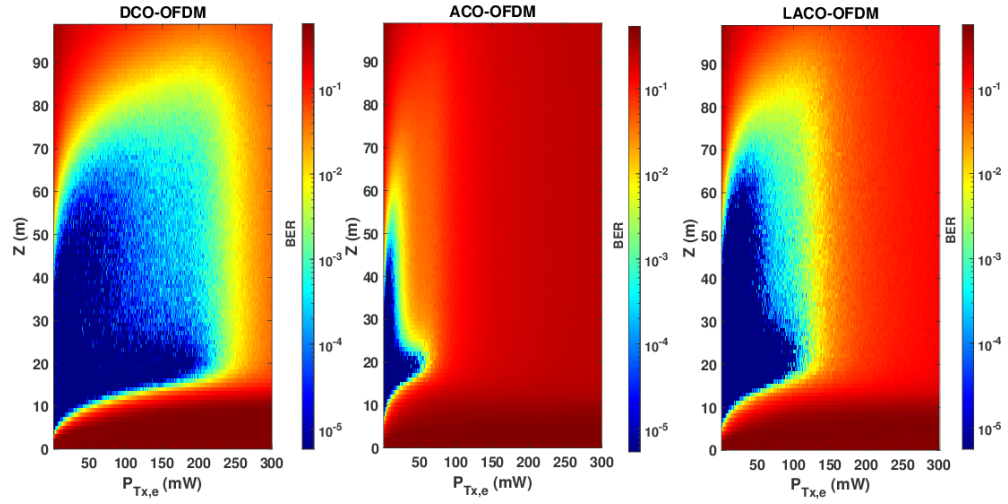

(a) $R_b = 20$ Mbps

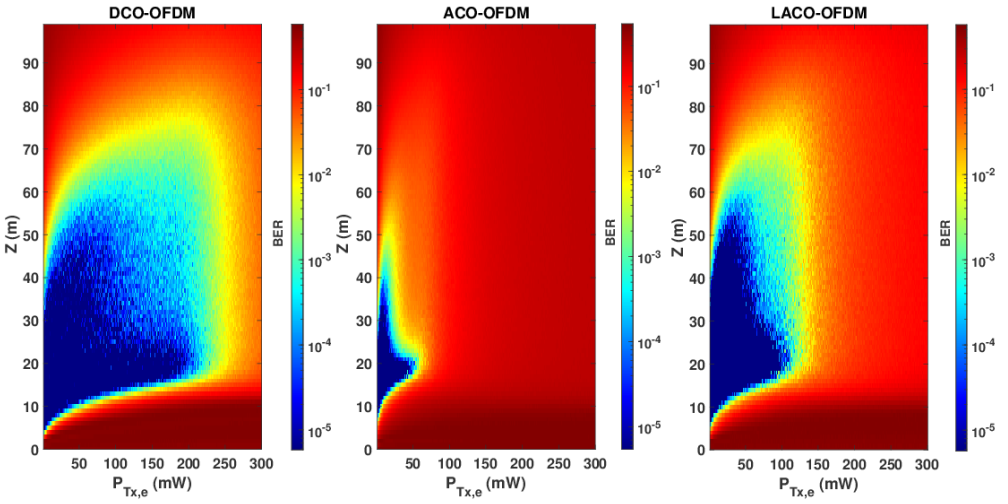

(b) $R_b = 50$ Mbps

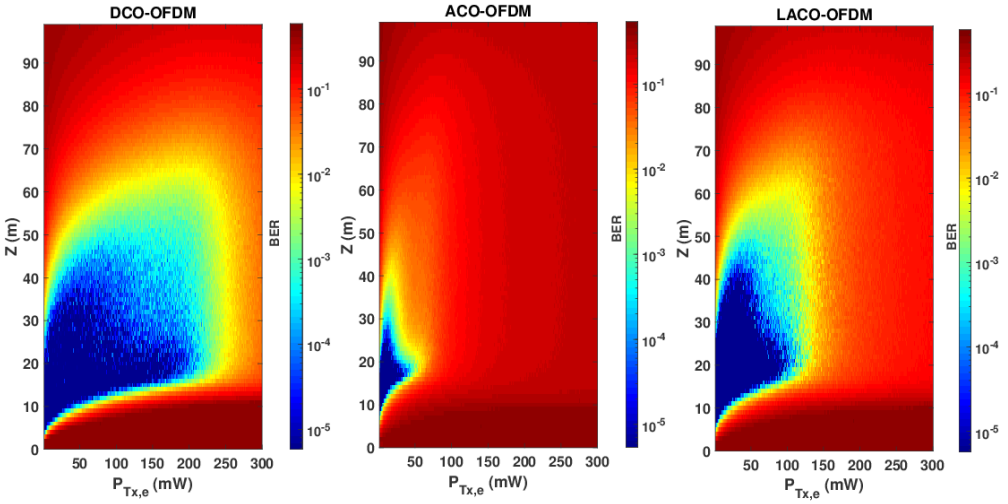

(c) $R_b = 100$ Mbps

Figure 5.15 — Comparison of BER versus the link range Z and the transmit electrical power $P_{\mathrm{Tx,e}}$ of the three transmission schemes. $N = 1024$, $N_{\mathrm{CP}} = 5$, 11, and 20, for data rates of (a) 20, (b) 50, and (c) 100 Mbps, $\eta \approx 2$ bps/Hz.

Table 5.6 — LBI and maximum attainable range for DCO, ACO, an LACO-OFDM transmission schemes according to Fig. 5.16; BER $= 10^{-3}$.

		$\eta \approx 1$ bps/Hz		$\eta \approx 2$ bps/Hz	
	R_b (Mbps)	LBI (m)	$Z_{\max}$ (m)	LBI (m)	$Z_{\max}$ (m)
DCO	20	93.7	127.5	77.5	115.5
	50	76.5	110.1	66.5	104.3
	100	58.5	91.6	53.3	90.9
ACO	20	91.2	135.4	6.3	57.9
	50	74.5	118.4	2.88	55.5
	100	57.3	99.9	–	–
LACO	20	89.32	131.8	74.8	118.3
	50	73.2	114.5	63.6	107.1
	100	55.6	95.9	50.4	94

with 4-QAM for DCO-OFDM) and $\eta \approx 2$ bps/Hz (i.e., with 16-QAM for DCO-OFDM). The LBI and $Z_{\max}$ corresponding to a target BER of 10^{-3} are summarized in Table 5.6, which are larger than those for the case of a single LED (compare with Tables 5.3 and 5.5). Nevertheless, the minimum operational distance (before SiPM saturation) is also increased, as expected [32]. For instance, for $R_b = 20$ Mbps with $\eta \approx 1$ bps/Hz, the LBI is about 93.7, 91.2, and 89.3 m for DCO, ACO, and LACO schemes, respectively. For $\eta \approx 2$ bps/Hz, we notice the undeniable advantage of DCO in terms of LBI. However, the maximum attainable distance is achieved by LACO as expected.

In practice, if the channel parameters (including the link range) are known at the Tx, the number of actually activated LEDs can be adjusted so as to allow working within the LBI adaptively, and hence, to optimize the link performance.

5.4 Conclusion

For the case of an SiPM-based UWOC system and in order to increase the link data rate, this chapter investigated the use of high spectral efficiency modulation schemes based on O-OFDM, namely the five schemes of DCO-, ACO-, LACO-, HACO-, and ADO-OFDM. We discussed the limitations in terms of the SiPM-based Rx saturation and the limited Tx DR, which determine the range of operation of the UWOC link for a given target BER. Indeed, the novelty of our study is that we take into account the

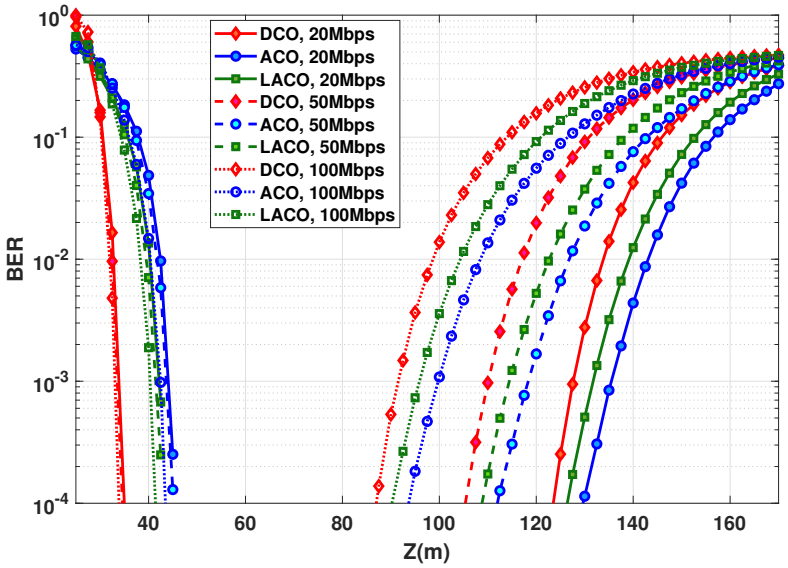

(a) $\eta \approx 1$ bps/Hz

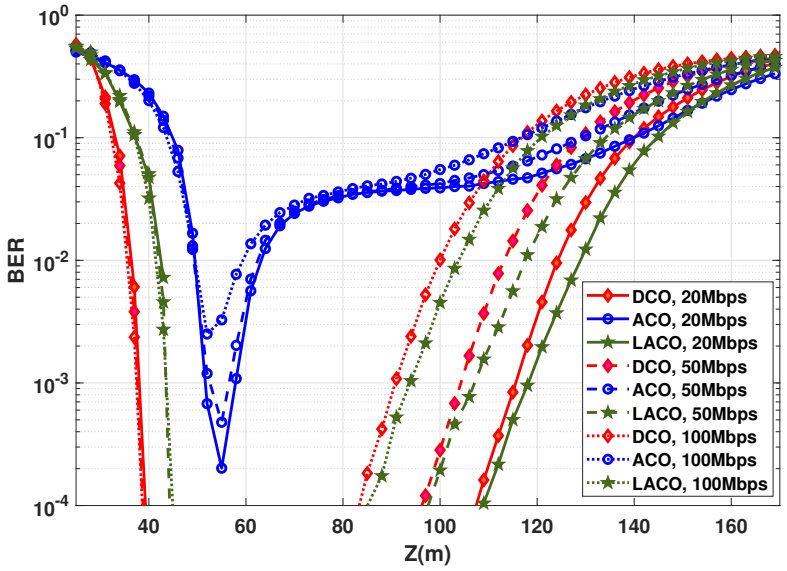

(b) $\eta \approx 2$ bps/Hz

Figure 5.16 — BER performance as a function of distance using 100 LEDs with $P_{\mathrm{Tx,e}} = 50$ mW for each; $N = 1024$. (a) $\eta \approx 1$ bps/Hz (e.g., 2-layer LACO and DCO-OFDM with 4-QAM) with $N_{\mathrm{CP}} = 9$, 20, and 28, for $R_b = 20$, 50, and 100 Mbps, respectively; (b) $\eta \approx 2$ bps/Hz (e.g., 3-layer LACO and DCO-OFDM with 16-QAM) with $N_{\mathrm{CP}} = 5$, 11, and 20, for $R_b = 20$, 50, and 100 Mbps, respectively.

required DC bias at the Tx for signal transmission, based on typical and practical LED characteristics. The presented results provide a reliable performance comparison of the considered schemes.

We showed that for moderate spectral efficiencies (namely $\sim 1\,\text{bps/Hz}$), LACO outperforms ADO- and HACO-OFDM while ACO-OFDM offers the best energy efficiency, i.e., it allows to attain the maximum link range for a given transmit electrical power. For relatively high spectral efficiencies (namely larger than $2\,\text{bps/Hz}$), ACO will suffer from high PAPR due to the required too large constellation size. There, LACO-OFDM becomes the best choice, as it makes a good compromise between PAPR reduction (with respect to ACO) and lower required DC bias at the Tx (with respect to DCO) at the cost of high computational complexity, especially when using more layers. Indeed, a high signal PAPR can result either in a high clipping noise level at the Tx side or a constrained link range due to SiPM saturation at the Rx side. Nevertheless, relaxing the constraint of $P_{\text{Tx,e}}$ at the Tx, we showed that DCO-OFDM is the most flexible scheme, offering the largest LBI, thus allowing a somehow more robust link operation when $P_{\text{Tx,e}}$ cannot be adaptively adjusted to the changing channel attenuation. Our study did not consider an optimization algorithm for power allocation of each layer when using hybrid O-OFDM schemes. Power allocation adjusting the optimal α for each layer can improve the performance of ACO-based schemes for a given constellation size; this can be studied further as discussed in [95].

Lastly, our study was based on a set of simplifying assumptions, including negligible turbulence effect, and perfect channel estimation and time synchronization. If these assumptions are not met in practice, the effect will be more or less the same for the three considered signaling schemes. In particular, the turbulence-induced channel fading and time synchronization errors will impact the link performance in the same way for the five schemes. Nevertheless, the impact of channel estimation errors can be more important for the case of LACO, HACO and ADO-OFDM, due to the successive detection used at the Rx and the risk of error propagation between layers due to imperfect channel state information, which needs further investigation.

Next chapter presents primary works for setting up a dedicated laboratory test-bed to assess the feasibility of the investigated transmission schemes for use in a real system.

CHAPTER 6

Experimental setup for an UWOC link

6.1 Introduction

In the previous chapters, we studied the performances of O-OFDM schemes for the SiPM-based UWOC links, based on numerical simulations. The next step is to validate our study through experiments. Due to the time constraint caused by the global pandemic, I did not have the time to complete this study. Therefore this chapter only presents the experimental setup and provide detail on the equipment used.

The rest of this chapter is organized as follows: Section 6.2 explains the experimental setup, including details of the various electrical and optical components. Section 6.3 concludes the chapter with some perspectives on the future studies.

6.2 Experimental setup description

Our test bench uses an aquarium filled with tap water and the optoelectronic used at the Tx and the Rx. The block diagram of the experimental link is shown in Fig. 6.1. The Tx block includes an arbitrary waveform generator (AWG) AFG1022 [103] and the LD driver CLD1010LP [104] with a pigtail single Mode Fiber [105]. Single mode pigtailed laser diodes are standard diodes that have been pigtailed to a 1 m long single-mode fiber. The optical signal output power is typically around 15 mW with a wavelength around 450 nm [104]. Here, we plan to start our experiment using a simple OOK modulation as a test; the binary data transmitted is randomly generated using Matlab software on the computer. The output bitstream is then fed into the AWG, which generates the corresponding electrical signal that will modulate the LD.

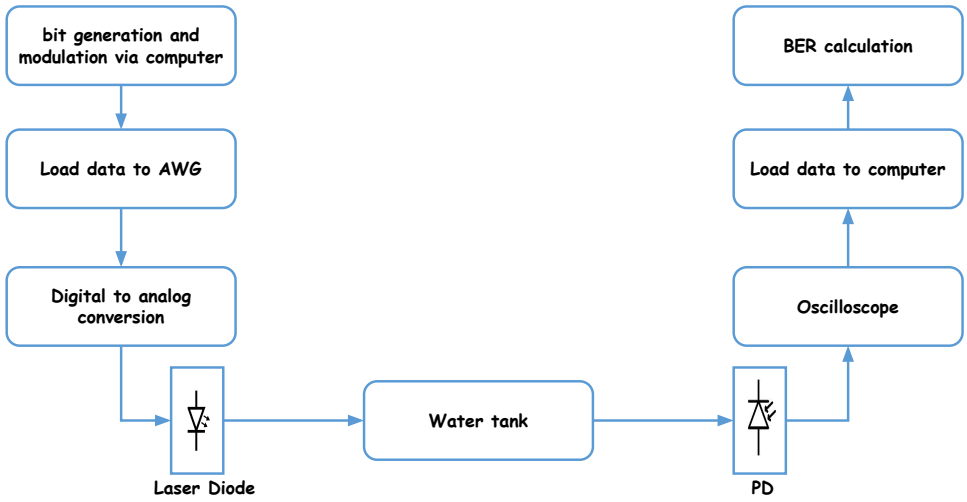

Figure 6.1 — Block diagram of the experimental setup.

The optical signal is transmitted via the aquarium of dimensions 100, 60, and 40 cm for length, width, and height, respectively (see Fig. 6.2), filled with tap water, considered a ”clear” water. The aquarium contains a filling and draining system, and is made of extra clair faces. To avoid the formation of algae, a filtering system is set up using a pump that allows continuously filtering of the water. Bleaching product was also added to purify the water (note that the bleach particles do not interfere with photons in the transmission). The collimator CFC8-A [106] is used after the optical fiber to maintain the same beam diameter throughout the trajectory. The optomechanic used to fix the laser diode fiber and the collimator are shown in Fig. 6.3.

It is worth mentioning that the light beam path contains an air channel (the small distance between the optoelectronic components and the aquarium) and a water channel. Please note that the refractive index of the glass in the aquarium is assumed to be equal to 1.

The use the of SiPM at Rx requires accurate calculation of the channel loss and setting of the transmit power due to the short distance between the Tx and Rx. First of all, we calculated the threshold value of the received optical signal that causes saturation. Based on the information provided by the manufacturer, for the wavelength of 470nm, the optical power resulting in SiPM saturation is about 5 nW. The SiPM is powered by a DC voltage generated by an external power supply using Keysight E3631A [107].

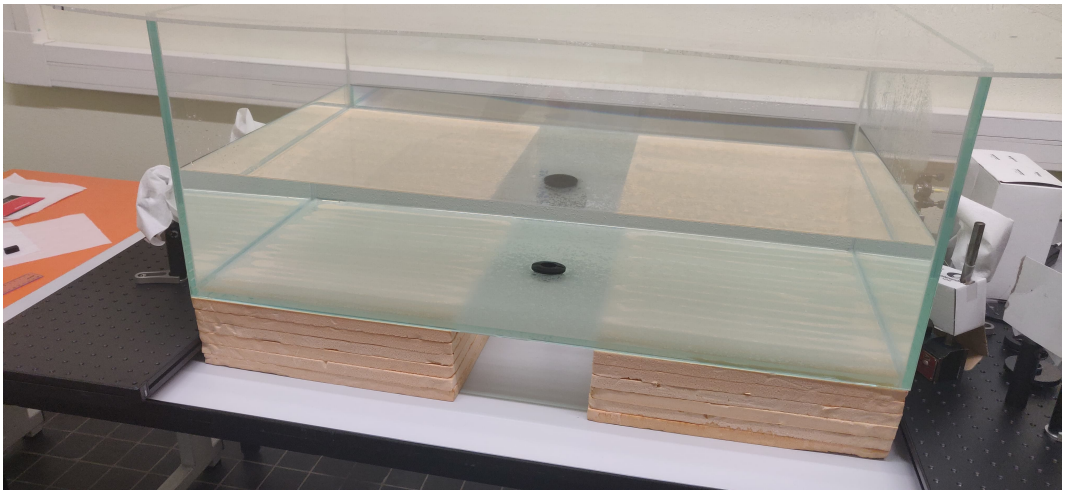

Figure 6.2 — Picture of the water tank used in the experiment

Optomechanical components from Thorlabs are also used to fix the SiPM and polarizers, lenses, etc., in the optical table. In order to validate the experiment before deploying the SiPM, we used a PDA10A2 [108] as a test. The PDA10A2 module consist of a reverse-biased PIN photodiode connected to a fixed-gain trans-impedance amplifier, designed to detect signals with wavelengths ranging from 200 to 1100 nm.

The electrical signal from the PD output is then sent to an digital oscilloscope with an integrated analog-to-digital converter (ADC). The digital data is then sent to the computer for signal demodulation using Matlab and BER estimation. The experiment is designed to be performed under dark conditions with no solar light presence.

So far, we were able to set the different equipment of the experiment except for the PIN PD, the binary data was saved in a USB drive, and we were able to generate the signal through the AWG. Fig. 6.4 shows an idea about the setup when it is complete.

6.3 This part is still going on

In this chapter, we presented the experimental setup to evaluate later the performance of an UWOC link using a SiPM. The next step will focus on conducting experiments with SiPM to assess the practical constraints and then to use an FPGA board to convert a video sequence into bits and transmit these bits through the aquatic channel. An FPGA board will be used at the receiver to reconstruct the same video on the receiver side.

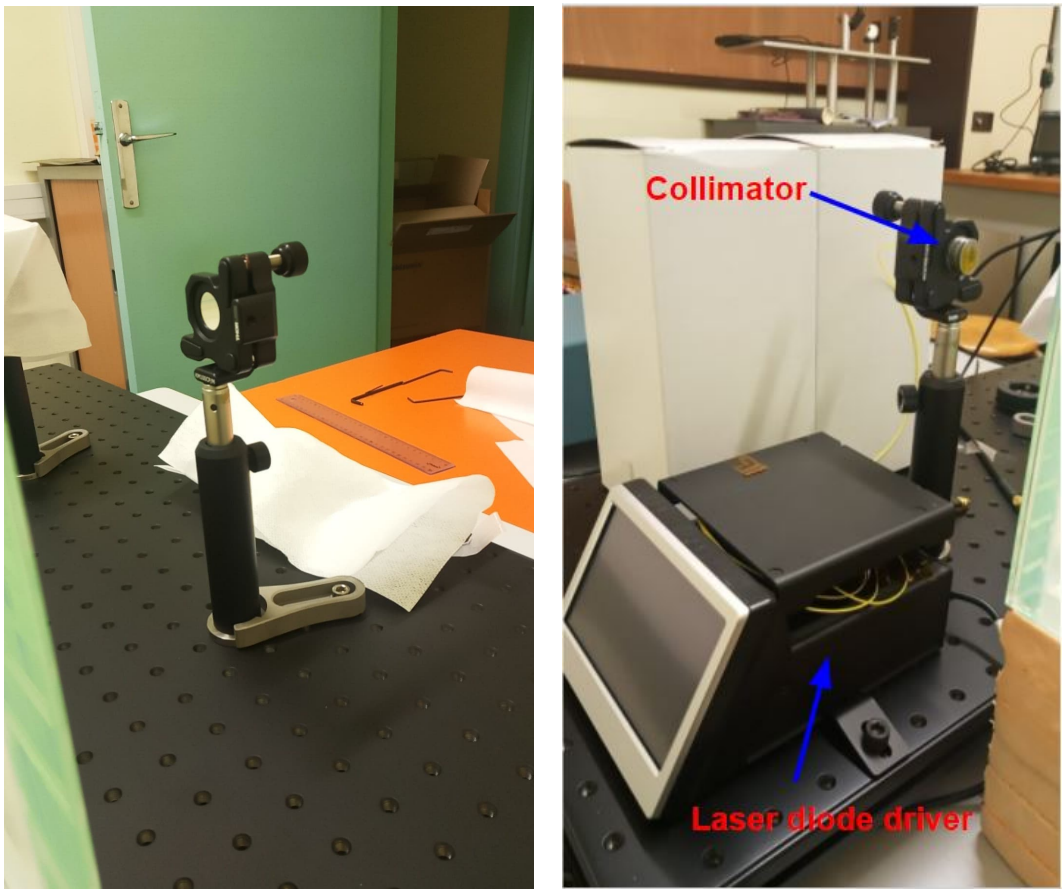

(a) Reflection mirror (b) Laser Diode + Collimator

Figure 6.3 — Pictures of laser diode and mirror used in the experiment

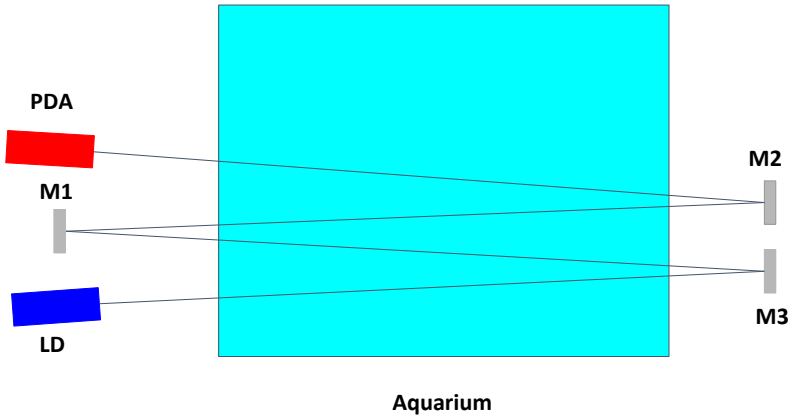

Figure 6.4 — Transmission link using mirrors (M1, M2, and M3) to extend the distance between Tx and Rx

CHAPTER 7

Conclusions and perspectives

7.1 Conclusions

Underwater optical wireless communication is a promising technology, especially when it comes to transmit with high data rates over a moderate distance. However, it is concerned with strong signal attenuation when transmitting over long distances. Moreover, the establishment of relatively high data rate link is challenged by the limited bandwidth of the opto-electronic components employed at the Tx and at the Rx. To address these issues, we focused in this thesis on investigating the use of high sensitive PDs, i.e., SiPMs, as well as O-OFDM signaling, to improve the performance link.

Chapter 3 presented the use of SiPMs in UWOC applications. We explained in detail the operating principles and is mathematical model for the transmission link. As an SiPM can be considered a photon-counting device, we consider the poisson distribution to model the number of photons counted which is proportional to the intensity of the received optical signal when operating in linear mode. We also described the effect of non-linear distortion of the SiPM-based Rx and how it impacts the number of the effectively detected photons. Afterwards, we investigated the performance of the SiPM Rx in a typical UWOC link using the OOK modulation scheme and showed that the LBI and the maximum attainable range $Z_{\max}$ values depend on the transmit electrical power $P_{\mathrm{Tx},e}$ and that for a higher data rate R_b, the link performance degrades due to a shorter symbol duration T_s.

To deal with the issue of the limited bandwidth of the opto-electronic component based on O-OFDM signaling, we investigated DCO-OFDM scheme in Chapter 4. We considered two approaches to set the DC bias of DCO-OFDM, taking into account the

scaling factor needed to adapt the signal to the DR of the LED. The optimal method to fix the DC bias showed little interest in practice than the classical bias setting method since it requires a relatively high computational accuracy. Meanwhile, we briefly showed the importance of using an SiPM with a low DCR to increase the link flexibility and maximum attainable range. Lastly, we investigated the impact of LED non-linearity on the performance of the link, since a low DCR is equivalent to a high PD sensitivity and showed its effect is decreasing the maximum attainable link as well as link flexibility.

Next, we identified in Chapter 5 the most suitable O-OFDM schemes in our application, namely, the DCO, ACO, LACO, HACO and ADO-OFDM, and investigated their performance in detail. We showed that for moderate spectral efficiencies (namely ~ 1 bps/Hz), ACO-OFDM offers the best energy efficiency, i.e., it allows to attain the maximum link range for a given transmit electrical power. For higher spectral efficiencies (namely larger than 2 bps/Hz), ACO will suffer from high PAPR due to the required too large constellation size. There, the three-layer LACO becomes the suitable choice, as it makes a good compromise between PAPR reduction (with respect to ACO) and the required DC bias at the Tx (with respect to DCO). Nevertheless, LACO requires a relatively high computational complexity, especially when using multiple layers, which increases the Rx delay latency. We showed that DCO-OFDM is the most flexible scheme, offering the largest LBI. Also, LED arrays can be used and adjusted to control the link range of the transmission link, assuming perfect knowledge of the channel parameters. Finally, initial works on the design and implementation of an experimental test-bed were presented in Chapter 6.

7.2 Perspectives for future research

This thesis was dedicated to the study of the performance of O-OFDM schemes in UWOC links using SiPM receivers to overcome the limited bandwidth of opto-electronic components and to allow increasing the data rate and the range at the same time. The work presented in this thesis meets the objectives presented in Chapter 1, but there are still several other remaining directions for future research.

Naturally, the first (i,e,. short-term) perspective is to carry out the experiments using the prepared test-bed, and to study the practical interest of the investigated O-OFDM schemes. In longer terms, the experimental setup can be equipped with FPGA boards at the Tx and at the Rx in order to realize real-time data transmission, e.g., a high-definition video sequence.

Furthermore, as a future extension of this work, a more detailed analysis could be done on the impact of DCR on the link performance. As shown Section 4.7, the maximum attainable link and flexibility increase considerably when lowering the DCR value. Indeed, to guarantee a lower SiPM receiver temperature, the system will consume more power, but the gain in terms of range is remarkable. In the future, the electrical power consumption of the Rx could be investigated as a function of LBI while using a cooling system. This study could help decide if it is interesting to use SiPM with a cooling system or increase only the transmitting power.

In Chapter 5, we mentioned HPAM-DMT, a recently proposed technique in [93] , which has close performances to LACO with a somehow lower computational complexity. Future work can also consider the enhanced O-OFDM scheme proposed in [109–111], which aims at compensating the loss of bandwidth due to hermitian symmetry in order to increase the SE.

Spatial multiplexing techniques could be used to increase UWOC link span and performance, such as multiple-input-multiple-out (MIMO) architectures [112], using arrays of LEDs and SiPM at the Tx and the Rx, respectively. Furthermore, LEDs with different wavelengths can be used to multiplex signal on different wavelengths and further improve the link throughput. There, since the signal is not attenuated equally within the visible spectrum, the corresponding constellation sizes or the transmit electrical powers can be adjusted for each wavelength to optimize the overall link performance.

APPENDIX A

Noise-signal independency in the frequency domain

The received time domain signal r can be written as follow :

$$r = x + n \tag{A.1}$$

x denotes the transmitted signal in the time domain and n denotes the shot noise and the thermal noise, please note that in this thesis we have neglected the thermal noise because we have a dominant shot noise from using SiPM, but for the sake of this demonstration we consider both noises. n is a zero mean signal-dependent additive Gaussian noise with variance σ^2 defined as [74] :

$$\sigma^2 = \beta x + \sigma_0^2 \tag{A.2}$$

where β is a coefficient depending on the SiPM characteristics and σ_0^2 is the signal-independent noise including thermal and background noise.

From equation (4.2), the received optical signal $\hat{R}_k$ in the frequency domain can be written as :

$$\hat{R}_k = \frac{1}{\sqrt{N}}\left[\sum_{n=0}^{N-1} r_n \cos\left(\frac{2\pi}{N}nk\right) + j\sum_{n=0}^{N-1} r_n \sin\left(\frac{2\pi}{N}nk\right)\right], \quad k = 0, ..., N-1. \tag{A.3}$$

The strength of the noise in the frequency domain can be calculated as the variance

of the frequency domain samples, $Var(\hat{R}_k|x_n)$, given the samples of the transmitted signal x_n are known [74].

Let's denote by $R(\hat{R}_k)$ and $I(\hat{R}_k)$ the real and imaginary part of $\hat{R}_k$, the variance can be calculated as follow :

$$\begin{aligned}
Var(R(\hat{R}_k)|x_n) &= \mathbb{E}\Big[\Big(\frac{1}{\sqrt{N}}\Big[\sum_{n=0}^{N-1} r_n \cos\Big(\frac{2\pi}{N}nk\Big)\Big] - \mathbb{E}\Big(\frac{1}{\sqrt{N}}\Big[\sum_{n=0}^{N-1} r_n \cos\Big(\frac{2\pi}{N}nk\Big)|x_n\Big]\Big)\Big)^2 |x_n\Big] \\
&= \mathbb{E}\Big[\Big(\frac{1}{\sqrt{N}}\Big[\sum_{n=0}^{N-1} (x_n + n_n) \cos\Big(\frac{2\pi}{N}nk\Big)\Big] - \frac{1}{\sqrt{N}}\Big[\sum_{n=0}^{N-1} x_n \cos\Big(\frac{2\pi}{N}nk\Big)\Big]\Big)^2 |x_n\Big] \\
&= \mathbb{E}\Big[\Big(\frac{1}{\sqrt{N}}\Big[\sum_{n=0}^{N-1} n_n \cos\Big(\frac{2\pi}{N}nk\Big)\Big]\Big)^2 |x_n\Big] \\
&= \frac{1}{N}\Big[\sum_{n=0}^{N-1} \mathbb{E}(n_n^2|x_n) \cos^2\Big(\frac{2\pi}{N}nk\Big)\Big]
\end{aligned} \tag{A.4}$$

From equation (A.2), the variance $Var(R(\hat{r}_k)|x_n)$ can be written as [74] :

$$\begin{aligned}
Var(R(\hat{R}_k)|x_n) &= \frac{1}{N}\Big[\sum_{n=0}^{N-1} (\beta x_n + \sigma_0^2)\Big(\frac{1 + \cos\frac{4\pi}{N}nk}{2}\Big)\Big] \\
&= \frac{1}{N}\Big[\sum_{n=0}^{N-1} (\frac{\beta x_n + \sigma_0^2}{2})\Big] \\
&= \frac{\beta\eta_x + \sigma_0^2}{2}
\end{aligned} \tag{A.5}$$

where $\eta_x = \frac{1}{N}(\sum_{n=0}^{N-1} x_n)$ is the average of the signal x, this equality comes from the fact that N is a large number [74]. Similar results can be proved for the imaginary part of the received signal :

$$\begin{aligned}
Var(I(\hat{r}_k)|x_n) &= \frac{1}{N}\Big[\sum_{n=0}^{N-1} \mathbb{E}(n_n^2|x_n) \sin^2\Big(\frac{2\pi}{N}nk\Big)\Big] \\
&= \frac{1}{N}\Big[\sum_{n=0}^{N-1} (\beta x_n + \sigma_0^2)\Big(\frac{1 - \cos\frac{4\pi}{N}nk}{2}\Big)\Big] \\
&= \frac{\beta\eta_x + \sigma_0^2}{2}
\end{aligned} \tag{A.6}$$

From Equation (A.5) and (A.6) we conclude that the strength of the noise in the frequency domain does not depend on the signal amplitude of each sample. In other words, when applying FFT, signal samples can be considered noise-independent.

Bibliography

[1] H. M. Oubei T. K. Ng G. Liu K. H. Park K. T. Ho M. S. Alouini C. Shen, Y. Guo and B. S. Ooi, "20-meter underwater wireless optical communication link with 1.5 Gbps data rate," *Opt. Express*, vol. 24, no. 22, pp. 25502–25509, Oct 2016.

[2] C. Lorenzo S. S. Giuseppe and L. Fabio, "Underwater optical wireless communications: Overview," *MDPI, Sensors*, vol. 20, no. 8, 2020.

[3] H. Kaushal and G. Kaddoum, "Underwater optical wireless communication," *IEEE Access*, vol. 4, 2016.

[4] Hamamatsu S. Piatek, "What is an sipm and how does it work?," 2011, available at https://hub.hamamatsu.com/jp/en/technical-note/how-sipm-works/index.html, Rev. 2020-09-14.

[5] NICHIA Corporation., "Specifications for blue LED: NSPB510AS, available at http://www.nichia.co.jp, 2020-09-20," .

[6] "Hamamatsu. MPPC modules data-sheet, GA types, C13366 Series," 2020, available at https://www.hamamatsu.com/resources/pdf/ssd/c13366-1350ga_etc_kacc1228e.pdf.

[7] F. Klingelhoefer and M. A. Gutscher, "Rov victor 6000, available at https://image.ifremer.fr/data/00655/76752/," 2020.

[8] B. Ambre, "Sous-marin auv ulyx dans le hall du centre de la seyne-sur-mer, available at https://image.ifremer.fr/data/00656/76771/," 2020.

[9] S. Milica, *Underwater Acoustic Communication*, pp. 1–12, American Cancer Society, 2015.

[10] S. Shiraz C. Mandar and S. Milica, "Underwater acoustic communications and networking: Recent advances and future challenges," *Marine Technology Society Journal*, vol. 42, no. 1, pp. 103–116, March 2008.

[11] D. Pompili I. F. Akyildiz and T. Melodia, "Underwater acoustic sensor networks: research challenges," *Ad Hoc Networks*, vol. 3, no. 3, pp. 257 – 279, May 2005.

[12] Y. KIDA T. SHIMURA and M. DEGUCHI, "High-rate acoustic communication at the data rate of 69 kbps over the range of 3,600 m developed for vertical uplink communication," in *OCEANS 2019 - Marseille*, 2019, pp. 1–6.

[13] H. Brundage, "Designing a wireless underwater optical communication system," Feb. 2006.

[14] Y. A. Chursin S. Affes M. F. Ali, D. N. K. Jayakody and S. Dmitry, "Recent advances and future directions on underwater wireless communications," *Archives of Computational Methods in Engineering*, pp. 1379 – 1412, 2020.

[15] F. Hanson and S. Radic, "High bandwidth underwater optical communication," *Applied Optics*, vol. 47, no. 2, pp. 277–283, Jan. 2008.

[16] L. J. Mullen B. M. Cochenour and A. E. Laux, "Characterization of the beam-spread function for underwater wireless optical communications links," *IEEE Journal of Oceanic Engineering*, vol. 33, no. 4, pp. 513–521, Oct. 2008.

[17] T. Hamza S. Bourennane P. Leon M. A. Khalighi, C. Gabriel and V. Rigaud, "Underwater wireless optical communication; recent advances and remaining challenges," *IEEE International Conference on Transparent Optical Networks (ICTON)*, pp. 1–4, July 2014, Invited paper, Graz, Austria.

[18] L. N. Alves Z. Ghassemlooy, S. Zvànovec, and M. A. Khalighi, Eds., *Visible Light Communications: Theory and Applications*, CRC-Press, 2017.

[19] M. Kong O. Alkhazragi Y. Guo M. Ouhssain Y. Weng B. H. Jones T. K. Ng X. Sun, C. H. Kang and B. S. Ooi, "A review on practical considerations and solutions in underwater wireless optical communication," *Journal of Lightwave Technology*, vol. 38, no. 2, pp. 421–431, Jan. 2020.

[20] R. J. Green L. J. Johnson and M. S. Leeson, "Hybrid underwater optical/acoustic link design," in *2014 16th International Conference on Transparent Optical Networks (ICTON)*, 2014, pp. 1–4.

[21] S. Bourennane P. Leon C. Gabriel, M. Khalighi and V. Rigaud, "Monte-carlo-based channel characterization for underwater optical communication systems," *Journal of Optical Communications and Networking*, vol. 5, pp. 1–12, 2013.

[22] M. Khalighi, T. Hamza, S. Bourennane, P. Leon, and J. Opderbecke, "Underwater wireless optical communications using silicon photo-multipliers," *IEEE Photonics Journal*, vol. 9, no. 4, pp. 1–10, 2017.

[23] R. Henderson Y. Li, M. Safari and H. Haas, "Nonlinear distortion in spad-based optical ofdm systems," in *2015 IEEE Globecom Workshops (GC Wkshps)*, February 2015, pp. 1–6.

[24] S. Bourennane P. Leon C. Gabriel, M. A. Khalighi and V. Rigaud, "Investigation of suitable modulation techniques for underwater wireless optical communication," in *2012 International Workshop on Optical Wireless Communications (IWOW)*, 2012.

[25] C. Gabriel, *Channel Characterization and performance analysis for an underwater optical transmission system*, Ph.D. thesis, Ecole Centrale Marseille, May 2013.

[26] M. A. Khalighi F. Xu and S. Bourennane, "Coded PPM and multipulse PPM and iterative detection for free-space optical links," *J. Opt. Commun. Netw.*, vol. 1, no. 5, pp. 404–415, Oct 2009.

[27] S. Long, *Development of Transmission Methods for a High Data Rate Free Space Optical Communication System*, Ph.D. thesis.

[28] M. A. Khalighi F. Xu and S. Bourennane, "Efficient channel coding for multipulse pulse position modulation in terrestrial FSO systems," in *Free-Space Laser Communications IX*, A. K. Majumdar and C. C. Davis, Eds. International Society for Optics and Photonics, 2009, vol. 7464, pp. 204 – 215, SPIE.

[29] T. Hamza, *Underwater Wireless Optical Communications: Long-range High-data-rate Transmission and Performance Analysis*, Ph.D. thesis, Ecole Centrale Marseille, March 2017.

[30] S. Long, *Indoor Channel Modeling and high Data-Rate Transmission for Visible Light Communication Systems*, Ph.D. thesis.

[31] T. Hamza and M. A. Khalighi, "On limitations of using silicon photo-multipliers for underwater wireless optical communications," in *2019 2nd West Asian Colloquium on Optical Wireless Communications (WACOWC)*, April 2019, pp. 74–79.

[32] H. Akhouayri M. A. Khalighi and S. Hranilovic, "Silicon-photomultiplier-based underwater wireless optical communication using pulse-amplitude modulation," *IEEE Journal of Oceanic Engineering*, pp. 1–11, July 2019.

[33] R. van Nee and R. Prasad, OFDM for Wireless Multimedia Communications, Artech House, Inc.685 Canton St. Norwood, MAUnited States, 1999.

[34] H. Hijazi E. P. Simon, L. Ros and M. Ghogho, "Joint carrier frequency offset and channel estimation for OFDM systems via the EM algorithm in the presence of very high mobility," *IEEE Transactions on Signal Processing*, vol. 60, no. 2, pp. 754–765, Oct. 2012.

[35] Inst Tools, "Laser diode working principle," available at https://instrumentationtools.com/laser-diode-working-principle/, Rev. 2020-09-10.

[36] B. Janjua H.Y. Wang C.T. Tsai Y.C. Chi T.K. Ng H.C. Kuo J.H. He M.S. Alouini G.R. Lin H.M. Oubei, J.R. Duran and B.S. Ooi, "4.8 Gbit/s 16-QAM-OFDM transmission based on compact 450-nm laser for underwater wireless optical communication," *Opt. Express*, vol. 23, no. 18, pp. 23302–23309, Sep 2015.

[37] K. Nakamura, I. Mizukoshi, and M. Hanawa, "Optical wireless transmission of 405 nm, 1.45 Gbit/s optical IM/DD-OFDM signals through a 4.8 m underwater channel," *Opt. Express*, vol. 23, no. 2, pp. 1558–1566, Jan 2015.

[38] T. Ali J. Wang R. Sarwar J. Han C. Guo B. Sun N. Deng Y. Chen, M. Kong and J. Xu, "26 m/5.5 Gbps air-water optical wireless communication based on an OFDM-modulated 520-nm laser diode," *Opt. Express*, vol. 25, no. 13, pp. 14760–14765, Jun 2017.

[39] S. Li J. Wang, C. Lu and Z. Xu, "100 m/500 Mbps underwater optical wireless communication using an NRZ-OOK modulated 520 nm laser diode," *Opt. Express*, vol. 27, no. 9, pp. 12171–12181, Apr 2019.

[40] X. Yu A. Lin M. Kong J. Han J. Xu, Y. Song and N. Deng, "Underwater wireless transmission of high-speed QAM-OFDM signals using a compact red-light laser," *Opt. Express*, vol. 24, no. 8, pp. 8097–8109, Apr 2016.

[41] Rhom Semiconductor, "Light emitting diode," available at https://www.rohm.com/electronics-basics/leds/what-are-ledsRev. 2020-09-10.

[42] A. Lin Y. Song X. Yu F. Qu J. Han J. Xu, M. Kong and N. Deng, "OFDM-based broadband underwater wireless optical communication system using a compact blue LED," *Optics Communications*, vol. 369, pp. 100 – 105, 2016.

[43] S. Yi Y. Huang S. Zhang X. Zhou L. Hu L. Zheng P. Tian, X. Liu and R. Liu, "High-speed underwater optical wireless communication using a blue GaN-based micro-LED," *Opt. Express*, vol. 25, no. 2, pp. 1193–1201, Jan 2017.

[44] H. Y. Wang C. T. Tsai Tsai-Chen Wu, Y. C. Chi and G. R. Lin, "Blue laser diode enables underwater communication at 12.4âGbps," *Scientific Reports*, vol. 7, no. 40480, 2017.

[45] W. Popoola Z. Ghassemlooy and S. Rajbhandari, *Optical Wireless Communications: System and Channel Modelling with* MATLAB, CRC Press, 2012.

[46] Hamamatsu, "Basic principles of photomultiplier tubes," available at https://www.hamamatsu.com/resources/pdf/etd/PMT_handbook_v3aE-Chapter2.pdf, Rev. 2020-09-10.

[47] L. Mullen B. Cochenour and J. Muth, "Temporal response of the underwater optical channel for high-bandwidth wireless laser communications," *IEEE Journal of Oceanic Engineering*, vol. 38, no. 4, pp. 730–742, July 2013.

[48] sonardyne, "available at https://www.sonardyne.com," .

[49] X. Zhu and J. M. Kahn, "Free-space optical communication through atmospheric turbulence channels," *IEEE Transactions on Communications*, vol. 50, no. 8, pp. 1293–1300, August 2002.

[50] Z. Ghassemlooy D. G. Michelson M. Omoomi Z. Vali, A. Gholami and H. Noori, "Modeling turbulence in underwater wireless optical communications based on monte carlo simulation," *J. Opt. Soc. Am. A*, vol. 34, no. 7, pp. 1187–1193, Jul 2017.

[51] A. Kammoun M. Hamdi B. S. Ooi E. Zedini, H. M. Oubei and M. Alouini, "Unified statistical channel model for turbulence-induced fading in underwater wireless optical communication systems," *IEEE Transactions on Communications*, vol. 67, no. 4, pp. 2893–2907, Jan. 2019.

[52] R. T. ElAfandy A. Kammoun M. Abdallah T. K. Ng M. Hamdi M. S. Alouini H. M. Oubei, E. Zedini and B. S. Ooi, "Simple statistical channel model for weak

temperature-induced turbulence in underwater wireless optical communication systems," *Opt. Lett.*, vol. 42, no. 13, pp. 2455–2458, Jul 2017.

[53] "Performance analysis of underwater wireless optical communication systems over a wide range of optical turbulence," *Optics Communications*, vol. 427, pp. 609 – 616, June 2018.

[54] A. Babiker and N. Zakaria, "Energy efficient communication for underwater wireless sensors networks," 2012.

[55] S. Bourennane P. Leon T. Hamza, M. A. Khalighi and J. Opderbecke, "Investigation of solar noise impact on the performance of underwater wireless optical communication links," *Optics Express*, vol. 24, no. 22, pp. 25832–25845, Oct. 2016.

[56] H. Zhang and Y. Dong, "Link misalignment for underwater wireless optical communications," in *2015 Advances in Wireless and Optical Communications (RTUWO)*, December 2015.

[57] Y. Dong J. Liu and H. Zhang, "On received intensity for misaligned underwater wireless optical links," in *OCEANS 2016 - Shanghai*, June 2016.

[58] B. L. Hughes J. A. Simpson and J. F. Muth, "Smart transmitters and receivers for underwater free-space optical communication," *IEEE Journal on Selected Areas in Communications*, vol. 30, no. 5, pp. 964–974, June 2012.

[59] ON Semiconductors, "Introduction to the silicon photomultiplier (SiPM)," July 2018.

[60] L. Brignone J. Opderbecke J. Greer M. A. Khalighi T. Hamza S. Bourennane P. Leon, F. Roland and M. Bigand, "A new underwater optical modem based on highly sensitive silicon photomultipliers," in *OCEANS 2017 - Aberdeen*, June 2017, pp. 1–6.

[61] X Chen C. Zhang M. Kong Z. Tong J. Shen, J. Wang and J. Xu, "Towards power-efficient long-reach underwater wireless optical communication using a multi-pixel photon counter," *Opt. Express*, vol. 26, no. 18, pp. 23565–23571, Sep 2018.

[62] C. Yu X. Chen J. Wu M. Zhao F. Qu Z. Xu J. Han J. Shen, J. Wang and J. Xu, "Single led-based 46-m underwater wireless optical communication enabled by a multi-pixel photon counter with digital output," *Optics Communications*, vol. 438, pp. 78 – 82, January 2019.

[63] C. Sun Z. Chen Z. Li H. Wang R. Jiang W. Shi A. Zhang L. Zhang, X. Tang, "Over 10 attenuation length gigabits per second underwater wireless optical communication using a silicon photomultiplier (SiPM) based receiver," *Opt. Express*, vol. 28, no. 17, pp. 24968–24980, Aug 2020.

[64] R. Sarwar B. Sun Z. Xu J. Han J. Chen H. Qin M. Kong, Y. Chen and J. Xu, "Underwater wireless optical communication using an arrayed transmitter/receiver and optical superimposition-based 4-PAM signal," *Opt. Express*, vol. 26, no. 3, pp. 3087–3097, Feb 2018.

[65] C. Sun Z. Chen Z. Li H. Wang R. Jiang W. Shi A. Zhang L. Zhang, X. Tang, "Over 10 attenuation length gigabits per second underwater wireless optical communication using a silicon photomultiplier (SiPM) based receiver," *Opt. Express*, vol. 28, no. 17, pp. 24968–24980, Aug 2020.

[66] N. Otte, "The silicon photomultiplier - a new device for high energy physics, astroparticle physics, industrial and medical applications," in *IX International Symposium on Detectors for Particle, Astroparticle and Synchrotron Radiation Experiments, SNIC Symposium, Stanford, California*, April 2006.

[67] Sensl, "An introduction to the silicon photomultiplier," 2011, available at https://www.sensl.com/downloads/ds/TN%20-%20Intro%20to%20SPM%20Tech.pdf, Rev. 2020-09-13.

[68] F. Acerbi and S. Gundacker, "Understanding and simulating SiPMs," *Nuclear Instruments and Methods in Physics Research Section A: Accelerators, Spectrometers, Detectors and Associated Equipment*, vol. 926, pp. 16 – 35, 2019, Silicon Photomultipliers: Technology, Characterisation and Applications.

[69] A. Para, "Afterpulsing in silicon photomultipliers: Impact on the photodetectors characterization," 2015.

[70] X. Chen, *Study of the Silicon Photomultipliers and Their Applications in Positron Emission Tomography*, Ph.D. thesis, Hamburg University:, 2016.

[71] E. Sarbazi, M. Safari, and H. Haas, "Statistical modeling of single-photon avalanche diode receivers for optical wireless communications," *IEEE Transactions on Communications*, vol. 66, no. 9, pp. 4043–4058, April 2018.

[72] R. Henderson Y. Li, M. Safari and H. Haas, "Performance analysis of SPAD-based OFDM," 2019.

[73] M. A. Khalighi F. Xu and S. Bourennane, "Impact of different noise sources on the performance of PIN- and APD-based FSO receivers," June 2011, pp. 211–218, Graz, Austria.

[74] M. Safari, "Efficient optical wireless communication in the presence of signal-dependent noise," in *2015 IEEE International Conference on Communication Workshop (ICCW)*, June 2015, pp. 1387–1391.

[75] P. A. Haigh P. Chvojka, S. Zvanovec and Z. Ghassemlooy, "Channel characteristics of visible light communications within dynamic indoor environment," *Journal of Lightwave Technology*, vol. 33, no. 9, pp. 1719–1725, Feb. 2015.

[76] "IEEE standard for information technology – telecommunications and information exchange between systems local and metropolitan area networks–specific requirements - Part 11: Wireless LAN medium access control (MAC) and physical layer (PHY) specifications amendment: Light communications," May 2018.

[77] J. Armstrong, "OFDM for optical communications," *IEEE/OSA Journal of Lightwave Technology*, vol. 27, no. 3, pp. 189–204, Feb. 2009.

[78] M.A. Khalighi, S. Long, S. Bourennane, and Z. Ghassemlooy, "PAM- and CAP-Based transmission schemes for visible-light communications," *IEEE Access*, vol. 5, Oct. 2017.

[79] Y. Hong N. Fernando and E. Viterbo, "Flip-OFDM for unipolar communication systems," *IEEE Transactions on Communications*, vol. 60, no. 12, pp. 3726–3733, Dec. 2012.

[80] S. Sinanovic D. Tsonev and H. Haas, "Novel unipolar orthogonal frequency division multiplexing (U-OFDM) for optical wireless," in *IEEE Vehicular Technology Conference (VTC Spring)*, May 2012, pp. 1–5, Yokohama, Japan.

[81] D. Tsonev and H. Haas, "Avoiding spectral efficiency loss in unipolar OFDM for optical wireless communication," in *IEEE International Conference on Communications (ICC)*, June 2014, p. 3336â3341, Sydney, NSW, Australia.

[82] D. Tsonev M. S. Islim and H. Haas, "On the superposition modulation for OFDM-based optical wireless communication," in *IEEE Global Conference on Signal and Information Processing (GlobalSIP)*, Dec. 2015, pp. 1022–1026, Orlando, FL.

[83] F. Breyer S. C. J. Lee, S. Randel and A. M. J. Koonen, "PAM-DMT for intensity-modulated and direct-detection optical communication systems," *IEEE Photonics Technology Letters*, Dec. 2009.

[84] W. Popoola A. Goldsmith and S. Rajbhandari, *Wirless Communications*, Cambridge University Press, 2015.

[85] W. Lv C. Yu J. Wu M. Zhao F. Qu Z. Xu J. Han J. Wang, X. Yang and J. Xu, "Underwater wireless optical communication based on multi-pixel photon counter and OFDM modulation," *Optics Communications*, vol. 451, pp. 181 – 185, June 2019.

[86] J. Armstrong and B. J. C. Schmidt, "Comparison of asymmetrically clipped optical OFDM and DC-biased optical OFDM in AWGN," *IEEE Communications Letters*, vol. 12, no. 5, pp. 343–345, May 2008.

[87] M. Zhang and Z. Zhang, "An optimum DC-Biasing for DCO-OFDM system," *IEEE Communications Letters*, vol. 18, no. 8, pp. 1351–1354, Aug. 2014.

[88] "B-series fast, blue-sensitive silicon photomultiplier sensors datasheet," available at http://www.sensl.com/downloads/ds/DS-MicroBseries.pdf Rev. 01-09-2020.

[89] S. Videv D. Tsonev and H. Haas, "Unlocking spectral efficiency in intensity modulation and direct detection systems," *IEEE Journal on Selected Areas in Communications*, vol. 33, no. 9, pp. 1758–1770, 2015.

[90] S. D. Dissanayake and J. Armstrong, "Comparison of ACO-OFDM, DCO-OFDM and ADO-OFDM in IM/DD systems," *Journal of Lightwave Technology*, vol. 31, no. 7, pp. 1063–1072, Apr. 2013.

[91] B. Ranjha and M. Kavehrad, "Hybrid asymmetrically clipped OFDM-Based IM/DD optical wireless system," *IEEE/OSA Journal of Optical Communications and Networking*, vol. 6, no. 4, pp. 387–396, Apr. 2014.

[92] X. Guo Z. Wang D. G. Cunningham Q. Wang, C. Qian and I. H. White, "Layered ACO-OFDM for intensity-modulated direct-detection optical wireless transmission," *Optics Express*, vol. 23, no. 9, pp. 12382–12393, May 2015.

[93] S. Feng B. Li and W. Xu, "Spectrum-efficient hybrid PAM-DMT for intensity-modulated optical wireless communication," *Opt. Express*, vol. 28, no. 9, pp. 12621–12637, Apr 2020.

[94] A. J. Lowery, "Comparisons of spectrally-enhanced asymmetrically-clipped optical OFDM systems," *Optics Express*, vol. 24, no. 4, pp. 3950–3966, Feb. 2016.

[95] F. Yang Y. Sun and J. Gao, "Comparison of hybrid optical modulation schemes for visible light communication," *IEEE Photonics Journal*, vol. 9, no. 3, pp. 1–13, June 2017.

[96] F. Yang Y. Sun and L. Cheng, "An overview of OFDM-based visible light communication systems from the perspective of energy efficiency versus spectral efficiency," *IEEE Access*, vol. 6, pp. 60824–60833, Oct. 2018.

[97] R. Zhang S. Chen X. Zhang, Q. Wang and L. Hanzo, "Performance analysis of layered ACO-OFDM," *IEEE Access*, vol. 5, pp. 18366–18381, Sept. 2017.

[98] R. Bai and S. Hranilovic, "Absolute value layered ACO-OFDM for intensity-modulated optical wireless channels," *IEEE Transactions on Communications*, 2020, In Press.

[99] F. Wang L. Dai R. Jiang, Q. Wang and Z. Wang, "An optimal scaling scheme for DCO-OFDM based visible light communications," *Optics Communications*, vol. 356, pp. 136–140, Dec. 2015.

[100] S. Dimitrov and H. Haas, "Optimum signal shaping in OFDM-Based optical wireless communication systems," in *Vehicular Technology Conference (VTC Fall)*, Sept. 2012, pp. 1–5, Québec City, Canada.

[101] Q. Wang R. Bai and Z. Wang, "Asymmetrically clipped absolute value optical OFDM for intensity-modulated direct-detection systems," *Journal of Lightwave Technology*, vol. 35, no. 17, pp. 3680–3691, 2017.

[102] T. Essalih M. A. Khalighi, S. Hranilovic and Akhouayri H, "Optical OFDM for SiPM-Based underwater optical wireless communication links," *Sensors*, vol. 20, no. 21, pp. 6057, Oct 2020.

[103] Thorlabs, "Arbitrary waveform generator," available at https://fr.rs-online.com/web/p/generateur-dondes/8555078/ Rev. 2020-11-26.

[104] Thorlabs, "Laser driver," available at https://www.thorlabs.com/newgrouppage9.cfm?objectgroup_ID=7752 Rev. 2020-11-26.

[105] Thorlabs, "pigtail single mode fiber," available at https://www.thorlabs.com/newgrouppage9.cfm?objectgroup_id=1489&pn=LP450-SF15#5230 Rev. 2020-11-26.

[106] Thorlabs, "Collimator," available at https://www.thorlabs.com/thorproduct.cfm?partnumber=CFC-8-A Rev. 2020-11-26.

[107] Thorlabs, "Power supply," available at https://www.keysight.com/en/pd-836433-pn-E3631A/80w-triple-output-power-supply-6v-5a-25v-1a?cc=FR&lc=fre Rev. 2020-11-28.

[108] Thorlabs, "Pin pd," available at https://www.thorlabs.com/newgrouppage9.cfm?objectgroup_id=3257&pn=PDA10A2#1896 Rev. 2020-11-26.

[109] M. Chafii A. W. Azim, Y. Le Guennec and L. Ros, "Enhanced Optical-OFDM with index and dual-mode modulation for optical wireless systems," *IEEE Access*, vol. 8, pp. 128646–128664, July 2020.

[110] Y. Le Guennec A. W. Azim, M. Chafii and L. Ros, "Spectral and Energy Efficient Fast-OFDM with Index Modulation for Optical Wireless Systems," *IEEE Communications Letters*, pp. 1–1, Apr 2020.

[111] M. Chafii A. W. Azim, Y. Le Guennec and L. Ros, "LACO-OFDM with index modulation for optical wireless systems," *IEEE Wireless Communications Letters*, pp. 1–1, Dec. 2020.

[112] E. P. Simon and M. A. Khalighi, "Iterative soft-kalman channel estimation for fast time-varying MIMO-OFDM channels," *IEEE Wireless Communications Letters*, vol. 2, no. 6, pp. 599–602, August 2013.